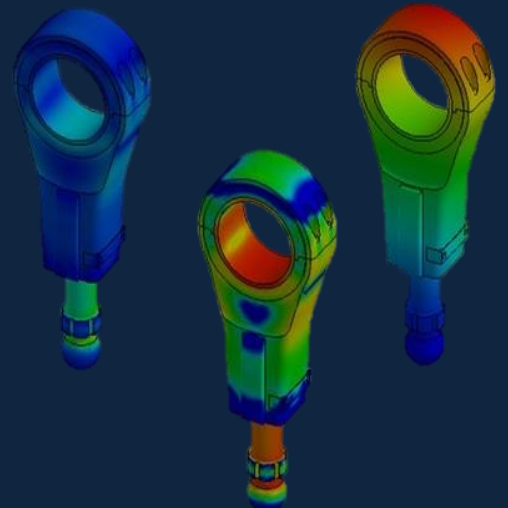$$F=ma$$

$$E=mc^2$$

$$\int \frac{dy}{dx}dt$$

International Advanced Researches and Engineering Journal (IAREJ) is a double-blind peer-reviewed and publicly available online journal that has Editorial Board (https://dergipark.org.tr/en/pub/iarej/board). The editor in chief of IAREJ welcomes the submissions that cover theoretical and/or applied researches on **Engineering** and related science with Engineering. The publication language of the Journal is **English**. **Writing Rules** are given in Author Guidelines (https://dergipark.org.tr/en/pub/iarej/writing-rules). IAREJ publishes **original papers** that are research papers and technical review papers.

IAREJ publication, which is **open access**, is **free of charge**. There is no article submission and processing charges (APCs).

IAREJ is indexed & abstracted in:

Crossref (Doi prefix: 10.35860/iarej.)
Directory of Open Access Scholarly Researches (ROAD)
Directory of Research Journals Indexing (DRJI)
EBSCO
Google Scholar
Index Copernicus (ICI Journal Master List)
J-Gate
TUBITAK ULAKBIM TR Dizin (TR index)
WorldCAT

Authors are responsible from the copyrights of the figures and the contents of the manuscripts, accuracy of the references, quotations and proposed ideas and the Publication Ethics (https://dergipark.org.tr/en/pub/iarej/page/4240).

International Advanced Researches and Engineering Journal (IAREJ) allows the author(s) to hold the copyright of own articles.

©
IAREJ
15 April 2023

Table of Contents

Research Articles

Research Article

Investigation of the effect of boriding on the wear behaviour of AISI 1050 carbon steel

Safiye Ipek Ayvaz [a,*] (iD)

[a]*Manisa Celal Bayar University, Turgutlu Vocational School, Celal Bayar University, 45400 Manisa, Turkey*

ARTICLE INFO	ABSTRACT
	In this study, AISI 1050 carbon steel samples were boronized with the powder pack boriding technique at 875°C for 2, 4 and 6 hours using Ekabor 2 boriding powder. The boride layer thicknesses obtained with the boriding time increased and after 2, 4 and 6 hours of boriding, a 30.6, 40.0 and 71.8 μm boride layer, predominantly composed of Fe_2B phase, was obtained. Boride layers were formed in tooth-like morphology. Thanks to this boride layer, the surface hardness of the substrate was improved 6.2-6.4 times and a maximum surface hardness of 1543.8 HV was reached. With the Daimler-Benz Rockwell-C adhesion tests, it was determined that the adhesion quality of the boride layer was generally at the HF1 level. With the boriding carried out, the specific wear loss of AISI 1050 steel was reduced from 421.25 mm^3/Nm x10^{-6} to 17.67 mm^3/Nm x10^{-6}, and the wear resistance was increased approximately 24 times.

1. Introduction

Boriding is a surface coating process performed with a thermochemical technique. In this process, boron (B) atoms are transferred to the metal substrate by diffusion and it is aimed to increase the surface quality by obtaining high hardness, excellent wear and improved corrosion resistance [1-5]. Among the boriding methods that can be performed in a solid, salt solution, electrolytic, plasma and gas environments. The solid boriding is used more widely than others due to its low cost and ease of application [6-8].

The solid boriding method is carried out by keeping the metal substrate in boron powder at temperatures between 850-1050 °C for 1-10 hours. [9-11]. At the end of this waiting period, the formation of a single- or bi-phase layer (FeB+Fe2B) is observed on the surface by the diffusion of boron atoms onto the metal substrate [12,13]. The FeB phase is more fragile. In addition, the two phases have different expansion coefficients, the formation of the Fe2B phase is more desirable than the formation of the double-layer FeB+Fe2B phase. [7, 14, 15].

Boriding process is also widely used in non-ferrous metals. Liu et al. were borided 99.9% pure tungsten discs at 950-1050 °C for 2-8 hours with the pack boriding process. After boriding, a boride layer consisting of WB+W2B phases with 18-116.2 μm thickness was obtained. As a result, in the applied tests, it was determined that the neutron attenuation capabilities of the samples increased with boriding [16]. Gunen et al. boronized Monel 400 alloy at temperatures of 900-1000 °C Celsius at 2-6 temperatures. A boride layer had 35-290 μm thickness and a hardness of 1002-1476 HV0.025, consisting of the N2B phase, was obtained with the boriding process. The boron activation energy was calculated as 300.7 kjmol-1 [17]. Yıldız boronized Cobalt-Magnesium (CM) and Nickel-Magnesium (NM) alloys at 900 °C for 1.5-4.5 hours with pack boriding technique. NiB in the NM alloy and Co2B in the CM alloy were obtained. While the layer thickness obtained in the CM alloy was 47.9-145.21 μm, 67.21-179.84 μm boride layers were obtained in the NM alloy [18]. Kaner et al. boronized powder metal pure chromium samples for 2, 4, 6 and 8 hours at 1000 °C to obtain a boride layer consisting of CrB, Cr2B, Cr2B3 and Cr3B4 phases [19]. Kanca boronized Invar-36 superalloy with powder-pack boriding technique for 975 °C for 5 and 7 h, and a boride film consisting of FeB, NiB and Fe2NiB phases had 176.9-189.1 μm thickness was obtained. The tribological investigations carried out showed that the boride film decreased the wear loss of Invar-36 superalloy 28.6-105 times [20].

In borided iron-based materials, high hardness, improved tribological properties and chemical stability are

obtained on the surface due to the boride films formed on the substrate surface [21-25]. Because of these results, boriding is applied in many areas (implants, agricultural machinery, tools, etc.) [2, 3, 26, 27]. Many studies have been conducted in the literature on the effect of boriding on wear. Boriding is also a highly effective thermochemical process in increasing the wear resistance of various steel alloys. In particular, it provides high wear resistance to steel under low loads due to its brittle structure [22]. Arslan et al. borided AISI 8620 steel by electrolysis method. They found the wear loss of the unborided and borided samples to be 0.265 ± 0.01 mm3 and 0.003 ± 0.001 mm3, respectively [14]. Türkmen et al. borided SAE 1020 steel with the powder boriding method. As a result of the tribological studies carried out, they determined that the abrasion resistance increased approximately 47 times [7]. Ulutan et al. applied the powder boriding process to AISI 4140 steel and identified that the wear resistance increased nearly 3-4 times compared to the unborided sample [8]. Taktak reported that when he borided 52100 and 440C steel alloys with powder boriding, their abrasion resistance improved 3 and 2.5 times, respectively [24]. Sezgin and Hayat obtained a boride film of 26.13-109.04 μm, consisting of FeB, Fe2B and MnB phases, with the powder pack boriding technique for 2, 4, and 6 h at 850-950 °C for novel high manhanese steels. With the corrosion tests carried out, it has been reported that the borided samples have a higher corrosion resistance than the unborided samples [28].

As can be understood from the outcomes of previous studies, boriding increases the mechanical properties of the surface and improves corrosion and wear resistance in both non-ferrous metal alloys and various steel alloys. However, some alloying elements such as Cr, Ni and Si have a negative effect on the formation and morphological properties of the boride film. Some of them cause the thickness of the layer to be formed as a result of boriding process to decrease, while others cause a flat layer by disrupting the tooth-like morphology of the boride film. For this reason, boriding process is a thermo-diffusional coating process that is more widely applied in plain carbon steels. In this study, AISI 1050 steels, which are used in a wide range of parts in many different machinery manufacturing, are boronized. The microstructural properties, hardness profile and adhesion strength of the borided boride film were investigated and its effect on the wear behaviour of AISI 1050 steel was presented.

2. Materials and Methods

In this study, AISI 1050 steel alloy samples with a diameter of 20 mm and a height of 10 mm were used as substrate material. The samples were borided using Ekabor 2 boriding powder in 50 mm diameter and 50 mm high AISI 304L stainless steel alloy boriding boxes. The boriding process was carried out at 875 °C for 2, 4 and 6 hours. After boriding, the cross-sections of the surfaces of the samples were obtained. The cross-sectional surfaces of the borided samples were sanded with 100-1200 grit sandpapers. The sanded sample surfaces were polished using 3 and 1 μm diamond suspensions, respectively. The polished surfaces were etched using 3% Nital solution. The thickness of the boride films was measured with the Nicon Eclipse LV150N optical microscope (OM) and Clemex image analysis software. In addition, the microstructures of the boride films were examined with the scanning electron microscope (SEM) (FEI QUANTA 250 FEG) in the backscattered electron (BSE) mode was performed.

Microhardness changes of boride films from surface to substrate were performed using Future-Tech FM-700 (Future-Tech Corp, JAPAN) Vickers microhardness tester for 100 gf and 10 s. Tribological examinations were carried out with a Anton Paar CSM Tribometer model wear tester (Switzerland) in accordance with ASTM G99-17 (2017) standards. The tests were carried out with 6 mm diameter 100Cr6 balls under 10N load with a sliding distance of 1000m and a sliding speed of 0.2 m·s-1. The wear type of the boride film was identified by performing SEM examinations of the worn surfaces.

3. Results and Discussion

In Figure 1, SEM micrographs are given from the cross-sectional surfaces of boride films obtained in AISI 1050 steel borided with box boriding technique for 2, 4 and 6 hours at 875 °C boriding temperature. As it is well known, since boron atoms diffuse faster in the [001] direction of the lattice structure, boride grains grow faster in the [001] direction than in other directions, perpendicular to the surface. For this reason, boride films are formed in a sawtooth-like morphological structure. Thanks to this sawtooth morphological structure, improved adhesion strength between the boride film and the substrate is obtained [27, 29]. As seen in Figure 1, this sawtooth morphological boride film was formed in AISI 1050 steel as well. In addition, it was observed that the formed boride film was generally Fe$_2$B compound. Another phenomenon observed from SEM micrographs was the porous structure of the boride film surface of AISI 1050 steel. Kirkendall explained that in thermo-diffusional methods, the porous structure occurs when the diffusion rate differs locally. This phenomenon is termed the "Kirkendall effect" [9, 30].

In Figure 2, the thicknesses of the boride films formed in AISI 1050 steel as a result of different boriding times are presented. The thickness of the boride films obtained as a result of boriding for 2, 4 and 6 hours at 875 °C boriding temperature were measured as approximately 30.6, 40.0 and 71.8 μm, respectively. Atik et al. reported that when they borided AISI 1010 steel at 900 °C for 8 hours, they obtained a 140 μm thick boride film [31]. For the same boriding

parameters as temperature and boriding time, the boride film thickness was measured as 130 μm in AISI 1040 steel. Petrova and Suwattananont, on the other hand, obtained a 76 μm thick boride film consisting of FeB and Fe2B boride compounds in AISI 1018 steel in consequence of boriding at 850 °C for 4 hours [32]. Boztepe and Bayramoğlu reported that after boriding at 900 °C for 6 hours, a 79 μm thick boride film consisting of FeB and Fe2B phases was obtained on the surface of AISI 1050 steel [33].

In Figure 3, the microhardness change of the boride film formed in AISI 1050 steel borided for 2, 4 and 6 hours at 875 °C boriding temperature, depending on the depth, is presented graphically. In microhardness measurements, the microhardness of the substrate material was determined as 230-240 $HV_{0.1}$. After 2, 4 and 6 hours of boriding, the maximum microhardness values of the surfaces were measured as 1431.9, 1499.7 and 1543.8 $HV_{0.1}$, respectively. Therefore, the microhardness values of the surface of AISI 1050 steel have been improved by approximately 6.2-6.4 times. As seen in Figure 1, the boride films formed generally consisted of Fe_2B phase. The measured hardness values are in agreement with similar studies in the literature in which the Fe_2B phase is formed. Milinovic et al. reported that when they borided AISI 1015 steel at 970 °C for 8 hours, they obtained a boride film consisting of Fe_2B phase with a hardness of 1541 HV [34]. Türkmen and Yalamaç measured the microhardness of the boride film consisting of Fe_2B phase in AISI steel in the range of 1329.19 ± 54.96 - 1541.85 ± 168.21 $HV_{0.1}$ after 4 hours of boriding at 850 °C [9].
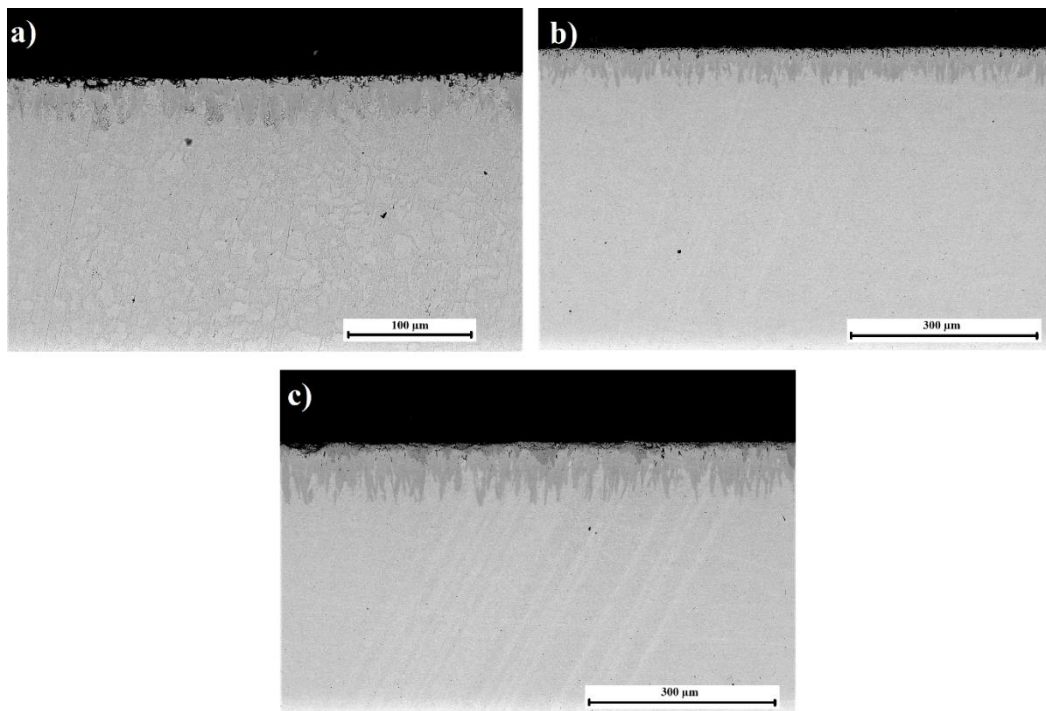
Figure 1. Cross-sectional SEM micrographs of the borided samples: a) 2 h, b) 4 h and c) 6 h
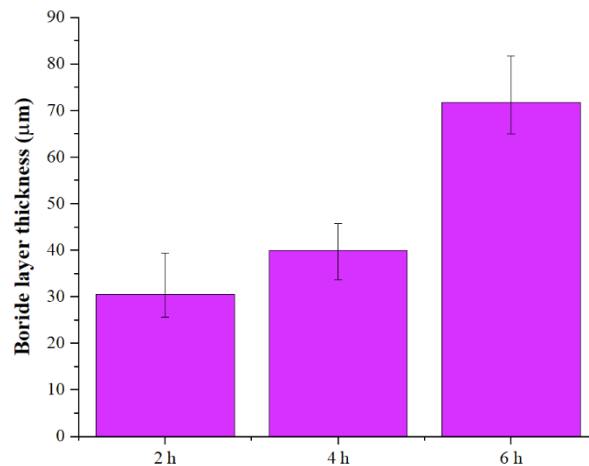
Figure 2. Boride layer thickness for various boriding time
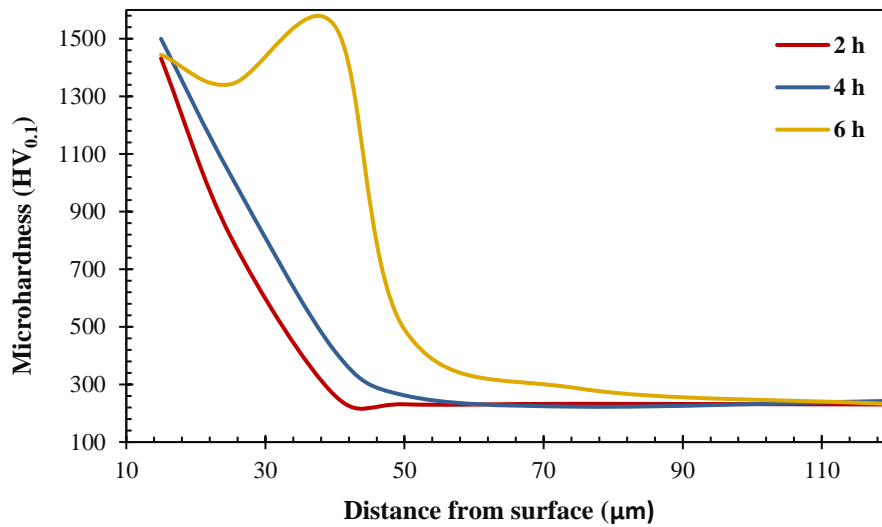
Figure 3. Microhardness variation depending on layer thickness for different boriding times

In Figure 4a-c, SEM images of the craters formed as a outcomes of Daimler-Benz Rockwell-C adhesion tests can be seen on the surfaces of the samples that were borided at 875 °C for 2, 4 and 6 hours, respectively. No delamination failure was observed when the craters were examined. In addition, radial cracks around the craters were clearly seen in the SEM images. While this type of crack was observed in all borided samples, an increase in the number and thickness of cracks was detected with the increase in boriding time. The cohesion quality of the boride films was found acceptable according to the HF1 grade according to the adhesion strength quality maps [35]. Success in adhesion strength is a result of its single-phase structure. It has been reported that the single-phase layer (Fe_2B) has good adhesion properties [9].
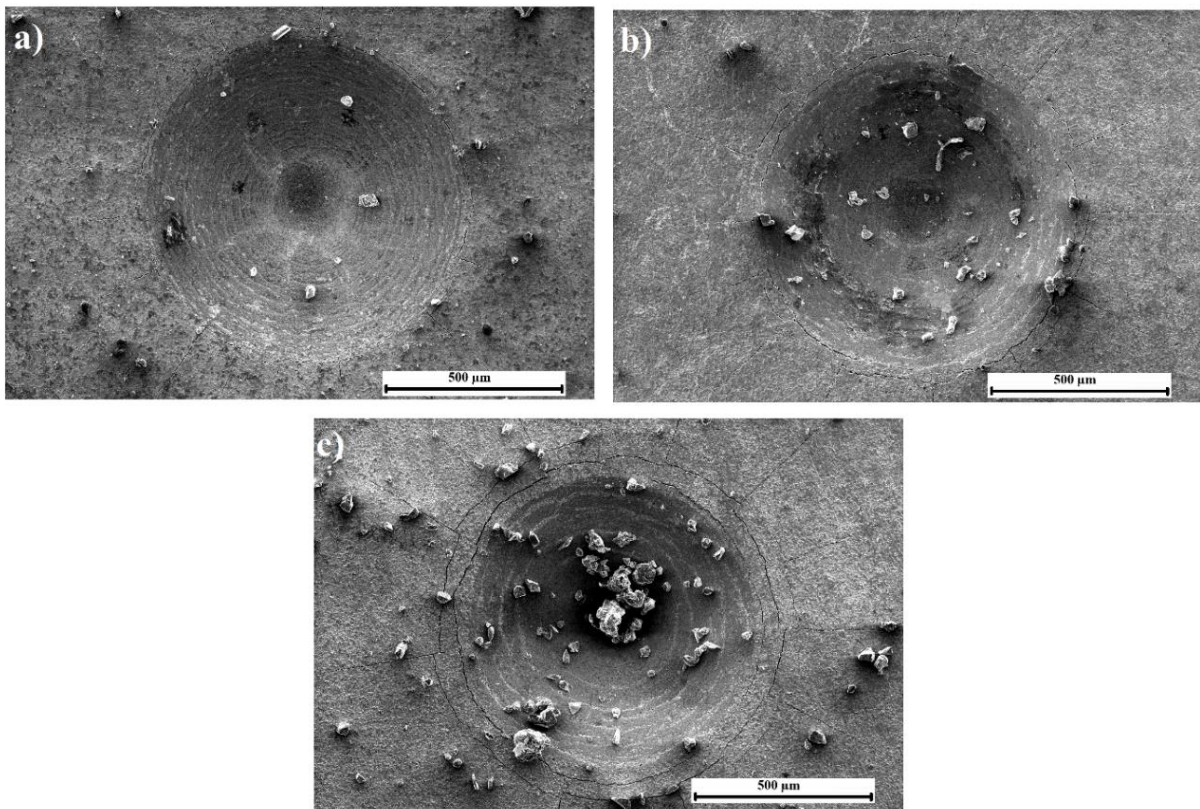
Figure 4. SEM images of craters formed after the Daimler-Benz Rockwell-C adhesion test: a) 2 h, b) 4 h and c) 6 h

The specific wear rates obtained as a result of the wear tests are given in Fig. 5. The specific volumetric wear rate of unborided AISI 1050 carbon steel was determined as 421.25 mm^3/Nm x10^{-6}. The specific wear rates of the borided samples at 875 °C for 2, 4 and 6 hours using Ekabor 2 boriding powder with the pack boriding method were determined as 31.47, 17.67, 22.47 mm^3/Nm x10^{-6}, respectively. Therefore, the wear resistance of AISI 1050 steel has been increased ~13-24 times by boriding. Küçükkurt borided AISI M35 and AISI M42 high speed-tool steels at 850, 900 and 950 °C for 2, 4 and 6 hours using Ekabor II powder in his master's thesis. After the wear tests, the lowest specific volumetric wear rate in AISI M35 steel was reported as 1.540 mm^3/Nm x10^{-5}. In AISI M42 steel, the lowest specific wear rate was measured as 1.820 mm^3/Nm x10^{-5} [36]. Güneş and Yıldız borided AISI 310 stainless steel alloy with Ekabor II powder in their study. 10 N load and 1000 m road parameters were used in the wear tests. In consequence of the wear tests, the lowest specific volumetric wear rate was determined as mm^3/Nm x10^{-5} in the borided sample at 1050 °C for 6 hours [37]. García-Leon et al. determined the specific volumetric wear rate of borided AISI 316L steel as 14.1 mm^3/Nm x10^{-6} [38]. Soydan et al. thespecific wear rates of AISI 4140, AISI 8620 and AISI 1050 steels, which they boron for 6 hours at 950 °C using Ekabor 1 powder, were determined as 16, 18 and 20 mm^3/Nm x10^{-6}, respectively, against carburized AISI 1020 steel [39]. As can be seen, the results obtained are in agreement with the literature. In Figure 6, SEM images of the worn layers of the unborided, 2, 4 and 6 hours borided samples are given. In the unborided sample, it is clear from the deep grooves on the worn surface that the wear type is predominantly abrasive wear (Fig. 6a). After 2 hours of boriding, it was observed that the abrasive wear of the sample was greatly reduced (Fig. 6b). Wear failure in the form of pitting was noticed on the worn layer of this sample. It was observed that a flat worn layer was formed in the 4 hours borided sample (Fig. 6c), in which the lowest specific wear rate was determined. In addition, some wear debris was observed in this sample. Similarly, this wear debris was observed in the borided sample for 6 hours (Fig. 6d). However, when the worn layer was examined, delamination areas and some abrasive grooves were detected. With the occurrence of these wear types, the specific volumetric wear rate increased in this sample.
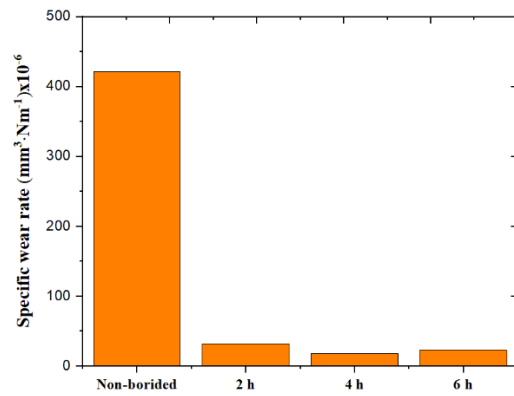

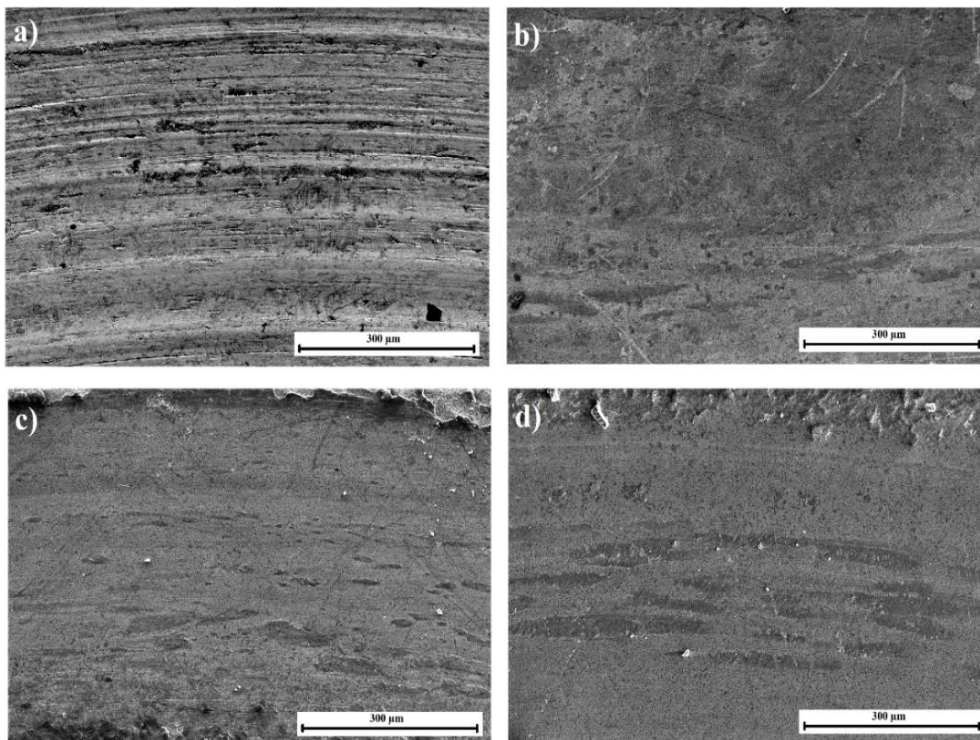Figure 5. The specific wear rate of the samples

Figure 6. SEM images of the worn surfaces of non-borided (a), 2 h (b), 4 h (c), and 6 h(d) borided AISI1050 steels

4. Conclusion

In this study, the microstructural and tribological properties of the samples borided at 875 °C for 2, 4 and 6 hours using Ekabor 2 boriding powder on AISI 1050 carbon steel and the cohesion quality of the boride films were investigated. The summary of the obtained data is as follows:

- As a result of boriding, a boride film consisting of Fe_2B phase was obtained.

- After 2, 4 and 6 hours of boriding, approximately 30.6, 40.0 and 71.8 μm boride films were obtained, respectively.

- Microhardness values of the surface of AISI 1050 steel were improved by approximately 6.2-6.4 times with boriding.

- The abrasion resistance of AISI 1050 steel increased ~13-24 times with boriding.

Declaration

The author declared no potential conflicts of interest with respect to the research, authorship, and/or publication of this article. The author also declared that this article is original, was prepared in accordance with international publication and research ethics, and ethical committee permission or any special permission is not required.

Author Contributions

S. İPEK AYVAZ developed the methodology, performed the experiments and wrote the manuscript. T. Author proofread the manuscript.

References

1. Hernandez-Ramirez, E.J., A. Guevara-Morales, U. Figueroa-Lopez and I. Campos-Silva, *Wear resistance of diffusion annealed borided AISI 1018 steel*, Materials Letters, 2020. **277**: 128297.

2. Genel, K., *Boriding kinetics of H13 steel*, Vacuum, 2006. **80**: p. 451-457.

3. Er, U. and B. Par, *Wear of plowshare components in SAE 950C steel surface hardened by powder boriding,* Wear, 2006. **261**: p. 251-255.

4. Çavdar, U. and E. Atik, Properties *of boronized, carbonitrided and steamed ıron-based compact*, Materials Testing, 2014. **56**(2): p. 126-130.

5. Altintaş, A., Y. Sarigün and U. Çavdar *Effect of Ekabor 2 powder on the mechanical properties of pure iron powder metal compacts.* Revista de Metalurgia, 2016. **52**(3): e073.

6. Akshay, A.J. and S.S. Hosmani, *Pack-boriding of AISI 4140 steel: boriding mechanism and the role of container design,* Materials and Manufacturing Processes, 2014. **29**: p. 1062-1072.

7. Turkmen, I., E. Yalamac and M. Keddam, *Investigation of tribological behaviour and diffusion model of Fe₂B layer formed by pack-boriding on SAE 1020 steel,* Surface and Coatings Technology, 2019. **377**: 124888.

8. Ulutan, M., M.M. Yildirim, O.N. Celik and S. Buytoz, *Tribological properties of borided AISI 4140 steel with the powder pack-boriding method,* Tribology Letters, 2010. **38**: p. 231-239.

9. Turkmen, I. and E. Yalamac, *Effect of alternative boriding mixtures on boride layer and tribological behaviour of borided SAE 1020 steel,* Metals and Materials International, 2022. **28**: p. 1114-1128.

10. Arslan, D. and S. Akgün, *Mechanical characterization of pack-boronized AISI 4140 and AISI H13 steels*, International Advanced Researches and Engineering Journal, 2021. **5**(1): p. 61-71

11. Kartal, G., O.L. Eryilmaz, G. Krumdick, A. Erdemir and S. Timur, *Kinetics of electrochemical boriding of low carbon steel,* Applied Surface Science, 2011. **257**: p. 6928-6934.

12. Genel, K., I. Ozbek and C. Bindal, *Kinetics of boriding of AISI W1 steel,* Materials and Science Engineering, 2003. **A347**: p. 311-314.

13. Sen, S., I. Ozbek, U. Sen and C. Bindal, *Mechanical behaviour of borides formed on borided cold work tool steel,* Surface and Coatings Technology, 2001. **135**: p. 173-177.

14. Arslan, M., A.C. Ok, G.K. Sireli and S. Timur, *Investigation on stuructural and tribological properties of borided gear steel after phase homogenization,* Surface and Coatings Technology, 2022. **429**: 127967.

15. Martini, C., G. Palombarini, G. Poli and D. Prandstraller, *Sliding and abrasive wear behaviour of boride coatings,* Wear, 2004. **256**: p. 608-613.

16. Liu, Y., X. Liu, C. Lai, J. Ma, X. Meng, L. Zhang, G. Xu, Y. Lu, H. Li, J. Wang and S. Chen, *Boriding of tungsten by the powder-pack process: Phase formation, growth kinetics and enhanced neutron shielding*, International Journal of Refratory Metals and Hard Materials, 2023, **110**: 10649.

17. Günen, A., M. Keddam, A. Erdoğan and M.S. Karakaş, *Pack-Boriding of Monel 400: Microstructural Characterization and Boriding Kinetics*, Metals and Materials International, 2022, **28**: 1851-1863.

18. Yildiz, I., *Surface Characterization and Boriding of Nickel and Cobalt Alloys*, Protection of Metals and Physical Chemistry of Surfaces, 2022, **58**: 772–778.

19. Kaner, S., Y. Kaplan, Ö., Pamuk and S. Aksöz, *Production and Tribological Investigation of Cr Borides by Boriding of Powder Metallurgy Pure Chromium Surface*, Journal of Materials Engineering and Performance, (2022). https://doi.org/10.1007/s11665-022-07195-4

20. Kanca, Y., *Microstructural characterization and dry sliding wear behavior of boride layers grown on Invar-36 superalloy*, Surface and Coating Technology, 2022, **449**: 128973.

21. Garcia-Leon, R.A., J. Martinez-Trinidad, I. Campos-Silva, U. Figueroa-Lopez and A. Guevara-Morales, *Development of tribological maps on borided AISI 316L stainless steel under ball-on-flat wet sliding conditions,* Tribology International, 2021. **163**: 107161.

22. Selcuk, B., R. Ipek and M.B. Karamis, *A study on friction and wear behaviour of carburized, carbonitrided and borided AISI 1020 and 5115 steels,* Journal of Materials Processing Technology, 2003. **141**: p. 189-196.

23. Ueda, N., T. Mizukoshi, K. Demizu, T. Sone, A. Ikenaga and M. Kawamoto, *Borıdıng of nickel by the powder-pack method,* Surface and Coatings Technology, 2000. **126**: p. 25-30.

24. Taktak, S., *Tribological behaviour of borided bearing steels at elevated temperatures,* Surface and Coatings Technology, 2006. **201**: p. 2230-2239.

25. Ipek Ayvaz, S. and I. Aydin, *Tribological and adhesion properties of microwave-assisted borided AISI 316L steel,* Materials Testing, 2022. **64**: p. 249-259.

26. Ipek Ayvaz, S. and I. Aydin, *Effect of the microwave heating on diffusion kinetics and mechanical properties of borides in AISI 316l,* Transactions of the Indian Instute of Metals, 2020. **73**: p. 2635-2644.

27. Carrera-Espinoza, R., , U. Figueroa-Lopez, J. Martinez-Trinidad, I. Campos-Silva, E. Hernandez-Sanchez and A. Motallebzadeh, *Tribological behavior of borided AISI 1018 steel under linear reciprocating sliding conditions,* Wear, 2016. **362-363**: p. 1-7.

28. Sezgin, C.T. and F. Hayat, *The effects of boriding process on tribological properties and corrosive behavior of a novel high manganese steel,* Journal of Materials Processing Tech., 2022, **300**: 117421

29. Medvedovski, E., *Formation of corrosion-resistant thermal diffusion boride coatings,* Advanced Engineering Materials, 2016. **18**: p. 11-33.

30. Krelling, A.P., F. Teixeira, C.E. da Costa, E.A.S. Almeida, B. Zappelino and J.C.G. Milan, *Microabrasive wear behavior of borided steel abraded by SiO_2 particles,* Journal of Materials Research and Technology, 2019. **8**: p. 766-776.

31. Atik, E., U. Yunker and C. Meric, *The effects of conventional heat treatment and boriding on abrasive wear and corrosion of SAE 1010, SAE 1040, D2 and 304 steels,* Tribology International, 2003. **36**: p. 155-161.

32. Petrova, R. and N. Suwattananont, *Surface modification of ferrous alloys with boron,* Journal of Electronic Materials, 2005. **34**: p. 575-582.

33. Boztepe, M.H. and M. Bayramoglu, *Optimization of process parameter of boronized AISI 1050 steel using the taguchi analysis,* The 17th International Conference on Machine Design and Production, 2016. Bursa: p. 1-11.

34. Milinovic, A., S. Brod, D. Krumes, I. Kladaric, S. Klaric and S. Aracic, *An investigation of boride layers growth kinetics on C15 steel,* 16th International Research/Expert Conference "Trends in the Development of Machinery and Associated Technology, 2012. Dubai: p. 135-138.

35. Vidakis, N., A. Antoniadis and N. Bilalis, *The VDI 3198 indentation test evaluation of a reliable qualitative control for layered compounds,* Journal of Materials Processing Technology, 2003. **481**: p. 143–144.

36. Küçükkurt, M., *Borlanmış AISI M35 ve AISI M42 Çeliklerinin Karakterizasyobu ve Aşınma Davranışlarının İncelenmesi,* 2015. Afyon Kocatepe Üniversitesi: Turkey. p. 112.

37. Gunes, İ. and I. Yıldız, *Investigation of Adhesion and Tribological Behavior of Borided AISI 310 Stainless Steel,* Revistamateria, 2016. **21**: p. 61-71.

38. Garcia-Leon, R.A., J. Martinez-Trinidad, R. Zepeda-Bautista, I. Campos-Silva, A. Guevara-Morales, J. Martinez-Londono and J. Barbosa-Saldana, *Dry sliding wear test on borided AISI 316L stainless steel under ball-on-falt configuration: a statistical analysis,* Tribology International, 2021. **157**: 106885.

39. Soydan, Y., S. Köksal, A. Demirer and V. Çelik, *Sliding Friction and Wear Behavior of Pack-Boronized AISI 1050, 4140, and 8620 Steels,* Tribology Transactions, 2008. **51**: p. 74-81.

Research Article

Optimizing the wind power generation cost in the Tirumala Region of India

Prasun Bhattacharjee [a],* , Somenath Bhattacharya [a]

[a]Jadavpur University, Raja Subodh Chandra Mallick Rd, Kolkata 700032, India

ARTICLE INFO	ABSTRACT

Global warming is impacting almost every nation of the world and causing excessive socioeconomic damage to human civilization. India is presently the second most inhabited country on the planet and possesses the noteworthy potential to curb global greenhouse gas emissions. Most of the stakeholders of the global communities have signed the Paris treaty of 2015 to curtail the surface temperature rise. As the central government of India has announced its target to attain net zero-emission by the end of 2070, the electricity generation sector of the country needs to utilize renewable resources like wind energy rapidly. This paper focuses to optimize the wind energy generation cost in the Tirumala region of the country using the Genetic Algorithm and Particle Swarm intelligence concurrently. Tirumala is located in the area of Tirupati in the southern state of Andhra Pradesh. A relative analysis of the optimization outcomes validates the superiority of the Genetic Algorithm over the Binary Particle Swarm Optimization Algorithm for minimizing the wind energy generation cost. The application of the Genetic Algorithm has been proven to cut down the generation cost by up to 7.56% as compared to the usage of Binary Particle Swarm Optimization for similar terrain conditions and wind flow conditions in the Tirumala Area.

1. Introduction

Climate change is impacting human communities across the continents of the world and devastating economies extensively [1]. Because of the universal concern for the restricted reserve of non-renewable fuels and their life-threatening after-effects on the ecosystem, renewable energy resources expound rich substitutes for global scientific society [2]. International renewable energy utilization has advanced rapidly in the current century [3]. Worldwide collective Wind Power Generation (WPG) competence has increased by more than 32 times in the past 20 years [4]. Worldwide wind energy utilization per capita augmented by 230 times in the past 30 years. Currently, India generates around 10% of its combined electricity generation capability from WPG systems [5]. The expenditure of WPG has been economical for the previous few decades and is anticipated to shrink by 7% in 2022 [6].

Hasager et al. [7] dealt with the probability of Indian offshore WPG with ENVISAT information. Nagababu et al. [8] scrutinized the Indian offshore WPG capacity with the OSCAT evidence. Singh and Kumar S.M. [9] evaluated the Indian offshore WPG competence and strived for minimizing the generation expenditure. the WPG capacity in the Tirumala district of India has been explored with Artificial Intelligence (AI) methods [10]. In another study, the reevaluation and bathymetry information have been employed for gauging the WPG fitness in the special commercial parts in India, formulating lenience for the prevalent salt-water biotic conditions [11]. Investigators have calculated a larger offshore WPG proposal in the western seashore of Gujarat state of India with the biological examination, and generation expense has been projected [12]. The lightning search algorithm was involved in multi-objective WPG farm layout improvement with more than a few airflow settings for upgraded efficiency regarding energy generation and venture expenditures [13]. The wind farm design proposal has been improved for a Spanish WPG farm with the coral reefs' optimization procedure counting the substrate level [14]. Gradient-centered optimization method has been directed for WPG farm layout enhancement, and the scrutiny conclusions have been juxtaposed with the same accomplished through large-eddy simulation [15].

This research aims for recognizing the optimum charge of WPG for the Tirumala zone in India. Due to the

computing might of AI systems have been employed in quite a lot of engineering disciplines [16][17]. That is why the Genetic Algorithm (GA) and Binary Particle Swarm Optimization Algorithm (BPSOA) were applied concurrently to optimize the WPG cost in the Tirumala area to assess the relative efficiency of the two AI methods for optimizing the generation cost and improving the design of WPG farm accordingly due to their ability to deal with the binary values ('1' for presence and '0' for the absence of turbine in a layout). Moreover, this study can aid concerned researchers and businesses to measure the effect of AI in the planning of WPG systems.

2. Problem Formulation

WPG systems are expected to remain economically worthwhile by competently controlling the generation cost (G_c). The generation cost has been evaluated using Eqs. (1)-(4) suggested in the 22nd Genetic and Evolutionary Computation Conference [18].

$$G_c = \frac{\{A\}+(B)}{(1-(1+r)^{-y})/r} * \frac{1}{8760*P} + \frac{0.1}{N} \tag{1}$$

$$A = C\left(\frac{2}{3} + \frac{1}{3}e^{-0.00174N^2}\right) \tag{2}$$

$$B = C_{om}N \tag{3}$$

$$C = \left\{C_t N + C_s floor\left(\frac{N}{m}\right)\right\} \tag{4}$$

where C_t represents the expenditure of a Wind Turbine (WT). C_s signifies the expenditure for a sub-station. N designates the sum of WTs in a WPG farm and m is WT per sub-station. C_{om} designates the yearly operative and upkeep charge. P symbolizes the energy harvest of the whole WPG farm. r denotes the fraction of interest. y shows the lifetime of the WPG farm. The directional wind-flow pattern in the Tirumala region has been shown in Fig. 1.

The contemplated terrain settings for this research are displayed in Figs. 2 and 3. Layout 1 is of 2000 m x 2000 m dimension and lacks any obstruction. Layout 2 is 2000 m x 2000 m with an internal obstruction of 1000 m x 1000 m. The internal obstruction has been marked in red and the available area for turbine placement has been shown in green in Figs. 2 and 3.

AI algorithms have been utilized in the current work to optimize the generation cost in the Tirumala area of India. The algorithms considered randomly generated locations (with horizontal and vertical distances) of WT inside the limitations of the considered terrain setting. Subsequently, the generation cost of wind power has been computed by applying Eqs. (1)-(4). The minimal WPG cost has been found after iterating the above-mentioned optimization process up to the maximum generation number and the optimal locations of WT for each considered terrain condition in the present study.
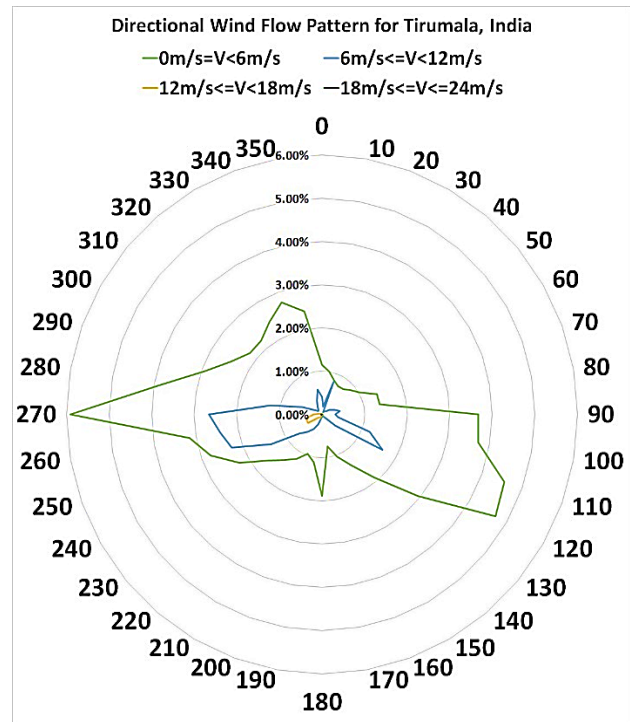

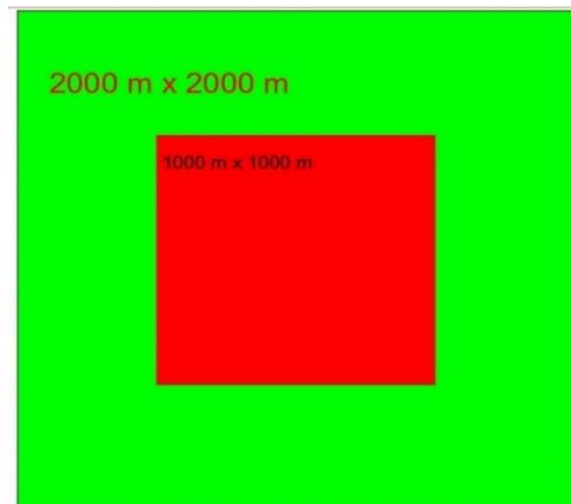Figure 1. Wind-Flow Form in Tirumala, India

Figure 2. Layout 1

Figure 3. Layout 2

3. Optimization Algorithm

3.1 Genetic Algorithm (GA)

GA can be termed as a bio-enthused metaheuristic scheme to suggest resolutions for optimization trials representing the evolvement of natural preference as projected by Turing [19][20]. The algorithm has been described as follows [16].

1. Organize the parameters such as population span, replication tally, potentials for crossover, and mutation.
2. Administer the suitability of every chromosome.
3. Engage the population unsystematically.
4. Scrutinize the suitability of every chromosome.
5. Launch the arithmetic crossover procedure.
6. Initiate the mutation action.
7. Measure the properness of the renewed beings.
8. Classify the most remarkable consequence by tracking the choice maker's penchant.

3.2 Binary Particle Swarm Optimization Algorithm (BPSOA)

The BPSOA is an altered preparation of particle swarm optimization algorithm that considers all constituents as strings of bits [21]. The BPSOA can be described as follows.

1. Comprehensively construct a basic population.
2. Arbitrarily form the essential velocities inside the restrictions.
3. Allot the opening values for local and global finest sites.
4. Calculate the weights obligatory for velocity development.
5. Adjust the velocities of the particles consequently.
6. Swap the positions of the particles.
7. Settle if the ultimate conditions are grasped, else revert to stage 3.

4. Results and Discussion

AI algorithms like Genetic Algorithm and Binary Particle Swarm Optimization have been employed for optimizing the WPG cost in the Tirumala area in India. Two dissimilar terrain settings have been considered and the AI algorithms utilized numerous randomly created positioning of WTs in each terrain setting for computing the WPG cost up to the extreme generation count. After ranking the calculated WPG costs, the most optimal value of generation charge has been found for both terrain conditions. Later, the optimal values of WPG costs computed using GA and BPSOA have been compared to select the most efficient AI algorithm for the considered optimization scenario.

The values of vital factors associated with WT and optimization processes have been displayed in Table 1. They have been deemed as per Wilson et al. (2018). The WPG cost has been calculated using Eqs. (1)-(4). The optimum locations of WTs for both layouts utilizing both optimization processes have been shown in Figs. 4-7. The vertical and horizontal axes symbolize the length and breadth of the proposed terrains for WPG systems. The red dot indicates the placement of a WT within the layout.

Table 1. Values of Vital Factors

| Factor	Value
Populace Range	20
Utmost Generation number	50
Turbine Output	1.5 MW
Blade Diameter	77 m
Inter-Turbine Space	308 m
Lowest Allowable Wind Velocity	12 km/hr.
Supreme Allowable Wind Velocity	72 km/hr.
Capital Charge per WT	$ 750,000
Sub-Station Cost per Sub-Station	$ 8,000,000
Total WTs per Sub-Station	30
Proportion of Interest	3%
Annual Maneuver and Upkeep Expenditure	$ 20,000
Possible Working Time	20 Years
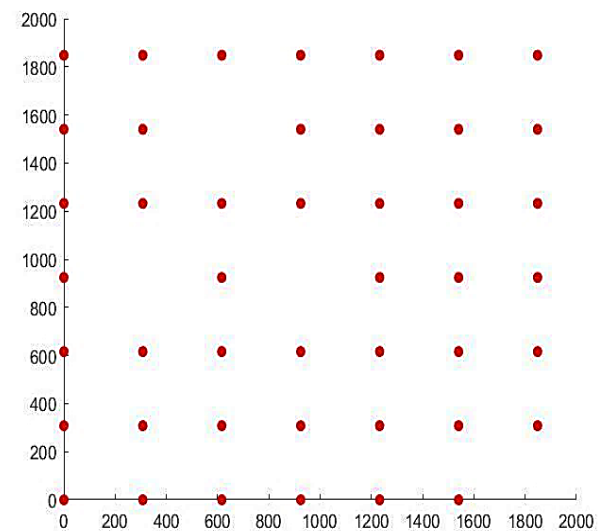
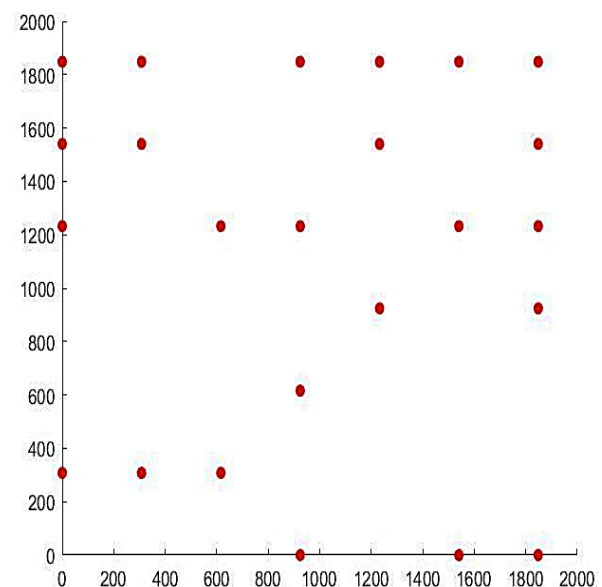Figure 4. Optimal Placement of WTs for Layout 1 Using GA

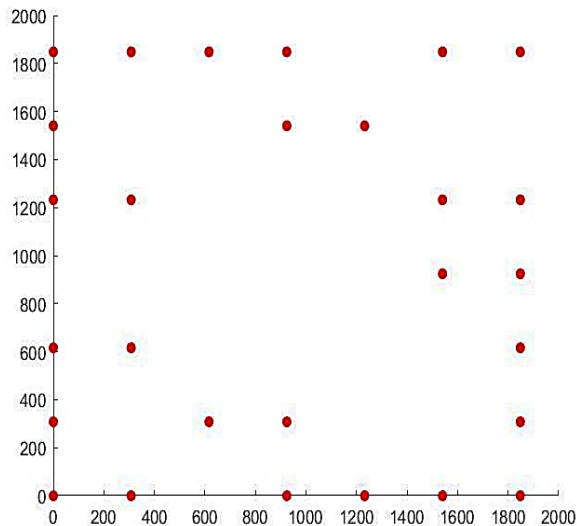Figure 5. Optimal Placement of WTs for Layout 1 Using BPSOA
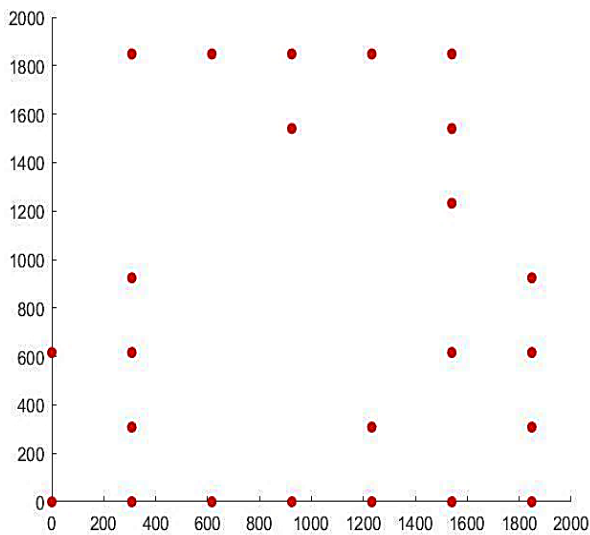
Figure 6. Optimal Placement of WTs for Layout 2 Using GA

Figure 7. Optimal Placement of WTs for Layout 2 Using BPSOA

Table 2. Assessment of Optimized WPG Cost Achieved by GA and BPSOA

Layout	GA Optimized Generation Cost (in USD/kWh)	BPSOA Optimized Generation Cost (in USD/kWh)
Layout 1	0.0110	0.0111
Layout 2	0.0110	0.0119

The generation costs of the WPG in the Tirumala area calculated employing GA and BPSOA have been offered in Table 2. The results show that the optimal generation costs attained for both the layouts by GA are more financially viable than the same achieved by BPSOA. The WPG costs achieved by GA are 0.90 % and 7.56% more optimal than the same attained by BPSOA. The optimization consequences authenticate the pre-eminence of GA over BPSOA for optimizing the WPG cost in the Tirumala area in India. The improved generation cost can assist the WPG businesses to stay economical and feasible for practical implementation.

5. Conclusions

The Paris agreement of 2015 guides the associated countries to control the emancipation of greenhouse gases for lessening the penalties caused by global climate change. The resourceful management of renewable energy generation expertise can abet countries realize their carbon neutrality ambitions. Wind power can play a crucial role in limiting the carbon footprint of electricity businesses.

This present research aims for minimizing the WPG cost in the Tirumala area of India. GA and BPSOA have been exercised to optimize the layouts for better financial feasibility. The outcomes validate the supremacy of GA over BPSOA for minimizing the WPG cost. This work can prompt innovative prospects for WPG layout optimization. In the forthcoming works, WTs with advanced generation capability and wheel area can be tried. As the current study has been conducted considering the cost function provided by Wilson et al. (2018), the results need to be verified using other similar functions in future studies.

Declaration

The authors declare no potential conflicts of interest with respect to the research, authorship, and/or publication of this article. The authors also declare that this article is original and was prepared in accordance with international publication and research ethics, and ethical committee permission or any special permission is not required.

Author Contributions

Prasun Bhattacharjee developed the methodology and wrote the article. Somenath Bhattacharya scrutinized the research work.

Acknowledgment

References

1. Obama, B., *The irreversible momentum of clean energy.* Science, 2017. **355**(6321): pp. 126-129.

2. Chaurasiya, P. K., Warudka, V., and S. Ahmed, *Wind energy development and policy in India: A review.* Energy Strategy Reviews, 2019. **24**: pp. 342-357.

3. BP, *BP Statistical Review of World Energy.* 2022. [Online]. Available: https://www.bp.com/en/global/corporate/energy-economics/statistical-review-of-world-energy.html. [Accessed 19 April 2022].

4. Global Wind Energy Council, *Global Wind Energy Outlook.* 2014. [Online]. Available: http://www.gwec.net/wp-content/uploads/2014/10/GWEO2014_WEB.pdf. [Accessed 06 September 2020].

5. Ministry of Power of Government of India, *Renewable Generation Report.* 2021. [Online]. Available: https://cea.nic.in/renewable-generation-report/?lang=en. [Accessed 23 July 2021].

6. Global Wind Energy Council, *India Wind Outlook Towards 2022: Looking beyond headwinds.* 2020. [Online]. Available: https://gwec.net/india-wind-outlook-towards-2022-looking-beyond-headwinds/. [Accessed 23 July 2021].

7. Hasager, C. B., Bingöl, F., Badger, M., Karagali, I. and E. Sreevalsan, *Offshore Wind Potential in South India from Synthetic Aperture Radar.* Information Service Department Risø National Laboratory for Sustainable Energy Technical University of Denmark, 2011.

8. Nagababu, G., Simha R, R., Naidu, N. K., Kachhwaha, S. S., and V. Savsani, *Application of OSCAT satellite data for offshore wind power.* In 5th International Conference on Advances in Energy Research, 2015, Mumbai, India.

9. Singh, R., and A. Kumar S.M., *Estimation of Off Shore Wind Power Potential and Cost Optimization of Wind Farm in Indian Coastal Region by Using GAMS,* In International Conference on Current Trends Towards Converging Technologies (ICCTCT), 2018.

10. Kumar, M. B. H., Balasubramaniyan, S., Padmanaban, S., and J. B. Holm-Nielsen, *Wind energy potential assessment by weibull parameter estimation using multiverse optimization method: A case study of Tirumala region in India.* Energies, 2019. **12**(11): pp. 2158.

11. Nagababu, G., Kachhwaha, S.S., Naidu, N. K., and V. Savsani, *Application of reanalysis data to estimate offshore wind potential in EEZ of India based on marine* ecosystem *considerations.* Energy, 2017. **118:** pp. 622–631.

12. Kumar, R., Stallard, T., and P. K. Stansby, *Large-scale offshore wind energy installation in northwest India: Assessment of wind resource using Weather Research and Forecasting and levelized cost of energy.* Wind Energy, 2020. **24**(2): pp. 174–192.

13. Moreno, S. R., Pierezan, J., Coelho, L. dos S., and V. C. Mariani, *Multi-objective lightning search algorithm applied to wind farm layout optimization.* Energy, 2021. **216:** p. 119214.

14. Pérez-Aracil, J., Casillas-Pérez, D., Jiménez-Fernández, S., Prieto-Godino, L., and S. Salcedo-Sanz, *A versatile multi-method ensemble for wind farm layout optimization.* Journal of Wind Engineering and Industrial Aerodynamics, 2022. **225**: p. 104991.

15. Thomas, J. J., Bay, C. J., Stanley, A. P., and A. Ning, *Gradient-Based Wind Farm Layout Optimization Results Compared with Large-Eddy Simulations.* Wind Energy Science Discussions, 2022. pp. 1-28.

16. Jana, R. K., and P. Bhattacharjee, *A multi-objective genetic algorithm for design optimisation of simple and double harmonic motion cams.* International Journal of Design Engineering, 2017. **7**(2): pp. 77-91.

17. Turkoglu, B., and E. Kaya, *Training multi-layer perceptron with artificial algae algorithm.* Engineering Science and Technology, an International Journal, 2020. **23**(6): pp. 1342-1350.

18. Wilson, D., Rodrigues, S., Segura, C., Loshchilov, I., Hutter, F., Buenfil, G. L., Kheiri, A., Keedwell, E., Ocampo-Pineda, M., Özcan, E., Peña, S. I. V., Goldman, B., Rionda, S. B., Hernández-Aguirre, A., Veeramachaneni, K., and S. Cussat-Blanc, *Evolutionary computation for wind farm layout optimization.* Renewable Energy, 2018. **126**: pp. 681-691.

19. Turing, A., *Computing Machinery and Intelligence (1950).* In The Essential Turing, Oxford University Press, 2004.

20. Akarsu, C. H., and Küçükdeniz, T., *Job shop scheduling with genetic algorithm-based hyperheuristic approach.* International Advanced Researches and Engineering Journal, 2022. **6**(1): pp. 16-25.

21. Bhattacharjee, P., Jana, R. K., and S. Bhattacharya, S. (2021). *A Relative Analysis of Genetic Algorithm and Binary Particle Swarm Optimization for Finding the Optimal Cost of Wind Power Generation in Tirumala Area of India.* In ITM Web of Conferences, 2021. **40**: p. 03016.

.

Research Article

Numerical investigation of aerodynamic performance and noise characteristic of air multiplier bladeless fan

Firdevs Yedekcioglu [a] [ID]*, Sumeyye Akyildiz [b]* [ID] *and Zekeriya Parlak [c,]* [ID]

[a]Sakarya University, Institute of Natural Sciences, Sakarya 54187,Turkiye
[b]Gazi University, Graduate School of Natural and Applied Science, 06560, Teknikokullar, Ankara, Turkiye
[c]Sakarya University, Department of Mechanical Engineering, Sakarya 54187,Turkiye

ARTICLE INFO	ABSTRACT
	Air multiplier fans, which are produced as an alternative to the convectional propellers used today, have come into prominence with the advantages providing in both efficiency and usage. In this study, three different blade profiles based on NACA 0012, NACA 1408, and EPPLER 1214 were used in the fan body. The design based on the NACA 0012 of body profile provided the highest flow rate. This profile was optimized using CFD analysis according to seven different geometrical parameters determined as the angle of attack, width, length, gap, inner and outer diameters, and tail length. The profile that provides less noise against the highest flow rate was determined as the optimal design. With CFD analysis, the sound pressure level of the optimal design was calculated by the k-ω and LES method, and the results were compared with each other.

1. Introduction

Today, while designing the fan, new and special designs are made by trying to improve the features of the fan. Despite the fact that fans are typically divided into axial or radial, the bladeless mechanism is distinct from both, this novel fan was developed by the English company Dyson in 2009 as an alternative to conventional fans. This fan design has become remarkable due to the simple shape of the model, the absence of a visible rotating fan, stable air supply, portability, easy cleaning, and reliability for children and pets. The device called as bladeless fan or air multiplier consists of two parts the cylindrical lower part and the circular air frame [1]. As shown in Figure 1, the air is sucked in by the fan in the body, accelerated, and forced to pass through the circular narrowing gap under high pressure at the back of the frame. According to Bernoulli's equation, the air accelerates while the passing through the narrowing slit and pressure drops [2].

Initially, it dwelled on the practical applications, social and economic implications of the air multiplier rather than its theoretical research. Li et al. [3] examined the effect the Coanda surface in the different curvatures on the performance of the air multiplier. They designed and simulated 5 types of Coanda surfaces with different curvatures and compared the results with the prototype.

Lasse and Simon [4] analyzed the flow characteristics of the Dyson air multiplier, performed CFD analysis for two different turbulence models, k-ε and k-ω, and determined that the k-ε turbulence model produced more accurate results for the air multiplier fan. Li et al. [5] investigated the outlet flow field of the air multiplier numerically and experimentally, analyzed it according to the k-ε model and confirmed the results with CTA, and concluded that the RNG k-ε model is a reliable model for estimating the time-dependent flow cycle in the fan outlet area.

Jafari et al. [6] investigated the potential of using a bladeless fan of 60 cm diameter inside a cubic room for industrial applications with numerical analysis and also examined its performance with experimental tests. According to the results of this study, the bladeless air multiplier can be designed in large sizes and used in a variety of industries such as underground tunnels or to remove smoke and dust from industrial environments.

Zafer and Gürsoy [7] in this study is concerned with the computational aero-acoustic analysis of an airfoil with jet blowing. The airfoil shape is chosen as NACA0015 profile with jet blowing on upper surface. The calculations of analysis are done by using commercial finite volume solver. The k-ε turbulence model is used for the turbulence modeling and the Ffowcs Williams and Hawking acoustic

analogy model is run for determination of acoustic data. The numerical results are compared with experimental data for computed Sound Pressure Level without jet blowing and well agreement is observed. The effects of different jet angles, velocity ratios, and angles of attack on airfoil are investigated in the case of jet blowing, and noise levels of non-jet and jet blowing cases are studied.

Kocak at al. [8] in this investigation flow performance of the rod-airfoil configurations is taken into consideration in order to understand the flow physics and acoustic performance of turbomachines, such as fans, wind and water turbines. Shear layer and Von-Karman vortex structures break apart at the leading edge of the airfoil and small vortices are generated through the airfoil. Due to the flow-solid surface interaction, noise and vibration arise. Rod-airfoil configurations can perfectly model turbomachines because the main cause of broadband noise in turbomachines is also incoming turbulent and stator interaction. The airfoil is placed in the wake region of the cylinder and the obtained results are compared with the experimental results from the literature. It was shown that, the developed numerical method and Computational Aeroacoustics Analysis (CAA) methodology compare well with the measurements obtained in an accompanying experiment. After validating, the results obtained with the developed numerical methodology, the cylinder diameter effects on vortex zones, separation point, reattachment point and sound pressure level is investigated. It was observed that with the increase in the Strouhal number, the Sound Pressure Level (SPL) levels of the configuration rises.

İlter [9] computed the flow around NACA 0012 foil using numerical techniques, and the effects of edge angle of attack and trailing edge shape on flow noise were investigated in two dimensions. In order to validate this study, the flow noise around a circular cylinder has also been investigated. The pressure fluctuations around the body were obtained by numerically solving Navier Stokes equations, and the equations were discretized using the Finite Volume Method (FVM), which is widely used in fluid dynamics The quadrupole component of sound was investigated by using Curle and Proudman methods which were derived from Lighthill analogy and far field noise was computed by using Ffowcs Williams and Hawkings (FW-H) equations.
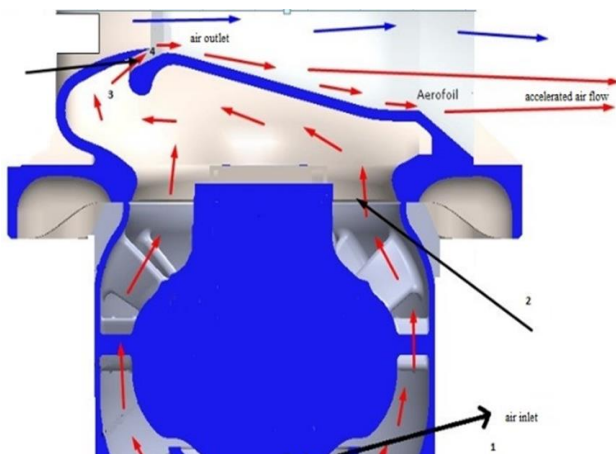

Figure 1. Working Principle of Fan

The sound pressure levels of an axial fan are numerically investigated in this paper using the Ffowcs-Williams & Hawkings (FW-H) analogy and the computational fluid dynamics (CFD) method. A simulation model based on unstructured mesh structure and Standard k-epsilon (k-ε) turbulence model is established for high speed rotation (3000 RPM), and the numerical simulation results are compared with experimental data specified by blade manufacturer company. Noise generation mechanism in the axial fan shroud are discussed using with the numerical results. [10]

Li [11] created and studied a bladeless fan prototype using numerical simulations in the current study. The entire fan prototype, including wind channel, base, rotor, and stator, is used to characterize the aerodynamic and aeroacoustic performances of the bladeless fan; when investigating the influence of the wind channel's geometric parameters, only the wind channel is considered in simulations. The effects of slit width, cross-section height, slit location, and cross-section profile are investigated.

Mehmood et al. [12] computationally analyzed a circular type bladeless ceiling fan in a standard empty room (4m x 4m x 4m). Different design features such as fan radius, height from the ceiling and floor, fan jet width, mass flow rate, and orientations were studied metrically, and their effect on perceived comfort level in terms of velocity spread and average velocities was computed. The results show that the fan height in the close vicinity of ceiling does not affect the flow field in the occupied zones, however, as the fan gets closer to the floor the velocity field in the occupied zone changes due to creation of a strong vortex at the center of floor. Thus, fan installation closer to the ceiling (less than 0.5m from the ceiling) is a preferred choice. With an increase in fan radius from 0.3m to 0.5m, an increment of 33% was observed in velocity spread thus increasing the zone of influence.

Ravi and Rajagopal. [13] conducted a three-dimensional numerical study to investigate the effect of various geometric shapes and slit angles on bladeless fan performance for various aerodynamic profiles. Airfoils considered for the present study are E169, E473 and E479 which are then reformed into a typical bladeless fan arrangement. The three-dimensional fluid flow variations through and across the airfoil were simulated by solving the governing equations, namely the continuity and Reynolds Averaged Navier-Stokes equations (RANS). The three-dimensional fluid flow variations through and across the airfoil have been simulated by solving the appropriate governing equations namely continuity and Reynolds Averaged Navier-Stokes equations (RANS). Numerically predicted results of lift, drag and streamwise velocity decay along the jet centerline of a cylindrical channel are compared with literature and a very close agreement exists between the two. Upon validation, geometric shapes - circular and square cross section with aspect ratios of 1, 1.5 and 2 and slit angles of 20, 40, 60 and 80 degrsee for all the above three airfoil configurations are analyzed numerically for various inlet Reynolds number. From the study it is observed that Eppler 473 airfoil profile

with slit thickness of 1 mm and slit angle of 80° provided the maximum discharge ratio of 34.17 for an inlet mass flow rate of 80 LPS.

Jafari et al [14] investigated effect of five geometric parameters on well aeroacoustic sound performance of a Bladeless fan. Li et al [15] investigated the outlet flow field of an annular jet for a bladeless fan experimentally using constant temperature anemometer hot-wire system at five Reynolds numbers. Joshi et al [16] investigated the influence of the airfoil's outlet slit thickness on the discharge ratio by varying the outlet slit thickness of an Eppler 473 airfoil from 1.2 mm to 2 mm in intervals of 0.2 mm. Results indicated that smaller slits showed higher discharge ratios.

In this study, three different bladeless fan geometries were created based on NACA 0012, NACA 1408 and EPPLER 1214 airfoils. As a result of CFD analysis, NACA 0012 was chosen because it gave the highest flow rate. The optimization study was made in the ANSYS Response Surface Optimization module according to seven different geometrical design parameters for the NACA 0012 profile to obtain the least noise against the best flow rate. The optimal geometry of the circular airfoil profile was determined as a result of the optimization by CFD analyses. Also, the sound pressure levels of the bladeless fan were calculated with both k-ω and the LES method and the results were compared with each other.

2. Design and CFD Analysis

Figure 2 shows the airflow in the propeller geometry of air multiplier manufactured by Dyson. Air, which is forced pass through the circular narrow gap at high velocity and low pressure, causes that air behind into the device also sucks towards the circular frame with the Coanda effect, thus total flow rate becomes a lot of times increased, it is defined as the multiplied flow rate. The ratio of the flow rate coming out of the airfoil circular body and the flow rate suctioned the inlet pipe by the rotating fan can be defined as follows.

$$Q_{inlet} = V_{inlet} \times A_{inlet} \qquad (1)$$

However, Dyson company stated that this ratio is about 15.
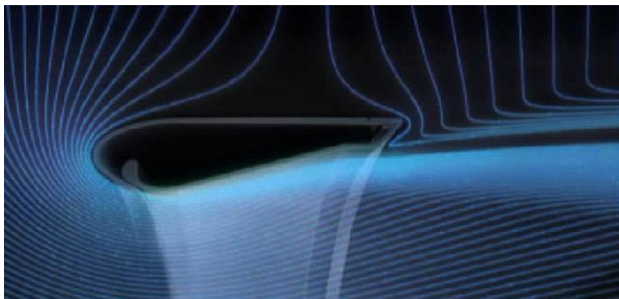

Figure 2. The effect of the Coanda effect on the air multiplier propeller [2]

Lasse and Simon [4] analyzed the device with a bladeless profile section without a bottom cylinder. Thermophysical properties of the air are accepted as density (ρ) is 1.225 kg/m³, dynamic viscosity (μ) is 1.7894.10-5 kg/ms airflow velocity (V) is 2.5 m/s. They stated that the fan generates less noise due to low turbulence generation, there is some high turbulence near the jet nozzle, the output current is relatively constant.

Three different geometries were created for the same parameters based on three different airfoils, which are NACA0012, NACA1408 and EPPLER1214. Among these profiles, NACA0012 was chosen because it is generally used in the literature, NACA1408 was chosen because it is similar to the NACA 0012 profile as symmetrical characteristic. EPPLER1214 model was chosen as an alternative model. The determined airfoils are given in Figure 3.

The model shown in Figure 4 was drawn in the ANSYS DesignModeller tool. The system consists of two units. The lower unit is the section where the air enters and the second unit is the section through which the air is directed and sent from a circular narrow gap. The view of the airfoil on the geometry is shown in Figure 4. The mesh is shown in Figure 5. The skewness value of the mesh is greater than 0.7, however the number of elements with these skewness values is extremely low. The same is valid for orthogonal quality values less than 0.2. Because it has a very complex geometry and extremely small gaps through which the fluid passes, the best available mesh has been developed after mesh independence tests.

For the turbulence model, a solution was tried by both k-ε and k-ω and the analyzes were continued with k-ω since better convergence. In order to capture the boundary layer correctly, the mesh density in the boundary layer was determined for the y+ value, which was obtained about as 1 and maximum 1.8 for all three profiles.

(a)

(b)

(c)
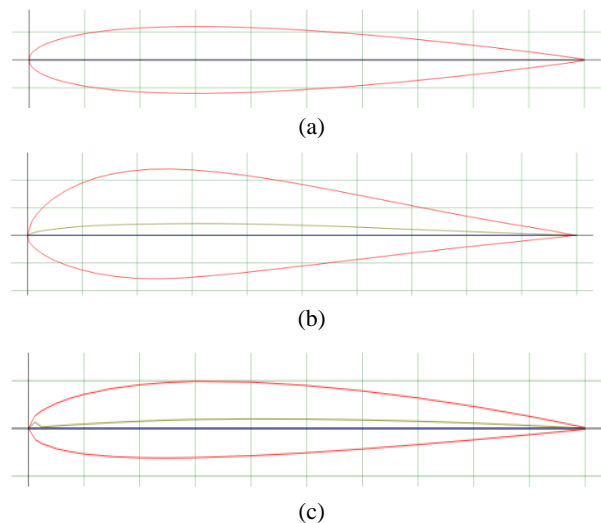
Figure 3. Chosen airfoiller (a) NACA0012, (b) NACA1408 and (c) EPPLER1214
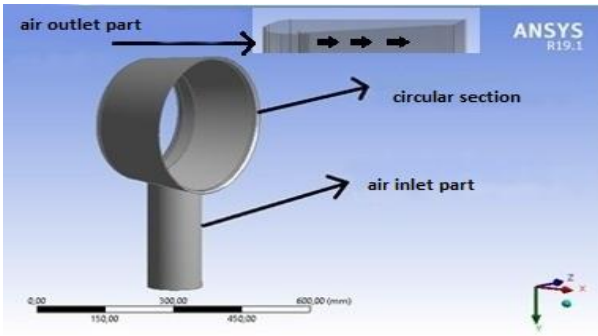
Figure 4. Geometry model based on NACA 0012 airfoil.
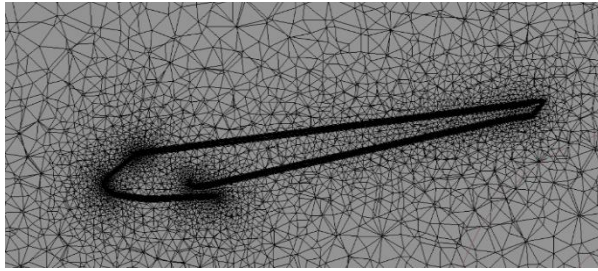
Figure 5. Mesh (NACA 0012)

3. Results of Aerodynamic Analysis

Boundary conditions for aerodynamic analysis of bladeless fan are shown in Table 1. The design parameters are shown in Table 2. and Figure 6.

Table 1. Boundary Conditions

Velocity inlet	Outlet pressure	Turbulence model
0.02 m³/s	0 Pa	k-ω

Table 2. Initial values of design parameters

Parameter	Initial Values
Width [mm]	9
The angle of Attack [°]	7
Gap [mm]	5
Diameter [mm]	116
Tail Length [mm]	10
Tail Angle [°]	45
Length [mm]	200

When the velocity vectors in Figure 7 and the velocity contours in Figure 8 are examined for the three airfoil geometries, it is seen that the circular airfoil geometry designed based on the NACA0012 profile accelerates the airflow more than the others. While the maximum velocity is approximately 18 m/s in the NACA 0012 profile, it is calculated as 12.5 m/s in the NACA1408 profile and 12 m/s in the EPPLER1214 profile. In addition, the flow is more stable and homogeneous in the NACA0012 profile. Due to the airfoil structure, the flow is more turbulent in the NACA1408 profile.
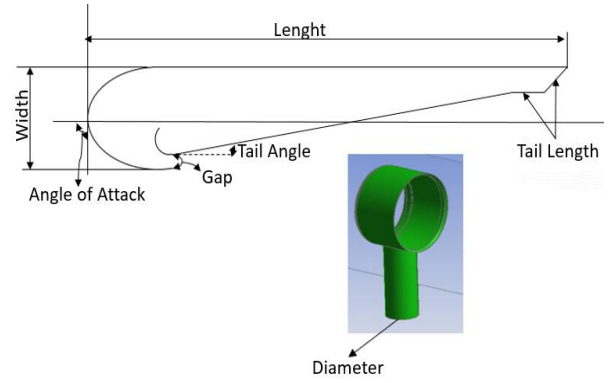
Figure 6. Design parameters determined for analysis in NACA 0012 airfoil geometry
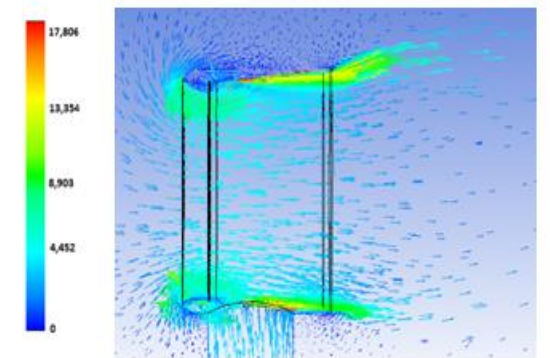
(a)
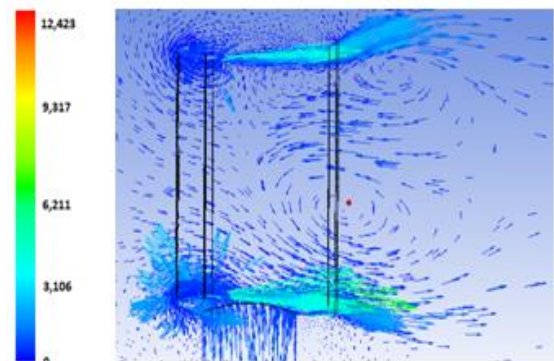
(b)
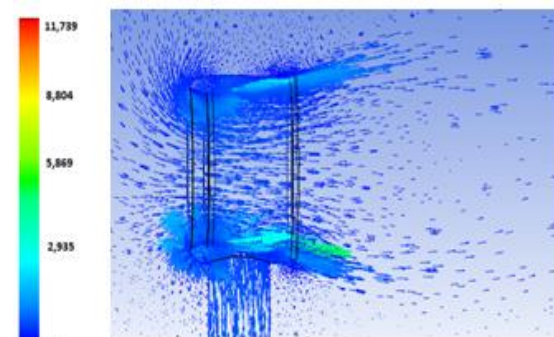
(c)

Figure 7. a) Velocity vectors of a) NACA0012, b) NACA1408, c) EPPLER 1214 profiles

(a)

(b)

(c)
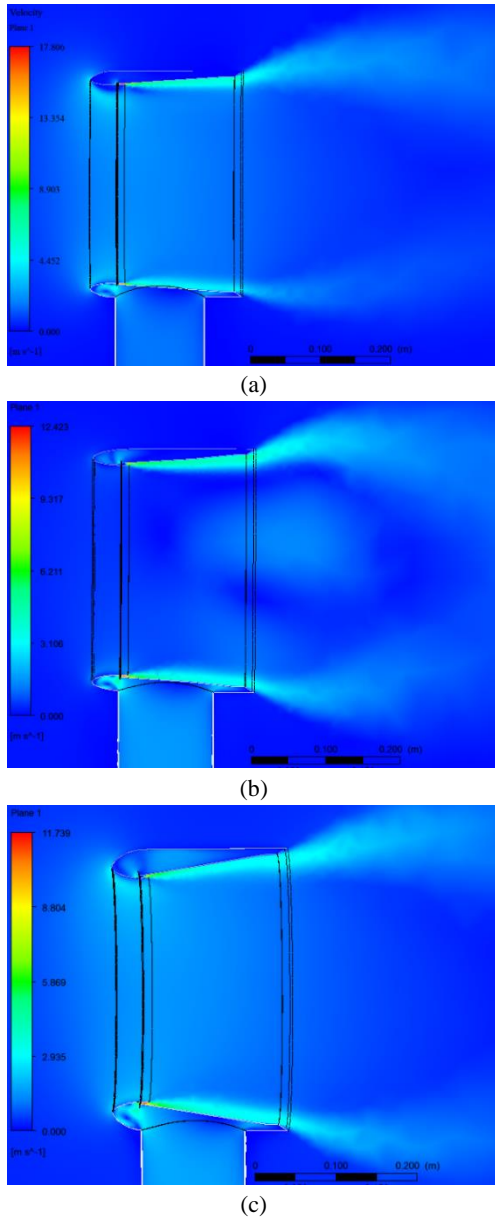
Figure 8. a) NACA 0012, b) NACA 1408, c) EPPLER 1214 velocity contours for shell design

The ratios of the flow rate at outlet to the flow rate at inlet are shown in Figure 9 for the profiles. Due to it was determined that the NACA0012, NACA1408 and EPPLER1214 profiles multiplied the flow rate by 11 times, 6 times, and 5 times, respectively. Regarding to the results, since the geometry created based on the NACA0012 profile increases the flow rate and velocity more than the others, and provides a more stable and homogeneous air flow, acoustic analyzes were continued with NACA0012 profile in the study.

4. Optimization

The optimization study was carried out to obtain the geometric design that provides the desired target values (highest flow, highest speed, least noise) by determining the lower and upper values for the geometric parameters given in Table 2.
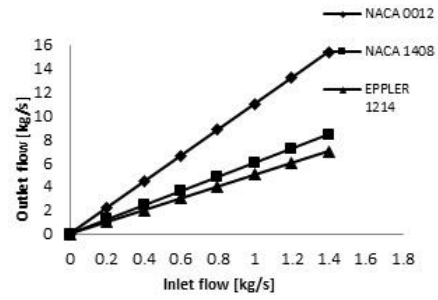
Figure 9. Rates of NACA0012, NACA 1408 and EPPLER 1214 airfoil based geometries of outlet flow to inlet flow

CFD analyzes were performed with geometries between the lower and upper ranges of the design parameters as based on the NACA0012 airfoil profile by using k-ω turbulence model in ANSYS Fluent. As a result of the analysis, it was also calculated how the design parameters in the range changed the target values.

A volumetric flow rate of 0.02 m³/s is required at the fan inlet, and it is expected that the approximate air flow rate at the outlet will increase by 15 times (Table 3.). Air inlet velocity is calculated as 1.89 m/s for the multiplier air inlet area.

Because the diameter of the air inlet is one of the design parameter values, the change in diameter causes the velocity of the inlet air to change. For this reason, the input velocity was defined as a parameter. Outlet pressure is 0 Pa, turbulence model is k-ω.

Table 4. shows the lower and upper limit values of the design parameters. The lower and upper values were determined by taking care not to cause any distortion in the geometry when the value of any parameter is changed.

Response surface methodology (RSM) is a collection of mathematical and statistical techniques, which was applied to establish a mathematical model between independent variable and dependent variable, and find the effect of parameters affecting a response in a process [17]. Originally, RSM was developed to model experimental responses and then migrated to the modelling of numerical experiments.

Table 3. Expected value as a result of calculation

Air inlet volume flow	Air outlet volume flow
0.02 m³/s	0.3 m³/s

Table 4. Parameter values

Parameters	Lower values	Upper Values
Width [mm]	8	12
Angle of attack [°]	0	20
Gap [mm]	2	10
Diameter [mm]	110	130
Tail length [mm]	7	15
Tail angle [°]	30	60
Length [mm]	180	220
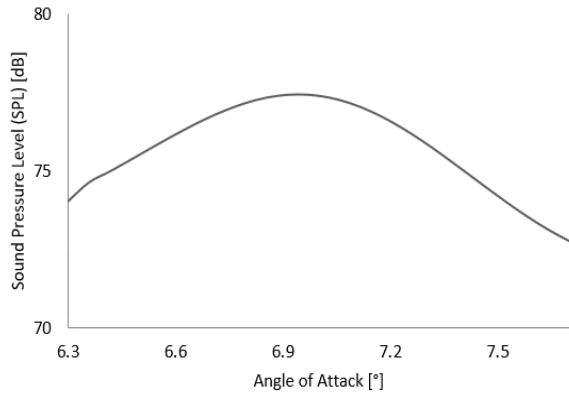
(a)
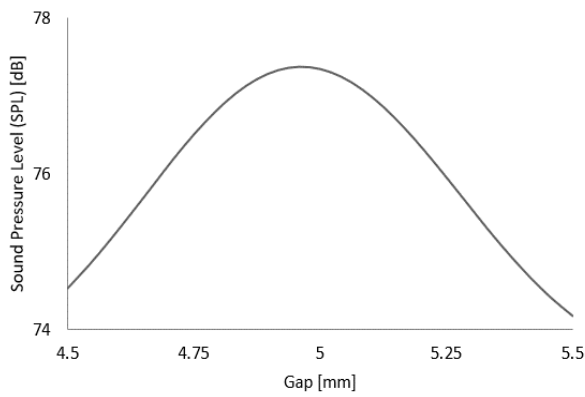
(b)
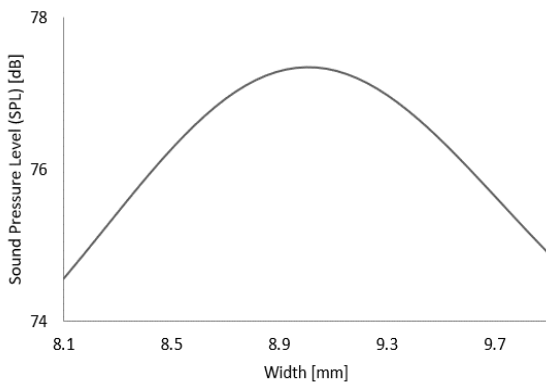
(c)
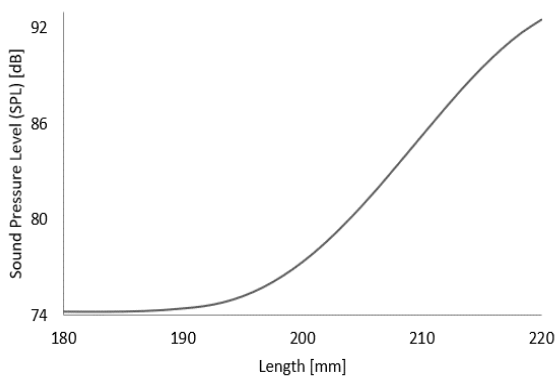
(d)

The Response Surface Optimization method allows us to determine how the parameters change the target values in the specified ranges and to perform the optimization by determining the design parameter values that provide the desired target value. The Response Surface Optimization module was connected to the Fluent analysis and the targets was selected the minimum noise-and maximum flow rate.

The changes in sound pressure caused by the change of each parameter are given in Figure 10. Other parameters were kept constant at the values indicated in Table 2 while examining the changes. As can be seen in Figure 10.a, the sound pressure level increased parabolically from 6.3° to 6.94° of angle attack and reached the maximum sound pressure level of 77 dB, then the sound level decreased parabolically with from 7° to 7.7° of angle attack. As can be seen in Figure 10.b, The sound pressure increased linearly until the gap value was 4,8 mm, and at 5 mm it reached the highest sound pressure level of 77 dB. Although the gap value increased, the sound pressure level decreased linearly. The sound pressure level increased linearly up to the value of the width parameter was 8,8 mm, reaching the highest sound pressure level of 77 dB at 9 mm of. While the width value increased, the sound pressure level decreased linearly (Figure 10.c). As can be seen Figure 10.d, while the value of the length parameter was 195 mm and above, the sound pressure level increased linearly. It reached the highest sound pressure level of 92 dB at 220 mm.
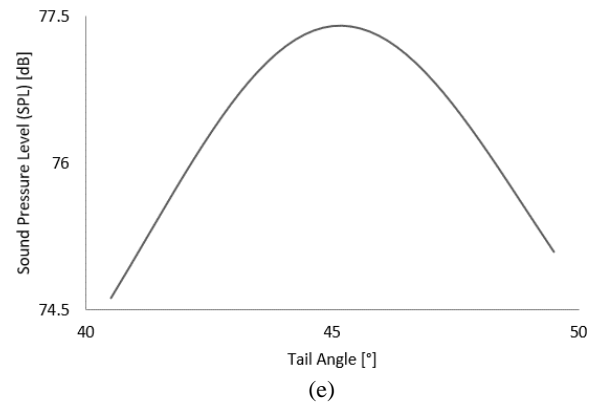
(e)
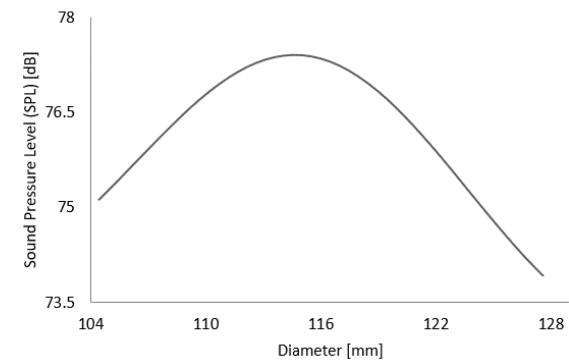
(f)

Figure 10. Effect of design parameters of NACA 0012 on sound level (a) Angle of attack (b) gap (c) width (d) length (e) tail angle (f) diameter

As can be seen Figure 10.e, the sound pressure level increased linearly up to the value of the tail angle parameter was 44°, and the highest sound pressure level reached 77 dB at 45°. In the following values, although the value of the tail angle increased, the sound pressure level decreased linearly. As can be seen Figure 10.f, the sound pressure level increased linearly up to the value of the diameter parameter was 103 mm, and reached the highest sound pressure level of 77 dB at 115.03 mm. While the diameter increased, the sound pressure level decreased linearly.

Optimization results made with Multi Objective Genetic Algorithm (MOGA) method on ANSYS with the help of response surface data created with RSM are given in Table 5. Three different optimal design points, P1, P2 and P3, which provide the highest the ratio of the output flow rate to the flow rate suctioned into the body by the radial fan (multiplied flow rate) and lowest sound pressure level targets, and the values of the design parameters at these points are given in the Table 5.

4.1 Calculation of Sound Pressure Level with k-ω Turbulence Model

A mesh structure has been created for the geometry that produces the least noise and corresponds to the highest ratio of flow rates. The k-ω method yields more accurate results in boundary layer calculations. Moreover, in calculations of acoustic pressure variation, the k-ω method is more suitable for calculating tonal noise. Time dependent flow field analyzes were performed using k-ω turbulence model and Ffowcs William-Hawkings (FW-H) acoustic analogy approach with ANSYS Fluent.

Reference microphones are placed on the geometry in order to examine the sound pressure distribution results. The locations of the microphone points are given in Figure 11. Figure 12 shows the values obtained from the microphones at the reference points at different frequencies.

Table 6. shows the sound pressure level at the microphone points. The 6th and 7th points are in the gap region where the fluid in the body comes out. Since the air velocity is high and the pressure is low here, the air at stagnant atmospheric pressure behind the body moves towards this low pressure region. Therefore, eddies are formed in this region and noise increases for high frequency values. A decrease of approximately 30 dB was observed in the noise level of the microphones at the 4th point, where located just at the exit of the body, and the 5th point, where located more distance of outlet of body. The lowest noise level was calculated as 90 dB at the 5th point.The noise value measured at the 2nd point 50 mm behind the body in the air flow direction is lower than the value at the 1st point, which is the starting point of the body. The noise level at the microphones at point 8 and point 9, which are inside the body but further upstream of the output gap, have a lower value than those at points 6 and 7.

Table 5. Optimization results

Parameters	P1	P2	P3
Width [mm]	9.8193	9.8678	9.8968
The angle of Attack [°]	7.6962	7.6769	7.6848
Gap [mm]	5.4976	5.4898	5.4975
Diameter [mm]	115.21	115.93	112.73
Tail length [mm]	9.3284	9.3161	9.5405
Tail angle [°]	42.801	42.984	42.396
Length [mm]	201.74	199.12	199.14
Ratio of flow rates	4.437	4.4831	4.5213
Sound pressure level [dB]	84	84	84
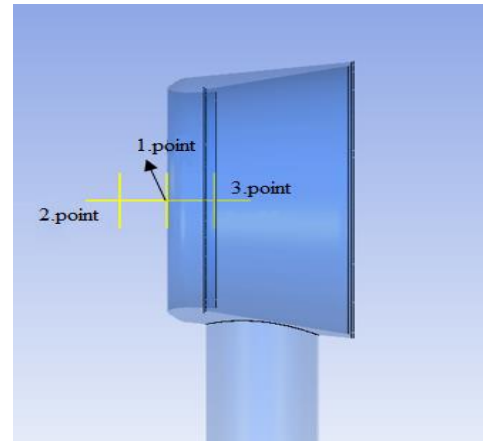
(a)

(b)
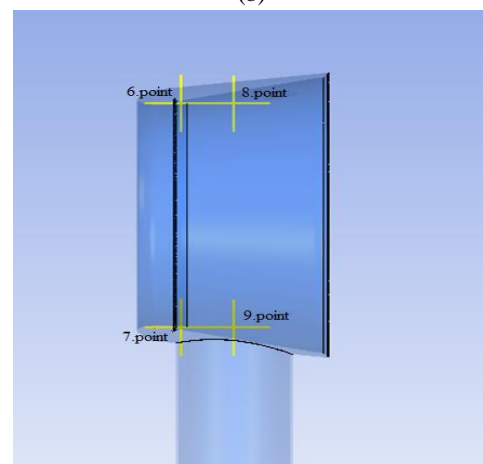
(c)

Figure 11. Microphone points of the NACA 0012 airfoil k-w turbulence model (a) 1.point, 2.point and 3.point, (b) 4.point and 5.point, (c) 6.point, 7.point, 8.point and 9.point
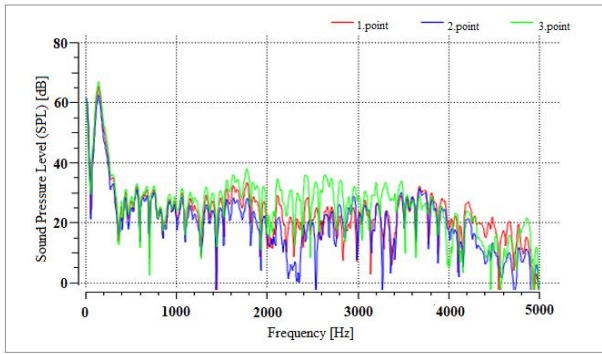
(a)
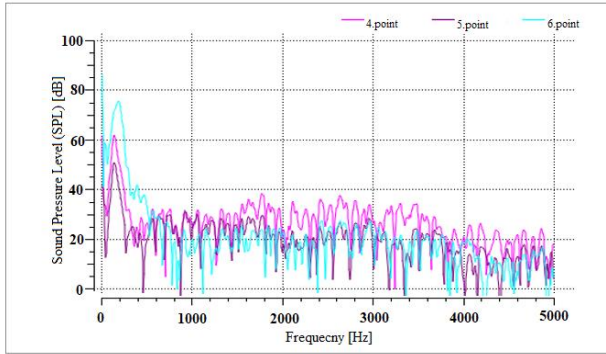
(b)
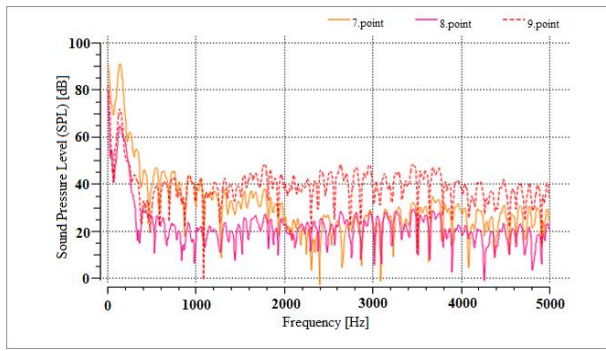
(c)

Şekil 12. According to the k-w turbulence model For 1.point, 2.point and 3.point, (a) 4.point,5.point and 6.point (b) 7.point, 8.point and 9.point (c) The effect of frequency on sound pressure level of points

Table 6. Sound pressure level

Points	Sound Pressure Level (dB)
1.point [mm]	97 dB
2.point [mm]	94 dB
3.point [mm]	98 dB
4.point [mm]	95 dB
5.point [mm]	90 dB
6.point [mm]	110 dB
7.point [mm]	120 dB
8.point [mm]	97 dB
9.point [mm]	105 dB

Sudden changes in the sound pressure level at high frequency values are due to the effect of eddy regions caused by pressure changes. Since the eddy represents the high energy in the flow field, the change in high frequencies increases the noise level due to the eddies.

4.2 Calculation of Sound Pressure Level with LES Model

Using LES turbulence model instead of the k-ω turbulence model in computational fluid dynamics allows to obtain more accurate solutions [10]. With models such as LES, large-scale eddy structures in the flow can be solved with the help of additional models (such as WALE Subgrid Scale, and Smagorinsky Subgrid Scale models), and the turbulence behavior can be solved mathematically at a rate of 90% directly [10]. Time dependent flow field analyzes were performed using LES turbulence model and FW-H acoustic analogy approach with ANSYS Fluent.

Figure 13 shows the values obtained from the microphones at the reference points at different frequencies.
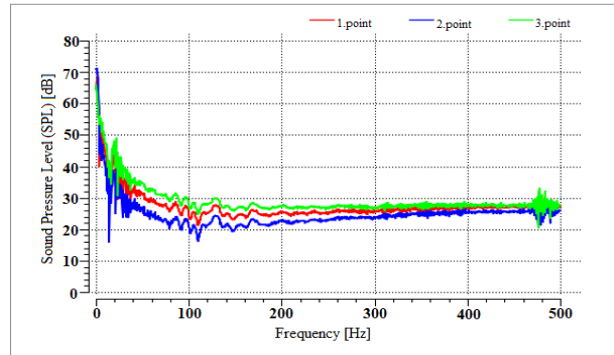
(a)
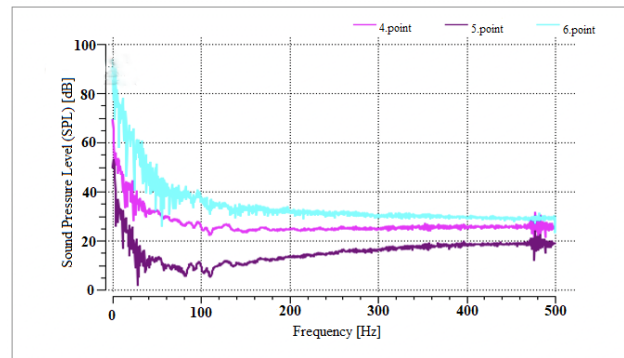
(b)
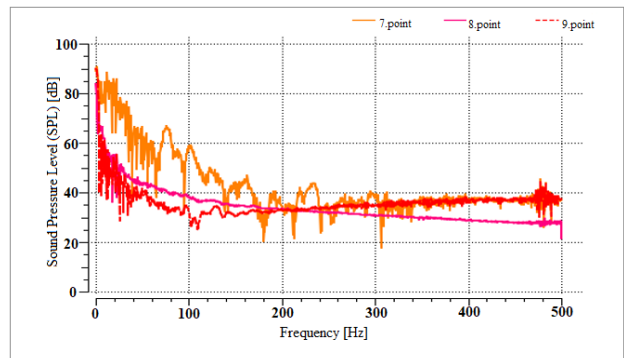
(c)
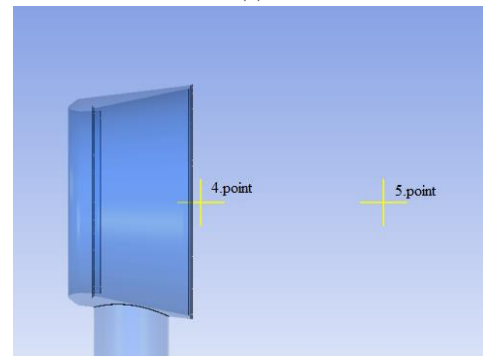
Figure 13 For the LES turbulence model, For 1.point, 2.point and 3.point, (a) for 4.point,5.point and 6.point (b) for 7.point, 8.point and 9.point (c) The effect of frequency on sound pressure level

Table 7. Sound Pressure Levels

Points	Sound Pressure Levels (dB)
1.point [mm]	70 dB
2.point [mm]	66 dB
3.point [mm]	72 dB
4.point [mm]	71 dB
5.point [mm]	57 dB
6.point [mm]	93 dB
7.point [mm]	98 dB
8.point [mm]	84 dB
9.point [mm]	81 dB

Table 7. demonstrates the sound pressure level at the microphone points. At 6th and 7th points, since air around the profile body has moved towards the low-pressure region, eddies have formed. According to the LES model calculation results; at the 6th and 7th points, the noise increased for high-frequency values. The noise level of the microphones at the 4th and 5th points showed a decrease of approximately 20 dB and 40 dB, respectively, from the noise levels at the 6th and 7th points. The lowest noise level was calculated as 57 dB at the 5th point. The value measured at the 2nd point has a lower noise value than the 1st point. As seen in microphones at 8th and 9th points, the velocity has a lower value compared to points 6 and 7. Therefore, the noise level has been reduced by about 13 dB. The rapid changes seen in the sound pressure level data at high-frequency values are due to the effect of pressure drops and eddy zones.

The results obtained from the calculations with k-ω at the 6th and 7th points, 22 dB higher sound pressure level was measured than the values calculated with the LES. The results obtained from the calculations with k-ω at the 1st point and the 2nd point, 28 dB higher sound pressure level was measured compared to the values calculated with the LES. The lowest sound pressure level was calculated at the 5th point in the solution with the k-ω turbulence model and LES model, and the results obtained from the calculation with the LES are 33 dB lower than the noise value calculated with the k-ω turbulence model. Points 4 and 5 are two points outside the air multiplier fan. The noise difference between calculations with the k-ω turbulence model and LES model is 24 dB at 4th point, and is 33 dB at 5th point, and is 26 dB at 3th point.
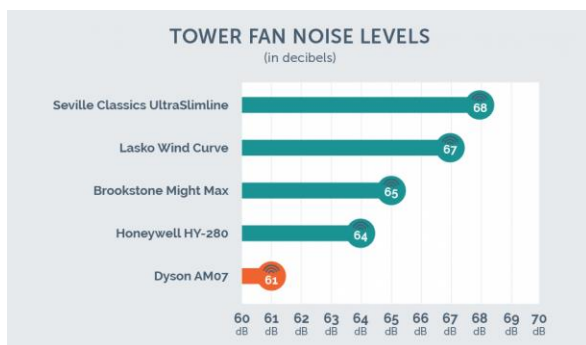
Figure 14. Fan Noise Level by Dyson company [2]

The results obtained with the LES method are more sensitive than the results calculated with the k-ω turbulence model. However, the solution time is longer. While the k-ω method solves turbulence by modeling, LES provides a direct solution. Therefore, the results of the calculations using the LES method are closer to the noise results announced by the Dyson company (Figure 14).

5. Conclusions

In this stud, three different air multiplier fan geometries were created based on NACA 0012, NACA1408, and EPPLER 1214 airfoils. As a result of the calculations made with CFD analysis, it was determined that the body profile providing the highest flow rate was NACA 0012. Using the ANSYS Response Surface optimization tool with seven geometric design parameters, a CFD-based study was conducted to determine the design that generates the least noise against the ratio of flow rate.

In the design that produces the least noise, the ratio of the output flow to the input flow is calculated as approximately 4.5. The geometry with the body profile of the bladeless fan determined as a result of this optimization was calculated using CFD analyzes and sound pressure level k-ω and LES turbulence models.

According to the results of these calculations, the noise decreases as the gap parameter value increases, the noise decreases as the angle of attack parameter value increases, the noise decreases as the width parameter value increases, the noise decreases up to a certain value of the length parameter value increases, then it has a constant value. The tail angle value increases, the noise decreases up to the 45º of the value of the parameter. As the diameter parameter increases, the noise decreases parabolically. When the value of the tail length parameter is up to 9 mm, the noise decreases and then increases.

By using the k-ω and LES method, the pressure distribution over 9 different microphones (observation) points were examined depending on time. It has been observed that the results obtained from the solutions made with the LES method are more sensitive and closer to the results announced by the Dyson company. The results obtained with the LES method showed that the determined design was usable.

Declaration

The authors declared no potential conflicts of interest with respect to the research, authorship, and/or publication of this article. The authors also declared that this article is original, was prepared in accordance with international publication and research ethics, and ethical committee permission or any special permission is not required.

Author Contributions

F. Yedekcioglu developed the methodology. S. Akyildiz performed the analysis. Z. Parlak supervised and improved the study. All authors wrote the manuscript together.

References

1. Bleier, F. P., *Fan Handbook: Selection, Application and Desing*. 1998, USA: McGraw-Hill.

2. Dyson UK. [cited 2020 20 June]; Available from: https://youtu.be/gChp0Cy33eY/.

3. Li, G., Hu, Y., Jin, Y., Setoguchi, T., and Kim, H. D., *Influence of Coanda surface curvature on performance of bladeless fan*. Journal of thermal science, 2014. **23**(5): p. 422-431.

4. Lasse, C. H., and Simon, H. T., *Flow Characteristics of the Dyson Air Multiplier*. Semantic Scholar, 2014. **14**(7).

5. Li, H., Deng, H. S., & Lai, Y. B., *Numerical and experimental research on the outlet flow field for the air multiplier*. Applied Thermal Engineering, 2016. **93**: p. 652-659.

6. Jafari, M., Afshin, H., Farhanieh, B., & Sojoudi, A., *Numerical investigation of geometric parameter effects on the aerodynamic performance of a Bladeless fan*. Alexandria Engineering Journal, 2016. **55**(1): p. 223-233

7. Zafer, B., Gürsoy, S., *Üflemeli kontrol sistemine sahip kanat kesitinin aeroakustik incelenmesi*. Uludağ Üniversitesi Mühendislik Fakültesi Dergisi, 2016. **21**(2): p. 237-256..

8. E. Kocak., E. Ayli., H.Turkoglu, *Kanat profili - silindir konfigürasyonunun aerodinamik ve aeroakustik performansinin sayisal analizi, in* 14th Ulusal Tesisat Mühendisliği Kongresi. 2019. İzmir: p. 908-917

9. İlter, Y.K., *İki Boyutlu Cisimler Etrafındaki Akım Gürültüsünün İncelenmesi*. 2014, İstanbul Teknik Üniversitesi, Fen Bilimleri Enstitüsü, Gemi İnşaatı ve Gemi Makinaları Mühendisliği Anabilim Dalı, Yüksek Lisans Tezi.

10. A.Bacak., A. Pinarbasi *Eksenel fan akustik performansinin sayisal olarak incelenmesi, in* 4th Uluslararasi Katilimli Anadolu Enerji Sempozyumu. 18-20 Nisan 2018. Edirne: p 798-804.

11. Li, A., *Characterization of Aerodynamic and Aeroacoustic Performance of Bladeless Fans*. 2019, Doctoral dissertation, Purdue University Graduate School.

12. Mehmood, K., Shahzad, A., Masud, J., Akram, F., Mumtaz, M. N., & Shams, T. A., *Numerical analysis of bladeless ceiling fan: An effective alternative to conventional ceiling fan*. Journal of Wind Engineering and Industrial Aerodynamics, 2022. **221**: 104905.

13. Ravi, D., & Rajagopal, T. K. R., *Numerical investigation on the effect of geometric shape and outlet angle of a bladeless fan for flow optimization using CFD techniques*. International Journal of Thermofluids, 2022. **15:** 100174.

14. Jafari, M., Sojoudi, A., & Hafezisefat, P., *Numerical study of aeroacoustic sound on performance of bladeless fan*. Chinese Journal of Mechanical Engineering, 2017. **30**(2): p. 483-494.

15. Li, H., Jin, X. H., Deng, H. S., & Lai, Y. B., *Experimental investigation on the outlet flow field structure and the influence of Reynolds number on the outlet flow field for a bladeless fan*. Applied Thermal Engineering, 2016. **100**: p. 972-978.

16. Joshi, V.; Noronha, W.; G, V.; Ramasamy, S.; K B, R. *Determination of Optimum Outlet Slit Thickness and Outlet Angle for the Bladeless Fan Using CFD*. Preprints, 2022. **2022110459**: p 1-17

17. Zhou, J., Hatami, M., Song, D., & Jing, D., *Design of microchannel heat sink with wavy channel and its time-efficient optimization with combined RSM and FVM methods*. International Journal of Heat and Mass Transfer, 2016. **103**: p. 715-724..

Research Article

Energy and exergy analysis in the ejector expansion refrigeration cycle under optimum conditions

Servet Giray Hacipasaoglu [a],* iD *, Ilhan Tekin Ozturk* [a] iD

[a]*Department of Mechanical Engineering, Faculty of Engineering, Kocaeli University, Kocaeli 41380, Turkey*

ABSTRACT

Refrigeration systems progress in parallel with the development of technology and the ways of saving energy in refrigeration systems are being researched. The literature suggests that incorporating ejectors in refrigeration systems can boost the coefficient of performance (COP) of the system. By utilizing ejector expansion, it is possible to improve the performance of the vapor compression refrigeration cycle (VCRC) by recapturing the expansion work that is typically lost during the expansion valve process. The present study investigation aims to contribute to the field of refrigeration by exploring the optimum pressure drop for three commonly utilized refrigerants. Specifically, the study scrutinizes the performance of an ejector based refrigeration cycle that incorporates a constant pressure mixing ejector. Utilizing the energy and exergy analyses are conducted to assess the system's performance with R134a, R600a, and R290 refrigerants across five distinct evaporator temperatures, namely 0°C, -5°C, -10°C, -20°C, and -30°C. The study further determines the optimum pressure drops in the secondary nozzle and the ejector area ratio at a specified condenser temperature, and examines the resultant total exergy destruction and exergy efficiency of the system. For R290 refrigerant; performance improvement ratio, decrease in total exergy destruction and exergy efficiency improvement ratios were found as 1.23, 54.02% and 22.97%, respectively. As a result, R290 is the most appropriate refrigerant for ejector expansion refrigeration cycle (EERC) among the refrigerants investigated as a result of the energy and exergy analyses.

1. Introduction

Refrigeration systems are preservation methods using in various applications that not only create a livable environment (commercial, residential vehicles, and buildings, etc.) but also serve to industrial sector, healthcare sectors etc. Therefore, performance improvements for the VCRC cover a wide range of applications. Reducing the throttling losses in the expansion valve is one of the methods to improve the system performance [1].

The conventional refrigeration cycle typically treats the expansion work that occurs during throttling as a form of energy loss. To compensate for this expansion work loss, it is conceivable to include a turbine instead of a throttling valve. However this is not practically possible. Instead, the ejector is preferred because of its simplicity, low cost and absence of moving parts [2]. One possible way to recover some of the kinetic energy lost during the expansion process in the VCRC is to replace the expansion valve with an ejector. By doing

so, the compressor suction pressure can be increased, leading to a reduction in compression work when compared to a conventional cycle.

Theoretical studies [3-7] and experimental studies [8-12] on refrigeration systems using ejectors instead of expansion valves presented that the COP is higher than the conventional systems. Ersoy and Bilir [13] performed an ejector system exergetically and examined the effects of ejector components on system performance. During their investigation, they observed that the efficiency of the ejector improved as the performance of the system increased, but this improvement was accompanied by a decrease in the ejector's area ratio. In their study, Bilir et al. [14] conducted a theoretical analysis of the COP in an ejector expander refrigerator, focusing on the influence of the refrigerant type on COP variations. The highest COP value was obtained for isobutane (R600a) among the refrigerants studied, followed by R134a. A modified VCRC utilizing an ejector as an expansion device was evaluated using three commonly used refrigerants:

R134a, R407C, and R410A. The study focused on analyzing the efficiency of the system, taking into account the condenser temperature of 35°C and evaporator temperature of 5°C. The results showed that the highest efficiency based on the second law was achieved under these conditions [15].

Gao et al. [16] studied a modified double evaporator EERC with R290. The study's findings indicate that the newly developed cycle exhibits superior energy and exergy performance compared to the conventional cycle. Specifically, the modified cycle's COP and exergy efficiency were observed to attain higher values than those of the conventional cycle under specific operating conditions.

A study conducted to compare ejector compression and VCRC found that at an evaporator temperature of 5°C and a condenser temperature of 40°C, the ejector compression system showed approximately 16% higher COP and second law efficiency compared to the VCRC system. Furthermore, the total exergy destruction observed in the VCRC was approximately 24% greater than that in the ejector expander cycle, given the same operating conditions [17].

Takleh and Zare [18] introduced a new EERC and performed a thermodynamic analysis using the first and second laws of thermodynamics with six different refrigerants: R134a, R236fa, R227ea, R500, R1234yf, and R1234ze. The authors found that, of the refrigerants examined, R1234ze exhibited 5.7% and 15.5% higher exergy efficiency compared to the conventional EERC and conventional VCRC, respectively, when operating at 40°C condenser temperature and 5°C evaporator temperature.

Cui et al. [19] proposed a new ejector-supported dual-evaporator refrigeration cycle for household refrigerator applications. According to their analysis results, the new cycle showed a 7.7% and 5.5% increase in the coefficient of performance and volumetric cooling capacity, respectively, compared to the split-ejector cycle with condenser output. Furthermore, the new cycle exhibited a 57% and 58% increase in these parameters, respectively, compared to the classical VCRC.

For household refrigerator/freezer applications, Chen et al. [20] introduced an ejector vapor compression refrigeration cycle (EVRC) that utilizes a zeotropic hydrocarbon mixture of R290/R600a. When compared to the classical VCRC, the new cycle showed significant improvements of 13.5%, 19.3%, and 13.4% in its coefficient of performance, volumetric cooling capacity, and exergy efficiency, respectively.

Bai et al. [21] conducted an experimental investigation of an ejector-automatic cascading refrigeration cycle that employed a zeotropic refrigerant mixture of R134a/R23. They conducted performance comparisons between the ejector cycle and two classical refrigeration cycles under selected operating conditions.

According to the authors, the ejector cycle demonstrated notable benefits in terms of achieving lower cooling temperatures and higher energy utilization efficiency when compared to conventional cycles. Specifically, the improvements in the COP and exergy efficiency of the ejector cycle were observed to be 9.6% and 25.1%, respectively.

Jeon et al. [22] researched the performance traits of a household refrigerator-freezer using R600a refrigerant with a condenser split ejector refrigeration cycle. To investigate the impact of entrainment ratio on pressure lift effect, mass flow rate variation, and performance coefficient improvement, the authors employed a test rig. Their findings revealed that, for comparable cooling capacity conditions, the COP of the condenser split ejector cycle could be enhanced by up to 11.4% when the entrainment ratio reached 0.18, as compared to conventional cycles.

The primary purpose of incorporating an ejector in the EERC is to minimize the level of irreversibility that typically occurs during the throttling process. When an ejector is used as an expansion valve in a refrigeration system, it is crucial to conduct an exergy analysis to determine the extent to which the irreversibility is reduced in the system and its components. By applying exergy analysis, it becomes possible to assess the irreversibilities that arise within energy systems, identify their origins, magnitudes, and distribution, and consequently, devise strategies for efficient energy utilization [23]. Despite this result, possibilities to improve performance should be investigated by using different fluids and, if any, different methods.

The purpose of this study and how it differs from previous studies in the literature is to find the optimum pressure drop for different evaporator temperatures and three different refrigerants, to perform exergy analysis for the optimum situation, and to determine the losses in each component in the system. During the analyses, optimum pressure drops were determined for each evaporator temperature, and each component's exergy destruction was examined. The originality of this study lies in determining the optimum pressure drop for R134a, R600a, and R290 refrigerants in a constant pressure mixing ejector at evaporator temperatures of 0, -5, -10, -20, and -30°C, and continuing with exergy analysis using these optimum pressure drops. In this context, while the optimum pressure drop is found; the pressure lift ratio, performance improvement ratio created by the use of the ejector system, and the ejector area ratio, which determines the ejector design parameter, based on the pressure drop in the secondary nozzle were obtained.

2. Thermodynamics Model and System Description

Figure 1 and Figure 2 demonstrate the operating schematic presentation of VCRC and EERC, respectively. As seen from these figures, the EERC is an improvement of the VCRC due to the addition of a vapor-liquid separator instead of the expansion valve, as well as an ejector to minimize throttling losses.

Figure 3 illustrates the P-h diagram obtained for the R600a refrigerant at -30°C evaporator temperature in the VCRC, and Figure 4 indicates the P-h diagram obtained for the EERC at -30°C evaporator temperature using the R600a refrigerant.
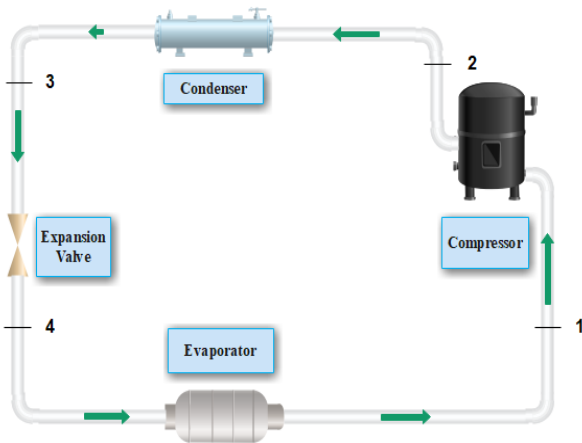
Figure 1. Schematic presentation of VCRC
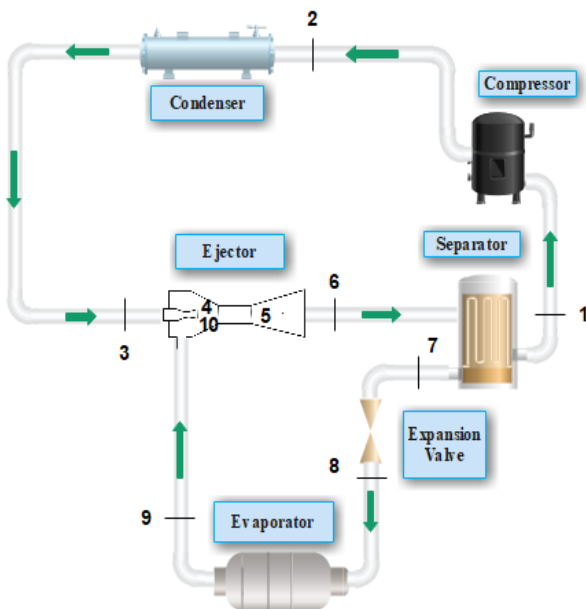
Figure 2. Schematic presentation of EERC
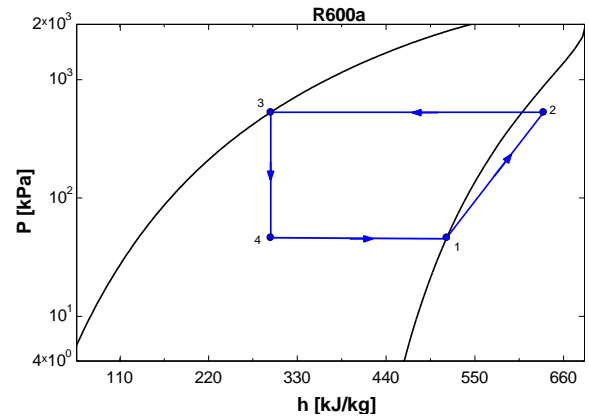
Figure 3. P-h diagram for R600a refrigerant of the VCRC.
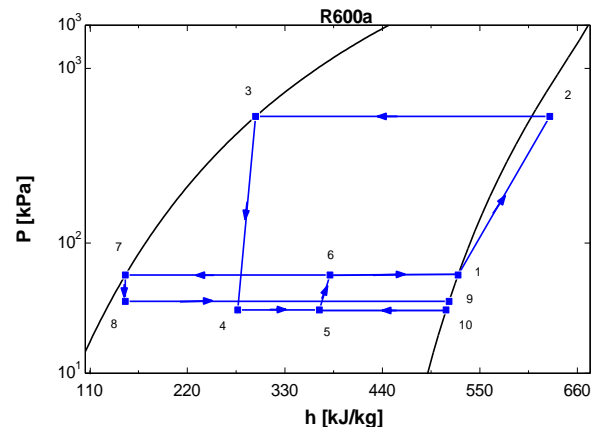
Figure 4. P-h diagram for R600a refrigerant of the EERC

This research involved the development of a thermodynamics model using a FORTRAN code specifically designed for EERC that utilizes a constant pressure ejector. The thermodynamic states of the refrigerants were obtained using REFPROP version 9.1. The model incorporates the conservation equations for mass, momentum, and energy. The thermodynamic properties of each point in the cycle were determined by considering the isentropic efficiency values for the irreversibilities in the ejector and compressor. The equations required for (constant pressure mixing) CPM modeling were used and the efficiency was assumed to be 100% for the separator (steam-liquid separator) [24]. The performance improvement ratio, ejector area ratio, and pressure lift ratio were calculated using the following methods:

Equations (1-3) are utilized to define the functioning of the motive nozzle of the ejector. Similarly, equations (4-6) are employed to represent the operations occurring in the secondary nozzle of the ejector. Moreover, equations (7-8) capture the mathematical relationships utilized to model the behavior of the ejector during constant pressure mixing. Lastly, equations (9-10) are utilized to define the functioning of the diffuser section of the ejector at the outlet. [24].

Table 1. CPM Ejector theory equations

	CPM Ejector Theory Equations
Eq. (1)	$\eta_{mn} = \dfrac{h_{mn,out} - h_{mn,in}}{h_{mn,out,s} - h_{mn,in}}$
Eq. (2)	$V_{mn,out} = \sqrt{2(h_{mn,in} - h_{mn,out})}$
Eq. (3)	$a_{mn} = \dfrac{v_{mn,out}}{V_{mn,out}(1 + w)}$
Eq. (4)	$\eta_{sn} = \dfrac{h_{sn,out} - h_{sn,in}}{h_{sn,out,s} - h_{sn,in}}$
Eq. (5)	$V_{sn,out} = \sqrt{2(h_{sn,in} - h_{sn,out})}$
Eq. (6)	$a_{sn} = \dfrac{v_{sn,out}}{V_{sn,out}(1 + w)}$
Eq. (7)	$V_{diff,in(mix,out)} = rV_{mn,out} + (1 - r)V_{sn,out}$
Eq. (8)	$h_{diff,in(mix,out)} = rh_{mn,in} + (1 - r)h_{sn,in} - \dfrac{V_{diff,in}^2}{2}$
Eq. (9)	$h_{diff,out} = \dfrac{h_{mn,in} + wh_{sn,in}}{1 + w}$
Eq. (10)	$h_{diff,out} = \dfrac{h_{mn,in} + wh_{sn,in}}{1 + w}$

With the help of the COP of VCRC and EERC, the performance of these two cycles can be compared with the help of Eq. (11).

$$R = \frac{COP_{EERC}}{COP_{VCRC}} \tag{11}$$

The area ratio given by Eq (12) is an important parameter obtained as a result of thermodynamic analysis for ejector designs.

$$A_r = \frac{a_{m,out} + a_{s,out}}{a_{m,out}} \tag{12}$$

The pressure lift ratio is determined as the ratio between the outlet pressure of the ejector and the pressure of the secondary fluid that enters the ejector, and it can be calculated by using Equation (13). The secondary flow is the flow out of the evaporator.

$$P_{lr} = \frac{P_{diff,out}}{P_{sn,in}} \tag{13}$$

Mass ratio is a parameter obtained from the entrainment ratio and is determined by Eq. (14) [24]. The primary flow is the flow out of the condenser.

$$r = \frac{m_{primary\ flow}}{m_{total}} \tag{14}$$

The reference state is denoted by a subindex of 0, an atmospheric pressure of 101.325 kPa, and 25°C ambient temperature are accepted for this study. To estimate the exergy for each component of the EERC, the mass flow rate per unit mixture in the ejector is used (Eq. 15).

$$E_i = [(h_i - h_0) - T_0(s_i - s_0)]m_i \tag{15}$$

When $i = 1, 2, 3, 4$, $m_i = r$

When $i = 5, 6$, $m_i = 1$

When $i = 7, 8, 9, 10$, $m_i = 1 - r$

The exergy losses in each component of the EERC can be obtained with the following equations (Eq. 16-20):

For compressor:

$$Ex_{comp} = (E_1 - E_2) + W_{comp} \tag{16}$$

For condenser:

$$Ex_{cond} = E_2 - E_3 \tag{17}$$

For evaporator:

$$Ex_{evap} = (E_8 - E_9) + \left[Q_{evap}\left(1 - \frac{T_0}{T_l}\right)\right] \tag{18}$$

$$T_l = T_{evap} + 5$$

For ejector:

$$Ex_{ejector} = E_3 + E_9 - E_6 \tag{19}$$

For expansion valve:

$$Ex_{exp} = E_7 - E_8 \tag{20}$$

The total exergy destruction in the system can be determined by summing up the exergy destruction of each individual component using Equation (21).

$$Ex_{total} = Ex_{comp} + Ex_{cond} + Ex_{evap} + Ex_{ejector} + Ex_{exp} \tag{21}$$

The exergy efficiency of the EERC is determined with the Eq. (22).

$$\Psi_{ej} = 1 - \frac{Ex_{tot}}{W_{comp}} \tag{22}$$

3. Operation Conditions and Model Validation

The operating conditions in the analyses are given in Table 2. Five different temperatures (0°C, -5°C, -10°C, -20°C, -30°C) were determined for the evaporator.

Table 2. Operation conditions for analyses

Evaporator temperature T_e [°C]	0, -5, -10, -20, -30
Condenser temperature T_c [°C]	40
Compressor isentropic efficiency (η_{comp})	0.75
Primary nozzle isentropic efficiency (η_m)	0.9
Secondary nozzle isentropic efficiency (η_s)	0.9
Diffuser isentropic efficiency (η_d)	0.8

Some general physical properties of R600a, R134a, and R290 are provided in Table 3.

Table 3. Physical properties of R600a, R134a and R290 [25]

Refrigerants	R600a	R134a	R290
Chemical name	Isobutane	1,1,1,2-Tetrafloretan	Propane
Molar mass (g/mol)	58.12	102.03	44.1
Normal boiling Point (°C)	-11.75	-26.07	-42.1
Critical temperature (°C)	134.66	101.06	96.74
Critical pressure (MPa)	3.629	4.059	4.251
Safety class	A3	A1	A3
ODP	0	0	0
GWP	4	1301	3

Figure 5 illustrates the comparison between the model created in this study and the reference model of under the same operating conditions (T_{cond} = 40°C, η_{mn} = η_{sn} = 0.9, η_{comp} =0.75) using R134a as the refrigerant [26]. This comparison was performed to investigate COP with a changing evaporator temperature, with an inconsistency of 1.03%.

Figure 6 demonstrates the calculation procedure for the thermodynamic modeling of the ejector with iterative solution method.

4.   Results and Discussion

Graphs of the changes in pressure lift ratio and performance improvement ratio were obtained to determine the optimum pressure drop using a constant pressure ejector for three different refrigerants while considering the basic factors affecting the performance of the ejector. Exergy analyses are performed with the pressure drops determined by these parameters.
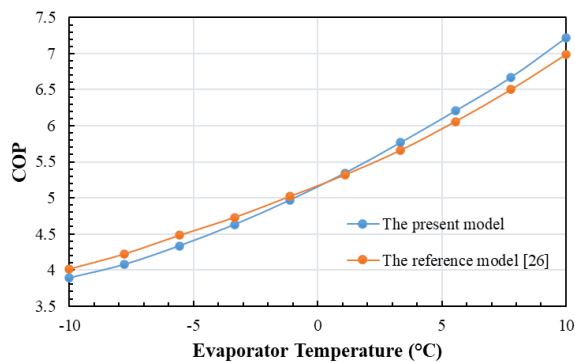
Figure 5. Comparison of the current model with (Yadav and Neeraj, 2018)
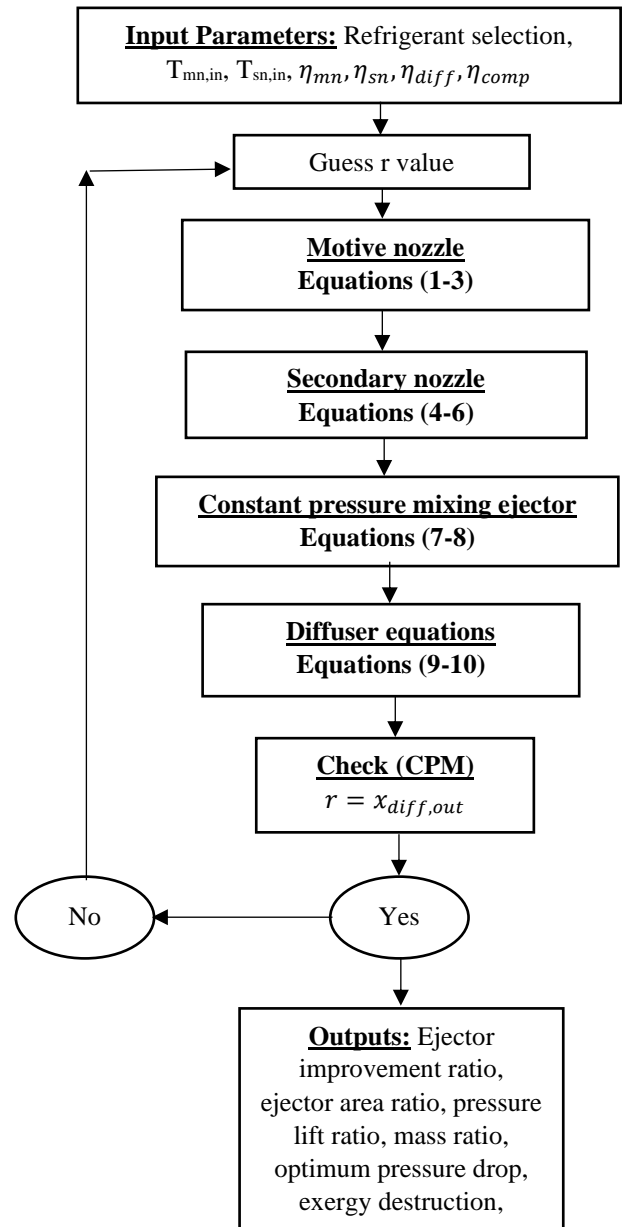
Figure 6. Flow chart of computation procedure

Figure 7-9 demonstrate the graphs obtained as a result of thermodynamic analyses using R600a refrigerant. Figure 7 displays the change in pressure lift ratio depending on the pressure drop in the secondary nozzle. The pressure lift ratio in the ejector is an important performance parameter. The higher this ratio, the higher the system performance. Because the compression work required is reduced. The aforementioned statement implies a discussion about an EERC, wherein a reduction in the compressor's work requirement could lead to an enhancement in the COP of the EERC.

In the given context, it is stated that the pressure drop at the maximum pressure lift ratio has been observed to be 5 kPa for R600a refrigerant at evaporator temperatures of 0°C, -10°C, -20°C, and -30°C. For -5°C evaporator temperature, the optimum pressure drop is approximately 9 kPa. Figure 7 and Figure 8 are actually

graphs that support each other, as an increase in the pressure lift ratio means an increase in the system performance improvement ratio. The maximum value reached in the system performance improvement ratio was obtained as approximately 1.22 with a pressure drop of 5 kPa for -30°C evaporator temperature. After approximately 35 kPa pressure drop value for -30°C evaporator temperature, the performance improvement ratio decreased below 1 and has no advantage over VCRC. Looking at the same graph for -20°C evaporator temperature, it has been seen that the performance improvement ratio drops below 1 after a pressure drop of 50 kPa. This situation is also reflected in Figure 9 of the ejector area ratio graph. For evaporator temperatures of 0, -10, -20, -30°C, the optimum ejector area ratio can be found from Figure 9 by considering the optimum pressure drop amounts found in Figure 7 and Figure 8. The area ratios for each evaporator temperature are: 8.144 for 0°C, 5.85 for -5°C, 6.933 for -10°C, 5.852 for -20°C, 4.892 for -30°C.

Figure 10-12 illustrates the graphs acquired as a result of thermodynamic analyses using R134a refrigerant. For R134a refrigerant, the pressure drop with the maximum pressure lift ratio for evaporator temperatures of 0, -5 and -10°C is 15 kPa. It is approximately 14 kPa for -20°C evaporator temperature and 12 kPa for -30°C evaporator temperature.

Figure 9. Variation of the ejector area ratio with the pressure drop in the secondary nozzle.

The maximum value reached in the system performance improvement ratio was obtained as approximately 1.221 with a pressure drop of 12 kPa for -30°C evaporator temperature. There is no case where the performance improvement ratio or the pressure lift ratio falls below 1 for the pressure drop values observed. The area ratios for each evaporator temperature are: 6.573 for 0°C, 6.082 for -5°C, 5.616 for -10°C, 4.892 for -20°C, 4.358 for -30°C.
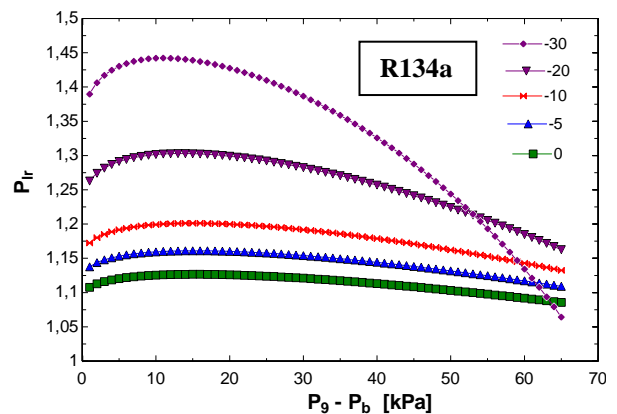
Figure 10. Variation of pressure lift ratio with pressure drop in secondary nozzle.

Figure 7. Variation of pressure lift ratio with pressure drop in secondary nozzle.

Figure 8. Variation of the performance improvement ratio with the pressure drop in the secondary nozzle.
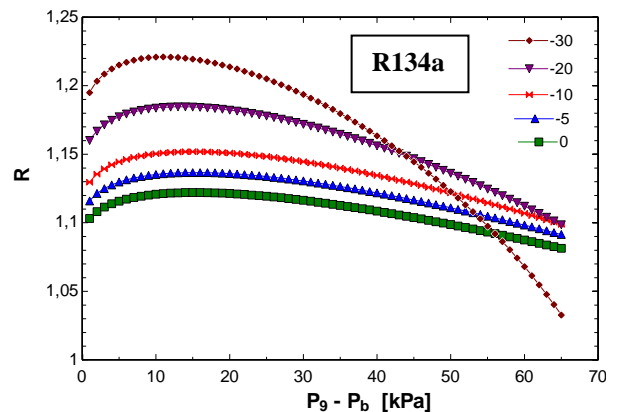
Figure 11. Variation of the performance improvement ratio with the pressure drop in the secondary nozzle.
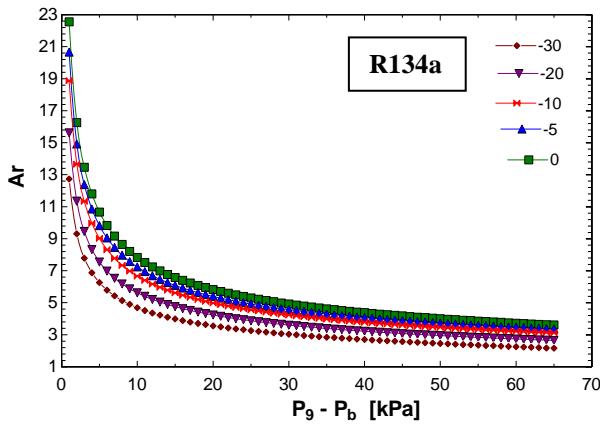
Figure 12. Variation of the ejector area ratio with the pressure drop in the secondary nozzle.

Under the conditions of a -30°C evaporator temperature and a 12 kPa pressure drop, the system performance improvement ratio for R134a refrigerant was found to be 1.221, the highest value obtained. The system performance improvement ratio for R600a refrigerant was found to be highest at approximately 1.22 under the conditions of a -30°C evaporator temperature and a 5 kPa pressure drop.

Figure 13, Figure 14, and Figure 15 indicate the graphs obtained as a result of thermodynamic analyses using R290 refrigerant. For R290 refrigerant, the pressure drop with the maximum pressure lift ratio for 0, -5, -10, -20, and -30°C evaporator temperatures is 20 kPa. The highest value obtained in the system performance improvement ratio was obtained as approximately 1.23 with a pressure drop of 20 kPa for -30°C evaporator temperature. The ejector area ratios for each evaporator temperature are: 6.705 for 0°C, 6.286 for -5°C, 5.881 for -10°C, 5.121 for -20°C, 4.424 for -30°C.

The maximum system performance improvement ratio for R134 refrigerant was achieved under the conditions of a -30 °C evaporator temperature and a 12 kPa pressure drop, with a value of 1.221.
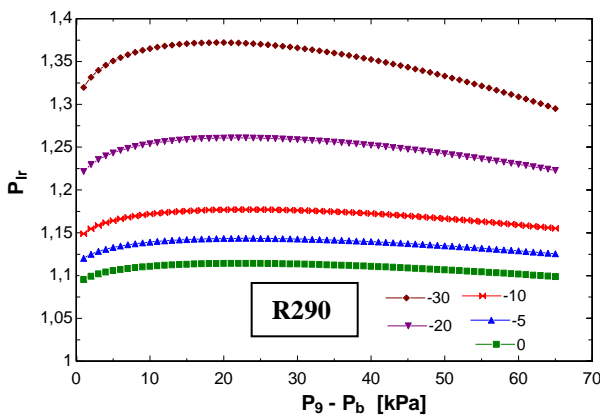
Figure 13. Variation of pressure lift ratio with pressure drop in secondary nozzle.
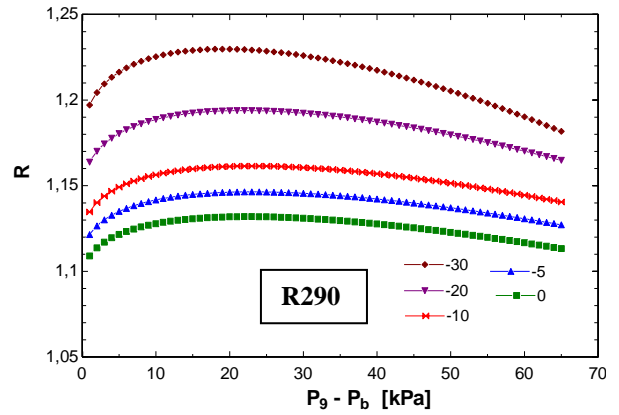
Figure 14. Variation of the performance improvement ratio with the pressure drop in the secondary nozzle.
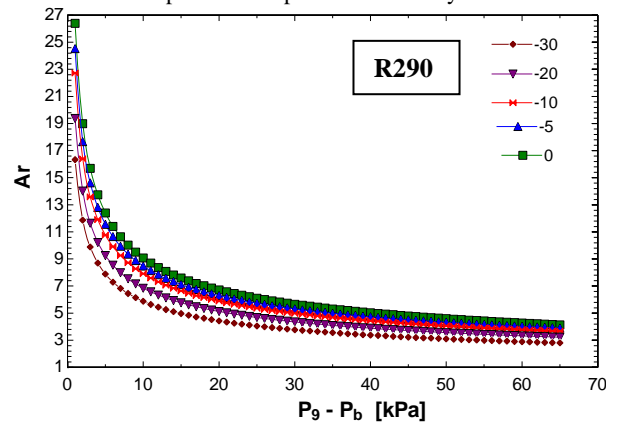
Figure 15. Variation of the ejector area ratio with the pressure drop in the secondary nozzle.

Under the conditions of a -30°C evaporator temperature and a 5 kPa pressure drop, the maximum value attained for the system performance improvement ratio of R600a refrigerant was approximately 1.22. The maximum value obtained in the system performance improvement ratio for R290 refrigerant was obtained as approximately 1.23 with a pressure drop of 20 kPa for -30°C evaporator temperature.

The primary objective of the ejector is to minimize irreversibility in the system. In the EERC and VCRC, the exergy analyses conducted in this study solely considered physical exergy, neglecting chemical, kinetic, and potential exergy.

Figure 16-21 present how the use of ejectors in the cycle will lead to a reduction in the amount of irreversibility in each component and the overall system. Exergy destruction values for each component and the overall system were computed in Figure 16 and Figure 17, utilizing the optimum pressure drop values identified earlier for R134a refrigerant at evaporator temperatures of -5°C and -30°C. For R134a, the optimum pressure drop values for evaporator temperatures of -5 and -30°C are 15 and 12 kPa, respectively. When utilizing R600a refrigerant, the optimum pressure drop values for evaporator temperatures of -5°C and -30°C are determined to be 9 kPa and 5 kPa, respectively. In the

use of R290 refrigerant, the optimum pressure drop value for evaporator temperatures of -5 and -30°C is 20 kPa.

It has been calculated that the amount of exergy destruction occurring in each element of the ejector system is less than in the conventional vapor compression system. Based on the exergy analysis outcomes presented in Figure 16 for the evaporator temperature of -5°C, employing R134a refrigerant, the total exergy destruction value for the VCRC was determined to be 26.92 kJ/kg, whereas the EERC recorded a total exergy destruction value of 13.10 kJ/kg. As per the results, the total exergy destruction of the EERC reduced by 51.34% in comparison to the VCRC. The exergy destruction attributed to the expansion valve in the VCRC is calculated as 6.032 kJ/kg, whereas the EERC's expansion valve exergy destruction value is computed to be 0.0322 kJ/kg. Due to its negligible value, the expansion valve exergy destruction for the EERC was excluded from the chart.

Based on the exergy analysis outcomes presented in Figure 17 for the -30°C evaporator temperature using R134a refrigerant, the total exergy destruction values for the VCRC and EERC were determined to be 44.352 kJ/kg and 20.47 kJ/kg, respectively. The findings indicate that the total exergy destruction in the EERC was reduced by 53.84% when compared to that of the VCRC.

Upon analyzing the exergy outcomes presented in Figure 18 for the -5°C evaporator temperature with R600a refrigerant, the total exergy destruction of the VCRC was determined to be 47.22 kJ/kg, while the EERC registered a total exergy destruction value of 23.18 kJ/kg. Accordingly, the total exergy destruction of the EERC decreased by 50.91% compared to the VCRC.

In view of the exergy analysis results for -30°C evaporator temperature using R600a refrigerant in Figure 19, the total exergy destruction of the VCRC was calculated to be 75.97 kJ/kg, while the total exergy destruction of the EERC was determined to be 35.37 kJ/kg. Accordingly, the total exergy destruction of the EERC decreased by 53.44% compared to the VCRC.

Considering the exergy analysis outcomes presented in Figure 20 for the -5°C evaporator temperature utilizing R290 refrigerant, the total exergy destruction values for the VCRC and EERC were determined to be 51.91 kJ/kg and 25.04 kJ/kg, respectively. Based on the results, the total exergy destruction of the EERC decreased by 51.75% in comparison to the VCRC.

The exergy analysis results for R290 refrigerant and an evaporator temperature of -30°C showed that the total exergy destruction of the VCRC was 85.13 kJ/kg, whereas the total exergy destruction of the EERC was found to be 38.99 kJ/kg. Hence, the total exergy

destruction in the EERC decreased by 54.20% compared to that of the VCRC.

In conclusion, upon comparing the exergy destruction values obtained from the analyses conducted for six different scenarios presented in Figures 16-21 for both VCRC and EERC, the most significant decrease of 54.20% was observed when using R290 refrigerant with a -30°C evaporator temperature.

	Compressor	Condenser	Evaporator	Expansion Valve	Ejector	Total Exergy Destruction
VCRC (kJ/kg)	9.151	9.002	2.738	6.032	0	26.923
EERC(kJ/kg)	4.781	5.144	1.62	0.0322	1.53	13.1072
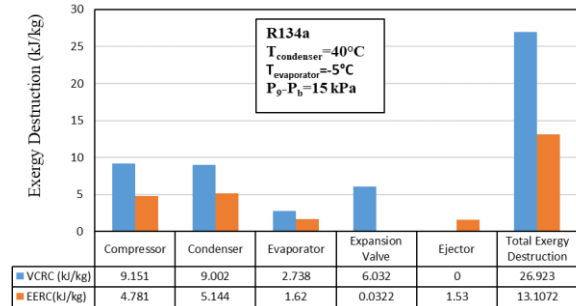
Figure 16. Comparison of EERC and VCRC exergy destruction amounts (R134a, T_{evap}=-5°C)

	Compressor	Condenser	Evaporator	Expansion Valve	Ejector	Total Exergy Destruction
VCRC (kJ/kg)	15.52	10.56	2.962	15.31	0	44.352
EERC(kJ/kg)	8.274	6.142	1.907	0.08959	4.06	20.47259
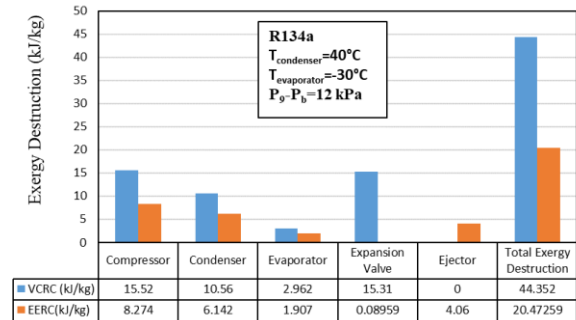
Figure 17. Comparison of EERC and VCRC exergy destruction amounts (R134a, T_{evap}=-30°C)

	Compressor	Condenser	Evaporator	Expansion Valve	Ejector	Total Exergy Destruction
VCRC (kJ/kg)	16.63	15.63	4.958	10.01	0	47.228
EERC(kJ/kg)	8.712	8.975	2.924	0.04301	2.532	23.18601
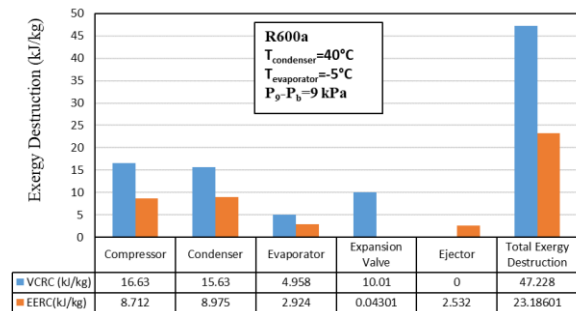
Figure 18. Comparison of EERC and VCRC exergy destruction amounts (R600a, T_{evap}=-5°C)

	Compressor	Condenser	Evaporator	Expansion Valve	Ejector	Total Exergy Destruction
VCRC (kJ/kg)	28	16.89	5.226	25.86	0	75.976
EERC(kJ/kg)	14.96	10.07	3.365	0.1374	6.841	35.3734
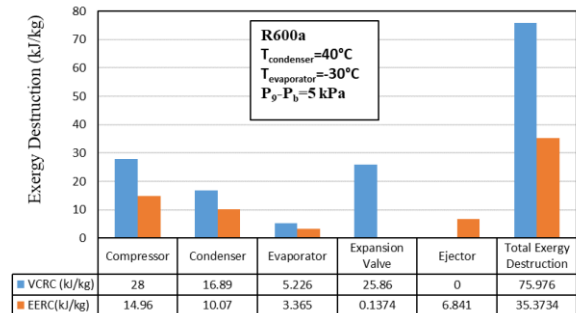
Figure 19. Comparison of EERC and VCRC exergy destruction amounts (R600a, T_{evap}=-30°C)
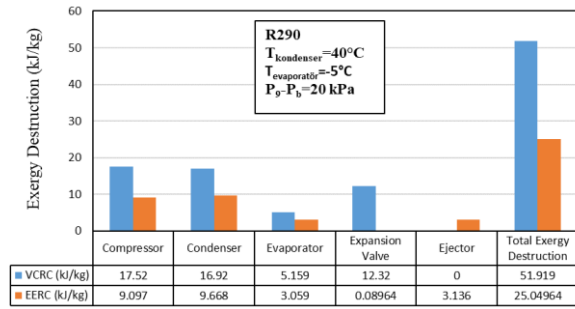
Figure 20. Comparison of EERC and VCRC exergy destruction amounts (R290, T_{evap}=-5°C)
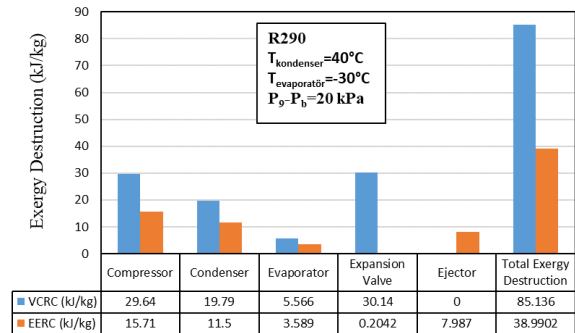
Figure 21. Comparison of EERC and VCRC exergy destruction amounts (R290, T_{evap}=-30°C)

Figures 22-23-24 exhibit how the exergy efficiency improvement ratio changes with the condenser temperature for R134a, R600a, and R290 refrigerants, respectively. As the condenser temperature increases, the rate of exergy efficiency improvement ratio also increases. Upon analyzing the situation for a single evaporator temperature, it can be noticed that the losses in the expansion valve rise as the pressure differential between the condenser and evaporator grows, which is directly proportional to the increase in the condenser temperature. Utilizing an ejector instead of the expansion valve in a refrigeration system can lead to an increase in the recycling rate of losses and thereby result in an improvement in the exergy efficiency improvement ratio. The exergy efficiency improvement ratios for R134a, R600a, and R290 refrigerants at a condenser temperature of 40°C were found to be 22.09%, 20.74%, and 22.97%, respectively. Therefore, the highest increase in terms of exergy efficiency improvement ratio was achieved with R290 refrigerant.

In Figure 25, the variation of the COP value of the EERC depending on the pressure drop in the ejector is given for R134a, R600a, R290 used in this study and R134a used in the reference model. As a result of the comparative energy and exergy analyzes for the fluids used in the study, the use of R290 refrigerant was suggested. For R290 refrigerant, the COP was found to be 6.33 at a pressure drop of 15 kPa, for R600a refrigerant at a pressure drop of 10 kPa, COP 6.243, and for R134a at a pressure drop of 25 kPa, COP was found

to be 6.182. The comparison of the COP was conducted by using the graph, which takes into account the previous study in the literature that utilized R134a refrigerant. The results of this study were validated, and it was highlighted that R290 refrigerant is the preferred option among these refrigerants (T_{cond} = 40°C, T_{evap} = 5°C, $\eta_{mn} = \eta_{sn} = 0.9$, $\eta_{comp} = 0.75$).
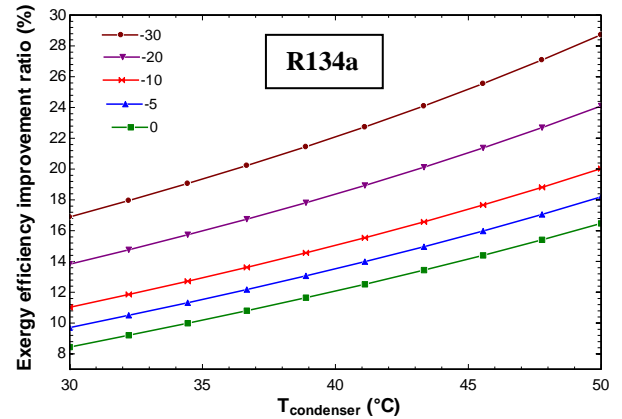
Figure 22. Alteration of the exergy efficiency improvement ratio with condenser temperature for R134a refrigerant
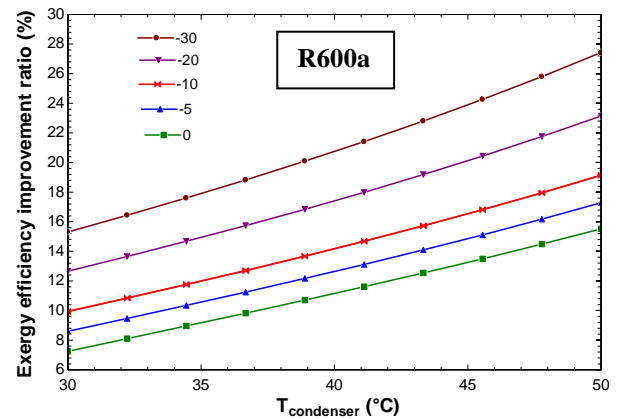
Figure 23. Alteration of exergy efficiency improvement ratio with condenser temperature for R600a refrigerant
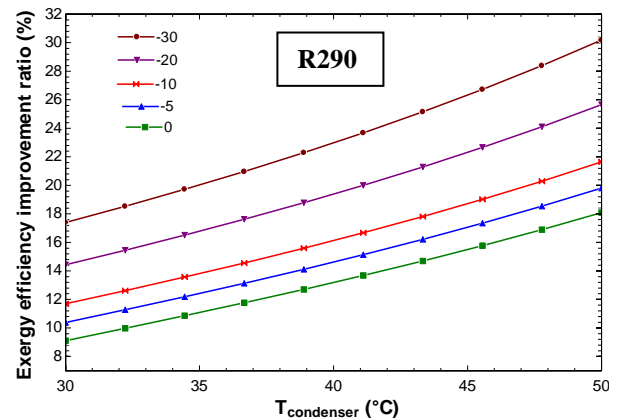
Figure 24. Alteration of exergy efficiency improvement ratio with condenser temperature for R290 refrigerant
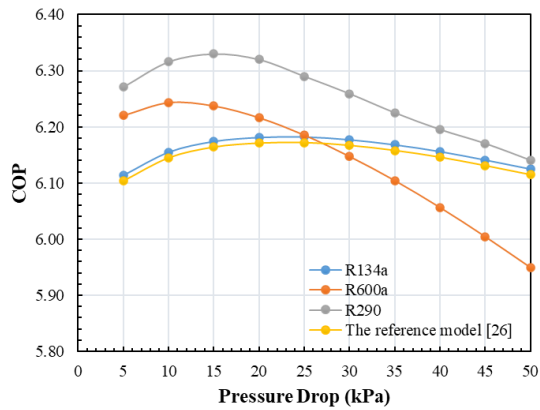
Figure 25. Alteration of pressure drop with COP

5. Conclusions

In VCRC, the use of ejectors in the system has been investigated in order to reduce the losses caused by the expansion valve and to reduce the work spent on the compressor. EERC energy and exergy analyses based on the constant pressure ejector flow model were performed. The present study focused on determining the optimum pressure drop in the secondary nozzle and corresponding ejector area ratio, total exergy destruction values, and exergy efficiency improvement ratio for a given condenser temperature. In addition, energy and exergy analyses were conducted for five different evaporator temperatures using three different refrigerants at optimum conditions. The study yielded the following findings:

- For R134a refrigerant, the pressure drop with the maximum pressure lift ratio for evaporator temperatures of 0, -5 and -10°C is 15 kPa. It is approximately 14 kPa for -20°C evaporator temperature and 12 kPa for -30°C evaporator temperature. The maximum value reached in the system performance improvement ratio was obtained as approximately 1.221 with a pressure drop of 12 kPa for -30°C evaporator temperature. It was obtained as approximately 1.13 with a pressure drop of 15 kPa for -5°C evaporator temperature.

- For R600a refrigerant, the pressure drop with the maximum pressure lift ratio for evaporator temperatures of 0, -10, -20 and -30 °C is 5 kPa. For an evaporator temperature of -5 °C, it is approximately 9 kPa. The maximum value reached in the system performance improvement ratio was obtained as approximately 1.22 with a pressure drop of 5 kPa for -30°C evaporator temperature. It was obtained as approximately 1.13 with 9 kPa pressure drop for -5°C evaporator temperature.

- For R290 refrigerant, the pressure drop with the maximum pressure lift ratio for 0, -5, -10, -20, and -30°C evaporator temperatures is 20 kPa. The maximum value reached in the system performance

improvement ratio was obtained as approximately 1.23 with a pressure drop of 20 kPa for -30°C evaporator temperature.

- When comparing the exergy destruction values obtained from the exergy analyses for six different cases, it was found that the greatest decrease in total exergy destruction of the system was achieved when R290 refrigerant was used and the evaporator temperature was set to -30°C, resulting in a reduction of 54.02% for both EERC and VCRC. Also, as a result of the analyses made to determine the increase in exergy efficiency, the highest exergy efficiency improvement ratio was obtained in R290 refrigerant. As a result of the energy and exergy analyses, it can be concluded that R290 is the most suitable refrigerant for EERC among the refrigerants investigated.

- In the further studies; Thermoeconomic analysis using R290 refrigerant and performance analysis of other environmentally friendly fluids for EERC can be recommended.

Declaration

The authors declared no potential conflicts of interest with respect to the research, authorship, and/or publication of this article. The authors also declared that this article is original, was prepared in accordance with international publication and research ethics, and ethical committee permission or any special permission is not required.

Author Contributions

İ. T. Öztürk developed the methodology. S. G. Hacıpaşaoğlu performed the analysis. İ. T. Öztürk supervised and improved the study. S. G. Hacıpaşaoğlu and İ. T. Öztürk wrote the manuscript together. İ. T. Öztürk proofread the manuscript.

Nomenclature

A_r	:Area ratio
h	:Specific Enthalpy [kJ/kg]
m	:Mass [kg]
mn	:Primary nozzle
o	:Reference situation
out	:Outlet
P	:Pressure [kPa]
P_b	:Mixing pressure [kPa]
P_{lr}	:Pressure lift ratio
r	:Mass ratio
R	:Performance improvement ratio
s	:Specific Entropy [kJ/kgK]
sn	:Secondary nozzle
T	:Temperature [°C]
tot	:Total

Greek symbols

W	:Work per unit mass [kJ/kg]
η	:Isentropic efficiency
Ψ	:Exergy efficiency improvement ratio

Abbreviations

1, 2, 3, .	:State points
comp	:Compressor
cond	:Condenser
COP	:Coefficient of Performance
CPM	:Constant Pressure Mixing
diff	:Diffuser
E	:Exergy [kJ/kg]
EERC	:Ejector Expansion Refrigeration Cycle
evap	:Evaporator
Ex	:Exergy destruction [kJ/kg]
exp	:Expansive valve
GWP	:Global Warming Potential
in	:Inlet
ODP	:Ozone Depletion Potential
VCRC	:Vapor Compression Refrigeration Cycle

References

1. Elbel, S. and Lawrence, N., *Review of recent developments in advanced ejector technology*. International Journal of Refrigeration, 2016. **62**: p. 1-18.

2. Ersoy, H. K. and Bilir, N., *Performance characteristics of ejector expander transcritical CO2 refrigeration cycle*. Proceedings of the Institution of Mechanical Engineers, Part A: Journal of Power and Energy, 2012. **226**(5): p. 623-635.

3. Wang, X., Yu, J., Zhou, M. And Lv, X., *Comparative studies of ejector-expansion vapor compression refrigeration cycles for applications in domestic refrigerator-freezers*. Energy, 2014. **70**: p. 635-642.

4. Boumaraf, L., Haberschill, P. and Lallemand, A., *Investigation of a novel ejector expansion refrigeration system using the working fluid R134a and its potential substitute R1234yf*. International Journal of Refrigeration, 2014. **45**: p. 148-159.

5. Liu, X., Yu, J. and Yan, G., *Theoretical investigation on an ejector–expansion refrigeration cycle using zeotropic mixture R290/R600a for applications in domestic refrigerator/freezers*. Applied Thermal Engineering, 2015. **90**: p. 703-710.

6. Xing, M., Yan, G. and Yu, J., *Performance evaluation of an ejector subcooled vapor-compression refrigeration cycle*. Energy Conversion and Management, 2015. **92**: p. 431-436.

7. Zhou, M., Wang, X. and Yu, J., *Theoretical study on a novel dual-nozzle ejector enhanced refrigeration cycle for household refrigerator-freezers*. Energy Conversion and Management, 2013. **73**: p. 278-284.

8. Lawrence, N. and Elbel, S., *Experimental and analytical investigation of automotive ejector air-conditioning cycles using low-pressure refrigerants*. Internatıonal Refrıgeratıon and Air Conditioning Conference. 2012. Purdue: p. 1169.

9. Lawrence, N. and Elbel, S., *Experimental investigation of a two-phase ejector cycle suitable for use with low-pressure refrigerants R134a and R1234yf*. International Journal of Refrigeration, 2014. **38**: p. 310-322.

10. Jeon, Y., Kim, S., Kim, D., Chung, H. J. and Kim, Y., *Performance characteristics of an R600a household refrigeration cycle with a modified two-phase ejector for various ejector geometries and operating conditions*. Applied Energy, 2017. **205**: p. 1059-1067.

11. Jeon, Y., Kim, D., Jung, J., Jang, D. S. and Kim, Y., *Comparative performance evaluation of conventional and condenser outlet split ejector-based domestic refrigerator-freezers using R600a*. Energy, 2018. **161**: p. 1085-1095.

12. Sag, N. B., Ersoy, H. K., Hepbasli, A. and Halkaci, H. S., *Energetic and exergetic comparison of basic and ejector expander refrigeration systems operating under the same external conditions and cooling capacities*. Energy Conversion and Management, 2015. **90**: p. 184-194.

13. Ersoy, H. K. and Bilir, N., *The influence of ejector component efficiencies on performance of ejector expander refrigeration cycle and exergy analysis*. International Journal of Exergy, 2010. **7**(4): p. 425-438.

14. Bilir, N., Ersoy, H. K. and Hepbaşlı, A., *Farklı soğutucu akışkanlar için genleştirici olarak ejektör kullanan kompresörlü soğutucunun performans analizi*, X. Ulusal Tesisat Mühendisliği Kongresi. 2011. İzmir: p. 1317-1325.

15. Baruah, A., Saini, D. K. and Sachdeva, G., *Exergy investigation of a vapor compression system comprising ejector for isentropic expansion*, In Journal of Physics: Conference Series. 2019. IOP Publishing: p. 012125.

16. Gao, Y., He, G., Cai, D. and Fan, M., *Performance evaluation of a modified R290 dual-evaporator refrigeration cycle using two-phase ejector as expansion device*. Energy, 2020. **212**: p. 118614.

17. Yari, M., *Exergetic analysis of the vapour compression refrigeration cycle using ejector as an expander*. International Journal of Exergy, 2008. **5**(3): p. 326-340.

18. Takleh, H. R. and Zare, V., *Performance improvement of ejector expansion refrigeration cycles employing a booster compressor using different refrigerants: Thermodynamic analysis and optimization*. International Journal of Refrigeration, 2019. **101**: p. 56-70.

19. Cui, Z., Qian, S., & Yu, J., *Performance assessment of an ejector enhanced dual temperature refrigeration cycle for domestic refrigerator application*. Applied Thermal Engineering, 2020. **168**: p. 114826.

20. Chen, Q., Hwang, Y., Yan, G., and Yu, J., *Theoretical investigation on the performance of an ejector enhanced refrigeration cycle using hydrocarbon mixture R290/R600a*. Applied Thermal Engineering, 2020. **164**: p. 114456.

21. Bai, T., Yan, G., and Yu, J., *Experimental investigation of an ejector-enhanced auto-cascade refrigeration system*. Applied Thermal Engineering, 2018. *129*: p. 792-801.

22. Jeon, Y., Kim, D., Jung, J., Jang, D. S., and Kim, Y., *Comparative performance evaluation of conventional and condenser outlet split ejector-based domestic refrigerator-freezers using R600a*. Energy, 2018. *161*: p. 1085-1095.

23. Kotas, T. J., *The exergy method of thermal plant analysis*. Elsevier. 2013.

24. Kornhauser, A. A., *The use of an ejector as a refrigerant expander*, International Refrigeration and Air Conditioning Conference. 1990. Purdue: p. 10-19.

25. Sánchez, D., Cabello, R., Llopis, R., Arauzo, I., Catalán-Gil, J. and Torrella, E., *Energy performance evaluation of R1234yf, R1234ze (E), R600a, R290 and R152a as low-GWP R134a alternatives. International Journal of Refrigeration*, 2017. **74**: p. 269-282.

26. Yadav, A. K. and Neeraj., *Performance analysis of refrigerants R1234yf, R1234ze and R134a in ejector-based refrigeration cycle*. International Journal of Air-Conditioning and Refrigeration, 2018. **26**(03): p. 1850026.

Research Article

Application of reverse engineering method on agricultural machinery parts

Ozgur Verim [a],* (ID) *and Ozan Sen* [b] (ID)

ªAfyon Kocatepe University, Faculty of Technology, Department of Mechanical Engineering, Afyonkarahisar and 03200, Turkey
ᵇÇelikform Gestamp Otomotiv A.Ş., Bursa, 16140, Turkey

ARTICLE INFO	ABSTRACT
	Reverse engineering, the production of parts without CAD data, the reproduction of damaged parts, the creation and production of new parts by making innovations on parts with CAD data is a significant area. Considering the field of mechanical engineering, the surface and geometric properties of an existing part can be reconstructed by reverse engineering application. Within the scope of this study, the possibilities offered by reverse engineering are used to create a three-dimensional (3D) model of an agricultural part and the production of its prototype. The agricultural part was scanned in 3D with the help of a scanner, and a mesh model was created. Afterward, the solid model of the part was created, and the prototype was produced with the help of a 3D printer. The deviations of geometric dimensions between the mesh and solid models were analysed, and their convergence levels were determined. At the end of the study, the geometric values between the solid model and the prototype model were compared, and the deviations from the actual value were determined. Thus, it has been shown that both surface modelling studies and solid model designs can be integrated with reverse engineering software.

1. Introduction

Today's production environment is a highly competitive, dynamic and uncertain process. In an environment where competition in the global market is high and customer expectations are constantly changing, a production system must be flexible and reconfigurable [1]. These conditions have led companies to new ways to reduce design times, enable rapid prototyping, and provide commercial benefits [2]. Reverse engineering is used to redesign an existing part, reproduce damaged parts, develop a different product from the existing part, etc. Reverse engineering has a wide range of uses such as machinery, aviation, medicine and archaeology [3,4]. The main purpose of reverse engineering is to create a 3D CAD model suitable for the design of the object. The first stage of reverse engineering is scanning the surface of the part with the help of contact or non-contact scanners. The second stage is the arrangements made to increase the similarity of the model obtained as a result of scanning to the original product. The data obtained at the end of this stage is in the form of points and these data are called point clouds. The third stage is the conversion of the obtained point cloud to the mesh structure and the creation of the CAD model by processing this structure (Figure 1). The

last stage is the creation of the prototype of the product by taking the CAD model as a reference [5,6].

Since the reverse engineering method has a wide field of study, it is frequently used in interdisciplinary studies. Önçağ et al. [2] analyzed literature studies using reverse engineering method for redesign or repair of mechanical parts that are widely used in industry and created a workflow. They used their workflow to create a turbocharger elbow part. They produced the solid model obtained with the reverse engineering approach with the help of 3D printers in 1/1 scale. Kaplan et al. [7] utilized reverse engineering processes in the repair of impeller blades of water turbines in a hydroelectric power plant undergoing maintenance work. By using reverse engineering method, the impeller blades of the water turbine were repaired. Mian et al. [8] combined contact system (with probe) and laser non-contact scanning (without probe) in their work and used contact system for digitization of geometric shapes and non-contact scanning for non-geometric surface forms. They have obtained an advantage for reverse engineering by scanning the part with complex surface form, which is relatively inefficient to scan with the help of the contact system, with the help of the non-contact system.
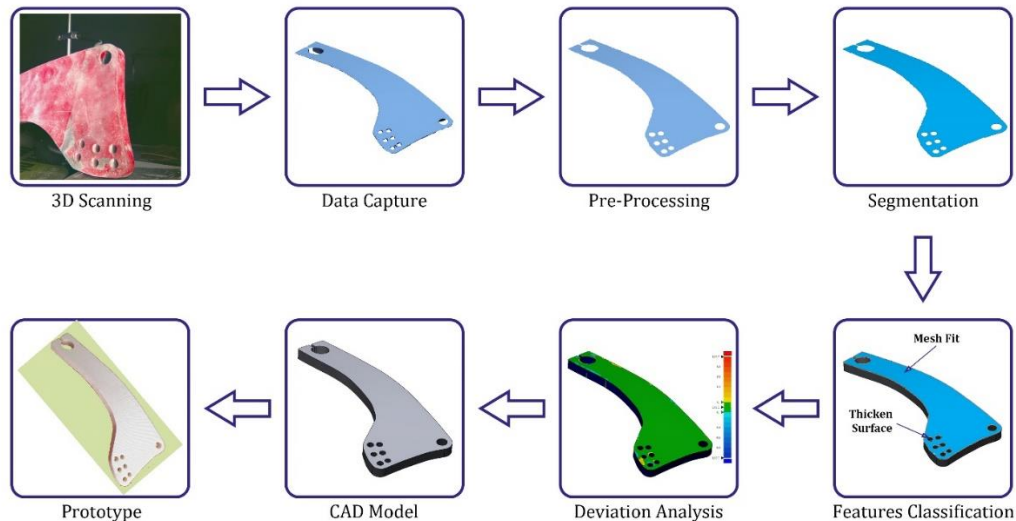
Figure 1. Flowchart of general reverse engineering approach

For the study, although reverse engineering was applied to many fields, we thought there was a shortage of parts in the agricultural field. Because, due to the production processes of the parts in the agricultural field, they usually consist of inhomogeneous geometries. In our study, we tried to apply the reverse engineering method on a non-homogeneous (produced by forging) agricultural piece.

2. Materials and Methods

In order to create a 3D model of a part in a computer environment, it is necessary to take the image of the part down to the smallest detail. Reflections that occur during the scanning of metal parts can prevent reliable data from some parts of the part. As a result, incomplete data formation occurs because sufficient data cannot be obtained from certain parts of the part. In order to eliminate this problem, after the surface of the part was cleaned, the surface of the part was matted. Then, markers were attached to both surfaces of the part to facilitate part image matching (Figure 2). The purpose of the marking process is to ensure that the scanning data overlaps as a result of different scanning operations. As a result of these processes, the agricultural part was fixed on the movable scanner table and made ready for scanning.
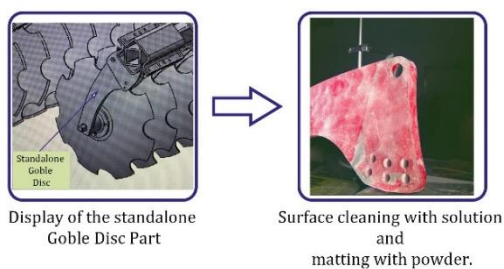
Figure 2. Preparing the agricultural machine part for 3D scanning

2.1 3D Scanning, Data Capture and Pre-Processing

The scanning process of the agricultural part was made with the NextEngine (NextEngine Inc.) device, which scans with a noncontact method. The scanner in question sends laser beams on the part with its 3 detector eyes. While doing this, it detects the surfaces and details on the part according to the angle of reflection of the beams and the angle of incidence of the returning beams. It converts this mathematical data into small triangle particles called "mesh" and transfers it to the computer program. At this point, it is necessary to check whether the details of the part are captured by the scanner. Because during the scanning process, due to parameters such as the quality of the scanner, surface roughness, color, transparency and brightness of the scanned part, situations such as obtaining more or less data than necessary may occur. In cases where more data is obtained, a decrease in the processing speed of the computer can be observed with the increase in file size. On the other hand, in cases where less data is obtained, problems such as not creating the 3D model properly may occur. For all these reasons, it is necessary to plan the scanning process well and to organize the data obtained after the scanning process before proceeding to 3D modeling. Data processing was carried out in the reverse engineering software Geomagic Design X. In this program, the data processing part is carried out with a certain hierarchy (Figure 3).

All scans made on the part surface from different angles were combined in the "Mesh Healing" section in the program, unwanted data on or around the part were cleaned and the noises found were removed. In the "Global Remesh" section, the triangle edge length must be below the current length value for the surface features to be more pronounced.
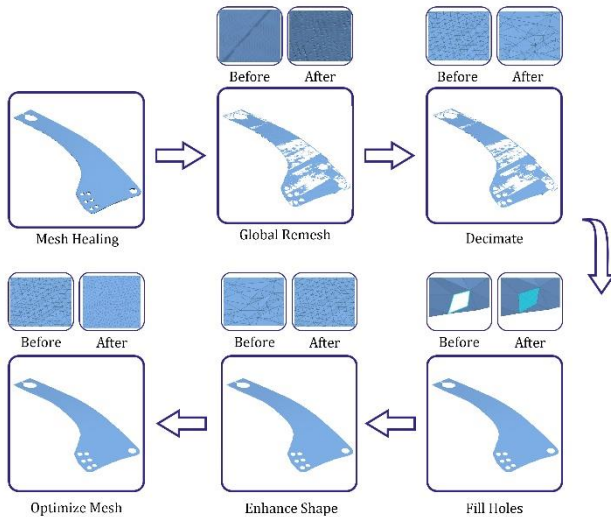
Figure 3. Data processing flowchart in reverse engineering
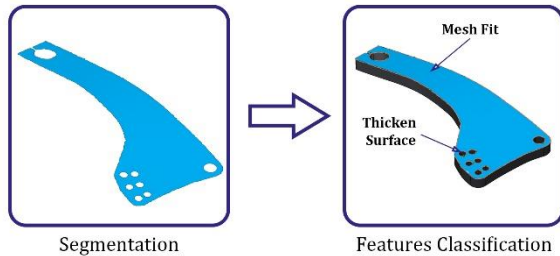
Figure 4. Applying segmentation and feature classification processes to the agricultural part

As a result of these operations, the number of meshes may increase and slow down the processing speed of the computer. Reducing the mesh size in the "Decimate" section speeds up the operations on the model and causes deformities on the model. Therefore, in this study, mesh size reduction was not done manually by us, but it was reduced automatically within the program. Then, with the "Fill Holes" process, the existing gaps on the mesh surface of the model are automatically determined and filled by the program. In the "Enhance Shape" section, the mesh structure is rebuilt and the quality of the mesh structure is improved. In the "Mesh Optimization" section, the mesh structure is optimized and the most suitable mesh structure is created by eliminating the errors (Figure 3).

2.2 Segmentation and Feature Classification

Segmentation can be described as dividing an image into meaningful regions, each of which contains different features, using point cloud and mesh structure data, and plays an important role in reverse engineering [9,10]. The segmentation process regulates the setting of region recognition and parameters that affect the type and size of defined regions [11]. Since the feature classification process was carried out using the segmentation method, segmentation was applied on the agricultural part after the data processing part (Figure 4).

2.3 Modeling

After determining the mesh model properties, firstly, plane and 2D drawings of the part were created. This step needs to be done very carefully and carefully, as the surface formation can differ significantly depending on the strategy chosen during the modeling of the surfaces. Since it is necessary to scan the surfaces in detail in surface modeling, the number of elements is high. The large number of elements causes an increase in surface irregularity and makes it difficult to define surfaces [12]. For the detailed description of irregular surfaces, NURBS (Non-uniform rational B-spline) method was used as surface modeling method and part surfaces were created (Figure 5).

2.4 CAD Model and Rapid Prototyping

The final stage of the reverse engineering process is the creation of the CAD model and the production of the created CAD model (Figure 6). The creation of the CAD model is carried out using heterogeneous methods (parametric or non-parametric), depending on the reverse engineering strategy. Procedures applied at this stage; clamping adjacent surfaces, creating radius and chamfers, and realizing geometric constraints [13]. Rapid prototyping is an integral factor of the reverse engineering process. Rapid prototyping is the process of rapidly producing a physical part with CAD data [14]. Thanks to the production realized in a short time, rapid prototyping has a wide range of uses such as automotive, aviation, medicine, and pharmaceutical industries [5].
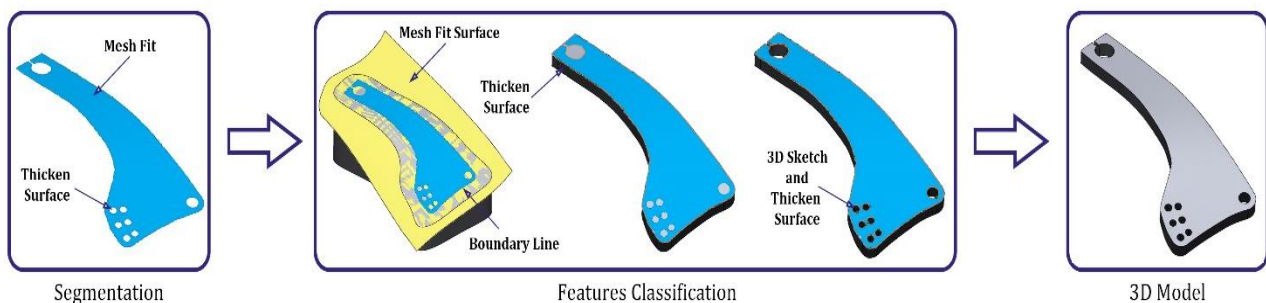
Figure 5. Modeling processes in reverse engineering
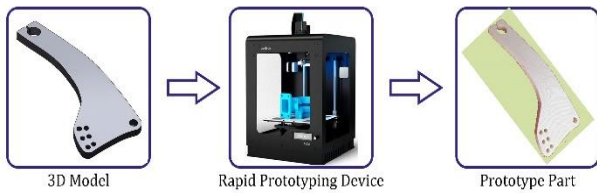
Figure 6. Reverse engineering processes of agricultural part

Rapid prototyping has been an interesting field of study for reverse engineering in recent years. With the rapidly developing technology and the gradual expansion of the application area, many rapid prototype production technologies have been developed. These systems can be listed as Stereolithography Apparatus (SLA), Solid Ground Curing (SGC), Fused Deposition Modeling (FDM), Laminated Object Manufacturing (LOM), Selective Laser Sintering (SLS), Electron Beam Melting (EBM), Shape Deposition Manufacturing (SDM) Direct Metal Laser Sintering (DMLS) and Three-Dimensional Printing (3DP) [5,15–17]. In this study, the prototype of the part was created using the FDM method. The geometric accuracy of the part could be achieved by many additive manufacturing methods. In our study, the availability of the device, the accuracy of the part geometry, the ease of material supply, etc. We chose the FDM method, taking into account the factors. Many studies have been carried out on the advantages of the FDM method and the reasons for its use in the study [18,19]. In FDM process, a plastic material is extruded through a nozzle that follows the cross-sectional geometry of the part. A thin plastic filament is used as the model material [20]. PLA material, which has better mechanical characteristics than ABS material, was used in the study [19]. Properties and process parameters of PLA filament material were determined as nozzle temperature 200 C^0, Table temperature 60 C^0, ambient temperature 23 C^0, material density 1.2 kg/m^3, Tensile strength 62 MPa, infill density 50%, printing speed 45 mm/s [21,22].

3. Results and Discussion

In this study, an agricultural part was scanned with a 3D laser scanner, converted into mesh form, and then a 3D model was created. The prototype of the part was produced with the help of 3D printer from the rapid prototyping tools and 3D created part model. The fact that the part does not have a flat form in the reverse engineering process complicates the scanning process and thus increases the applied processing time. The agricultural part used in the study also caused an increase in the processing time due to its difficult geometry. The dimensional accuracy of the part is extremely important as a backward modeling is done in reverse engineering. The combination of devices, software, and/or operator-induced errors used in the reverse engineering process gives the total error in the resulting model. For this reason, careful examination and analysis should be made for each stage applied. The accuracy analysis between the mesh model and the solid model created by the reverse engineering method was performed and the results are shown in Figure 7.

Looking at the color scale of the deviation analysis results given in Figure 7, it is seen that the green area is the desired region. It is seen that the divergence values of the geometric form of the part increase as one goes from green to red or blue tones. When the part surface is looked at, the abundance of green regions means that the model accuracy is high. A number of different color tones can be seen around the small and large hole circles of the part. Since the part has a non-uniform structure as a whole, modeling was also difficult. The difference in deviation values in the hole circles is due to the difficulty of modeling. The deviation analysis provides a detailed comparison of the mesh and the part. Since only the visible surface of the real part (Figure 1) was scanned, the deviation analysis was also created for this surface only.

The differences between the dimensions of the 3D model created by the reverse engineering method and the dimensions of the part created by rapid prototyping were revealed by morphometric comparison (Table 1). Some dimensions are important for the identification of the part and these dimensions are given in Table 1. The deviation values between the solid model and the prototype model are shown as distance (mm) and percent (%). According to the values in Table 1, the average deviation distance was 0.5 mm and the average deviation percentage was 97.63.

The close relationship between 3D digitization and rapid prototyping makes it easy for us to model 2D and 3D parts with difficult and complex geometries. By combining these two techniques, the creation of 3D solid models necessary for the modification or reconstruction of parts forms the basis of reverse engineering [23]. In this context, increasing the prevalence of studies in the field of reverse engineering provides more accurate results in the field of design and production. This issue is at the forefront of the results of our study. When we examine Table 1, it is seen that the deviation percentage values are above 95. This value is the result of how closely we produce this part with accuracy. In addition, the accuracy analysis results in Figure 7 show how accurate the transition to 3D solid model geometry is in the mesh structure.
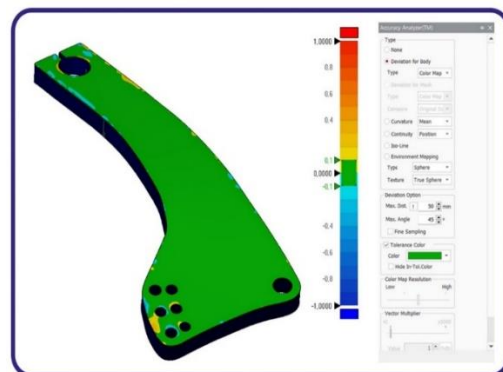
Figure 7. Deviation analysis results between mesh and solid model

Table 1. Morphometric comparison of Agricultural Machinery part
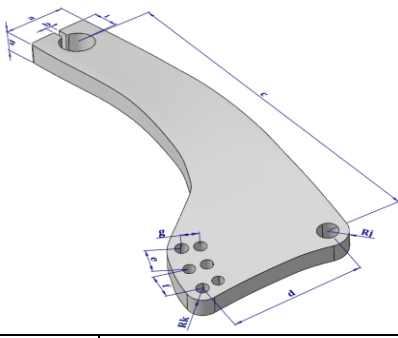
Parameters	Dimension on 3D Model (mm)	Dimension on Prototype Model (mm)	Deviation (mm)	Deviation (%)
a	67.39	66.72	0.67	99
b	5.99	6.3	0.31	95
c	381.51	380.8	0.71	99
d	140.37	139.6	0.77	99
e	29.33	28.97	0.36	98
f	29.33	28.97	0.36	98
g	18.08	18.27	0.19	98
h	20.46	21.07	0.61	97
i	29.18	29.27	0.09	99
Rj	20.99	21.6	0.61	97
Rk	17.99	17.1	0.89	95
		Average:	0.5	97.63

The 3D model developed with the CAD program was produced with 3D Printing technology. FDM method was used in production and PLA was chosen as the material. The accuracy of the part geometry produced in 3D Printing technology depends on many factors. In our study, we used the parameter values that are frequently selected during the printing process.

4. Conclusions

In our study, we examined the processes of creating a 3D solid model and prototype of a non-uniform agricultural machine part by reverse engineering method and comparing them with each other. In the reverse engineering method, 3D scanning and solid modeling methods [24–27] and rapid prototyping methods [28,29] were examined and procedures were carried out using the systems available in our institution. In the study carried out, the active and passive aspects of the processes were evaluated and certain gains were made. These gains constitute a preliminary experience for future studies.

Declaration

The authors declared no potential conflicts of interest with respect to the research, authorship, and/or publication of this article. The authors also declared that this article is original, was prepared in accordance with international publication and research ethics, and ethical committee permission or any special permission is not required

Author Contributions

O. Verim and O. Sen. Authors developed the methodology. O. Verim performed the analysis, supervised and improved the study. O. Verim and O. Sen wrote the manuscript together. O. Verim proofread the manuscript.

References

1. Bi, Z. M., and L. Wang, *Advances in 3D data acquisition and processing for industrial applications*. Robotics and Computer-Integrated Manufacturing, 2010. **26**(5): p. 403-413.

2. Önçağ A. Ç, Ç. Tekcan and H. Özden, *Assessment and application of modeling mechanic parts with reverse engineering*. Pamukkale University Journal of Engineering Sciences, 2018. **24**(1): p. 42-49.

3. Buonamici F, M. Carfagni, R. Furferi, L. Governi, A. Lapini, and Y. Volpe, *Reverse engineering of mechanical parts: A template-based approach*. Journal of Computational Design and Engineering, 2018. **5**(2): p. 145-159.

4. Dongaonkar A. V., and R. M. Metkar, *Reconstruction of damaged parts by integration reverse engineering (RE) and rapid prototyping (RP)*. 3D Printing and Additive Manufacturing Technologies, 2019. p. 159-171.

5. Çelik, İ., F. Karakoç, M. C. Çakır,and A. Duysak, *Hızlı prototipleme teknolojileri ve uygulama alanları*. Journal of Science and Technology of Dumlupınar University, 2013. (031): p. 53-70.

6. Haleem A, M. Javaid, A. Goyal, and T. Khanam, *Redesign of Car Body by Reverse Engineering Technique using Steinbichler 3D Scanner and Projet 3D Printer*. Journal of Industrial Integration and Management, 2022. **7**(02): p. 171-182.

7. Çelebioğlu K, and A. Kaplan, *Development and Implementation of a Methodology for Reverse Engineering Design of Francis Turbine Runners*. Pamukkale University Journal of Engineering Sciences, 2019.**25**(4): p. 430-439.

8. Mian, S. H., M. A. Mannan, and A. M. Al-Ahmari, *Multi-sensor integrated system for reverse engineering*. Procedia Engineering, 2013. **64**: p. 518-527.

9. Mejia, D., O. Ruiz-Salguero, J. R. Sánchez, J. Posada, A. Moreno, and C. A. Cadavid, *Hybrid geometry/topology-based mesh segmentation for reverse engineering*. Computers & Graphics, 2018. **73**: p. 47-58.

10. Verim, Ö., and M. Yumurtacı, *Application of reverse engineering approach on a damaged mechanical part*. International Advanced Researches and Engineering Journal, 2020. **4**(1): p. 21-28.

11. Buonamici, F., M. Carfagni, R. Furferi, L. Governi, A. Lapini, and Y. Volpe, *Reverse engineering modeling methods and tools: a survey*. Computer-Aided Design and Applications, 2018. **15**(3): p. 443-464.

12. Günpınar, E., *Tersine mühendislik yoluyla üç boyutlu geometrik modelin oluşturulması ve gemi yapim endüstrisindeki bazi uygulamalari*. Dokuz Eylül Üniversitesi Mühendislik Fakültesi Fen ve Mühendislik Dergisi, 2016. **18**(54): p. 624-639.

13. Benkő, P., R. R. Martin, and T. Várady, *Algorithms for reverse engineering boundary representation models*. Computer-Aided Design, 2001. **33**(11): p. 839-851.

14. Şahin, İ., T. Şahin, and H. Gökçe, *Hasarlı dişlilerin tersine mühendislik yaklaşımıyla yeniden oluşturulması*. Düzce Üniversitesi Bilim ve Teknoloji Dergisi, 2017. **5**(2): p. 485-495.

15. Dudek P, and A. Rapacz-Kmita, *Rapid prototyping: Technologies, materials and advances*. Archives of Metallurgy and Materials, 2016. **61**: p. 891–895.

16. Campbell, I., D. Bourell, and I. Gibson, *Additive manufacturing: rapid prototyping comes of age*. Rapid Prototyping Journal, 2012. **18**(4): p. 255-258.

17. Gibson, I., D. Rosen, and B. Stucker, *Additive Manufacturing Technologies: Rapid Prototyping to Direct Digital Manufacturing*, 2014, 498 Springer, New York, 2.

18. Bellini, A., and S. Güçeri, *Mechanical characterization of parts fabricated using fused deposition modeling*. Rapid Prototyping Journal, 2003. **9**(4): p. 252-264.

19. Vukasovic, T., J. F. Vivanco, D. Celentano, and C. García-Herrera, *Characterization of the mechanical response of thermoplastic parts fabricated with 3D printing*. The International Journal of Advanced Manufacturing Technology, 2019. **104**: p. 4207-4218.

20. Chua, C. K., K. F. Leong, and C. S. Lim, *Rapid prototyping: Principles and applications, third edition*. 2010, World Scientific Publishing Company.

21. Günay, M., S. Gündüz, H. Yılmaz, N. Yaşar, and R. Kaçar, *PLA esaslı numunelerde çekme dayanımı için 3D baskı işlem parametrelerinin optimizasyonu*. Politeknik Dergisi, 2020., **23**(1): p. 73-79.

22. Maguluri N, G. Suresh, and K. V. Rao, *Assessing the effect of FDM processing parameters on mechanical properties of PLA parts using Taguchi method*. Journal of Thermoplastic Composite Materials, 2021.

23. Dúbravčík, M., and Š. Kender, *Application of reverse engineering techniques in mechanics system services*. Procedia Engineering, 2012. **48**: p. 96-104.

24. Prakash, K. S., T. Nancharaih, and V. S. Rao, *Additive manufacturing techniques in manufacturing-an overview*. Materials Today: Proceedings, 2018. **5**(2): p. 3873-3882.

25. Wu, H., W. P. Fahy, S. Kim, H. Kim, N. Zhao, L. Pilato, and J. Koo, *Recent developments in polymers/polymer nanocomposites for additive manufacturing*. Progress in Materials Science, 2020. **111**: p. 100638.

26. Yakout, M., M. A. Elbestawi, and S. C. Veldhuis, *A review of metal additive manufacturing technologies*. Solid State Phenomena, 2018. **278**: p. 10-14.

27. Urhal, P., A. Weightman, C. Diver, and P. Bartolo, *Robot assisted additive manufacturing: A review*. Robotics and Computer-Integrated Manufacturing, 2019. **59**: p. 335-345.

28. Bartol, K., D. Bojanić, T. Petković, and T. Pribanić, *A review of body measurement using 3D scanning*. IEEE Access, 2021. **9**: p. 67281-67301.

29. Javaid, M., A. Haleem, R. P. Singh, and R. Suman, *Industrial perspectives of 3D scanning: features, roles and it's analytical applications*. Sensors International, 2021. **2**: p. 100114.

Research Article

Green biosynthesis, characterization of silver nanoparticles using a green alga *Spirogyra* sp. and their antioxidant and enzyme activities

Aysel Basoglu [a,*] iD and Zeynep Akar [b] iD

aDepartment of Occupational Health and Safety, Faculty of Health Sciences, Gümüşhane University, 29100 Gümüşhane, Turkey
bDepartment of Genetics and Bioengineering, Faculty of Engineering, Gümüşhane University, 29100 Gümüşhane, Turkey

ABSTRACT

A simple, environmentally friendly, inexpensive, and one-step alternative method was reported for the green biosynthesis of silver nanoparticles (AgNPs) operating the *Spirogyra* sp. extract as a reducing and stabilizing substance. Concentration of $AgNO_3$ and reaction time were optimized to prepare AgNPs under controlled conditions. The synthesized silver nanoparticles were characterized by UV-Vis absorption spectroscopy, fourier transform infrared spectroscopy (FT-IR), transmission electron microscopy (TEM), energy dispersive X-ray analysis (EDX), and elemental mapping. The TEM analysis showed that the average particle size of AgNPs was 18.3 nm. Structural details of silver nanoparticles elucidated by Selected Area Electron Diffraction (SAED) based on TEM images. In addition, biological activity tests were applied to nanoparticles and algal extracts to determine antioxidant activity (3 different tests: DPPH (1,1-diphenyl-2-picrylhydrazil) radical scavenging activity, total phenolic content (TPC) and total flavonoid content (TFC)) and α-glucosidase enzyme inhibition. Antioxidant activity and α-glucosidase enzyme inhibition values of silver nanoparticles are higher than the values of *Spirogyra* sp. extracts.

1. Introduction

High-tech materials advanced on the nano-scale, that have many benefits as compared with the research performed on the macro-scale, are actively used in many fields such as medicine, biotechnology, environment, energy, defense industry, textile, electronics and space research. Nanotechnology is typically well-known as a crucial branch of science that objectives natural and synthetic practical materials, that have a size distribution on the scale of nanometers (10^{-9} m) and feature attracted the eye of many scientists in the modern century. Nanotechnology involves understanding the basic physics, chemistry, biology, and technology of nanometer-scale materials. In recent decades, advances in nanotechnology have accelerated, with numerous engineered nanoparticles (NPs) having outstanding optical, magnetic, catalytic, and electrical properties being produced. Thanks to the development and diversification of nanoparticles, which are at the core of the field of nanotechnology, final products with pre-designed functional properties can be obtained. Nanostructures are the subject of all

nanotechnological applications everywhere in nature and the dimension of nanoparticles determines their characteristic properties [1]. In the context of nanosciences and nanotechnologies, it is widely accepted to focus on units of size [2]. Nano-sized particles have a larger surface area/volume ratio and surface molecule fraction, making them unique materials because of superior physicochemical properties like optical property [3], magnetic property [4], catalytic property [5], and antimicrobial property [6] at the nano-size compared to the bulk materials with the same chemical composition [7, 8]. Among the nanoparticles, silver nanoparticles (AgNPs) are widely used in scientific research due to unique predictable properties. About 5000 years ago, people of many races such as Greeks and Egyptians used silver to keep meals products safe [9]. In many dynasties in ancient times, the use of silver ware and utensils for various purposes such as eating, drinking, and storage various foods were quite common all over the world, in all probability because of the information of antimicrobial action [10]. It is mentioned in the Indian Ayurvedic medicine book known as "Charak Samhita" in the medical

literature that some metals such as silver have therapeutic potentials. As before, silver utensil is still used for the preparation of "panchamrit" in the worship of Hindu religion [11]. Also, silver was widely used as an antimicrobial agent until the determination of antibacterial effect of penicillin by Alexander Fleming 70 years ago.

Silver nanoparticles (AgNPs) commonly used in scientific research, are also preferred in different application areas of biomedical material [12], drug delivery [13], water treatment [14], agriculture (food storage-containers) [15], textile [16], energy [17], cosmetic [18] because of their particular properties such as good electrical conductivity, antifungal, antimicrobial, antiviral, antibacterial, anti-inflammatory, anticancer, photoelectrochemical, antibiofilm, and enzyme activity.

AgNPs are synthesized by numerous strategies, together with chemical reduction, impregnation, laser ablation, ultrasonic radiation, and explosion. Since the potent reducing and capping agents often utilized by the chemical methods are deadly to humans, and the environment, there is a desire to synthesize AgNPs in additional economical and eco-friendly manners. Some chemicals known to be toxic, such as sodium borohydride [19], citrate [20] or ascorbate [20], are widely used as reducing agents. In this classical preparation methods, the usage of several synthetic reactants as precursors, diverse of chemicals as reducing agent, large quantities of surfactants as stabilizing agents and, carcinogenic solvents firstly changed into dangerous to the living life, and then the future of the world. As a sub-branch of nanotechnology, the nanobiotechnology approach based on nanoparticle synthesis using herbal extracts, which has made significant progress in recent years, arouses interest as a popular research area. In this context, the procedures used have a green synthesis perspective, thus providing energy savings by bringing a very effective and environmentally friendly approach compared to classical methods, as well as being more cost-effective compared to conventional materials, offers a very interesting and innovative alternative to researchers working in this field. The production of silver nanoparticles by the green synthesis method has also paved the way for their use in biological systems.

The principle of green chemistry was first mentioned in the book "Green Chemistry" written by Anastas and Warner in 2000 [21]. The book "Green Chemistry" contains 12 principles that should be applied to limit the release of hazardous chemicals into the environment and human exposure to them. The headlines that stand out in principles of green chemistry are: -preventing the production of waste,- limiting energy usage - need materials in synthesis strategies have nominal or no toxicity to the surroundings or individual,- Organic solvents and auxiliary chemicals should not be used, - Using Renewable Raw Materials,   - Performing Real-Time Analysis for Pollution Prevention. Moreover, the 12 of principles were explained in detail by Gałuszka et al. in 2012 [22]. The main issue emphasized by both working groups is the use of agricultural products as reducing and limiting agents. Biosynthesis of AgNPs consist of bacteria like Escherichia Coli (E. coli) [23], yeast like Saccharomyces cerevisiae [24], fungi like Coriolus versicolor [25] and Penicillium brevicompactum [26], Algal Species like Caulerpa racemose [27], Gracilaria corticata [28] and Laminaria japonica [29] and plant/plant extracts like tea [30], Artemisia quttensis [31], Gardenia Jasminoides Ellis [32] and P. granatum L. [33].

Plants show biological activities because of their rich phenolic compounds content. Therefore, besides their use as food, plants are also widely used for medicinal purposes [34]. One of the applications used to more effective biological activity values of plant compounds is to form metal nanoparticles from plant compounds [35]. Biological activity determination studies on macroscopic terrestrial plants are more than other groups of organisms. However, algae, which contribute to the primary production of aquatic ecosystems, have an important place among organism groups in terms of biological activity [36].

Silver nanoparticles are usually formed in the presence of $AgNO_3$ salt solution. Ag^+ ions originating from the silver nitrate salt are first reduced to Ag atoms by reducing agents. Then, the reduced Ag atoms create several nucleates. Finally, the nucleates carried out in tiny clusters grow the particles. The size and shape of the nanoparticles can be controlled with the presence of atoms based on the concentration ratio of silver salt to reducing agent. The present study regarding the synthesis and characterization of AgNPs using the aqueous alga *Spirogyra* sp. and, their antioxidant and enzyme activities. This study purpose to form a new biological source for the synthesis of silver nanoparticles besides evaluating their antioxidant and enzyme activities of silver nanoparticles by comparing with that of the algal extract. There are limited studies in which algae are used as a source for silver nanoparticle production. [27-29, 37]. It should be especially noted that silver nanoparticles have been synthesized the usage of the *Spirogyra varians* in a study by Salari et al., and the antibacterial properties of was studied through measuring the inhibition zone, MIC and MBC [38]. In our study, the algal extracts could be available as reducing and stabilizing substance to make stable AgNPs operating a green chemistry road as a different method over other toxic chemical reducing substance.

2. Materials and Methods

2.1. Materials

All chemical compounds are of analytical grade and do not need any purification before using in the study. The

standart solution of silver nitrate (AgNO$_3$, 1000 mg/L)) was bought from Merck. The silver nitrate solutions (1mM, 2 mM and 3 mM) were prepared in deionized water. The deionized water was achieved by using the Sartorius Milli-Q system (arium 611UV; Sartorius AG, Göttingen, Germany). Also the filter paper is Whatman No. 1. The chemical for bioactivity tests were purchased from Sigma Aldrich (chemicals of DPPH, gallic acid and α-Glucosidase enzyme), Merck (chemicals of folin-ciocalteu and quercetin) and Biosynth Carbosynth (4-nitrophenyl-α-D-glucopyranoside).

The algal sample (*Spirogyra* sp.) was collected from a spring in Torul district of Gümüşhane province. The collected algal biomass were washed with deionized water a couple of times to clear from the dust and particles. Next procedure is an drying under the sun to remove the ultimate moisture from the algae *Spirogyra* sp.. The well-dried algae were easily pulverized by hand crumbling.

2.2. Preparation of Spirogyra sp. extract

The *Spirogyra sp.* extract was carried out according to the similar methods described earlier with modifications [29, 32]. The algal extract was obtained by placing 7.5 g of fine powders together with 100 mL of deionized water: For the preparation of the algal extract, at first, this *Spirogyra* sp. aqueous solution was heated until boiling. After boiling, it was incubated at 60ºC in water bath for 30 minutes. The mixture changed its color from watery to darkish brown. The algal extract was given time to cool down to room temperature, filtered using filter paper. Also, to take away the suspended particles, this extract was centrifuged at 10000 rpm for 10 minutes. The filtrate volume was finally maintained to 50 mL with deionized water. The stock filtrate of the Spirogyra sp. was stored further as a reducing substance for the biosynthesis of AgNPs in refrigerator at 4 ∘C.

2.3. Biosynthesis of silver nanoparticles (AgNPs)

The *Spirogyra* sp. extract was biologically served as reducing substance in the synthesis of silver nanoparticles. For the reduction of Ag$^+$ ions, the algal extract was added to aqueous solution of AgNO$_3$ (45 mL) and heated at 60 ºC under magnetic stirring at 500 rpm/min for 2 h (C-MAG HS7 digital magnetic stirrer, IKA Co., Staufen, Germany) [29]. The incubation of the reacting solution in a dark place protects against the excitation of nanoparticals' atoms by light energy at room temperature.

In many studies, the effect of different AgNO$_3$ concentrations on the biosynthesis of AgNPs has been studied [18, 23, 33].AgNPs were also synthesized with various concentration of AgNO$_3$ (1mM, 2 mM and 3 mM) by ensuring the concentration of the extract the same (5 mL, 7.5% w\v). For all AgNO$_3$ concentrations, the color of the reaction mixtures was changed shortly after the addition of the algae extract, demonstrating the presence of specified reduction reaction. As the reduction reaction continues, the initial slightly yellowish color of the solution mixture turned to gray, brown and finally reddish color. The strong absorbance created by the excitation of the nanoparticle surface plasmons causes the change in color which was the strongest evidence for the formation of the silver nanoparticle [39, 40]. The reduction reactions in the formation of silver nanoparticles were observed with the changes in their color of the reaction mixtures including different AgNO$_3$ concentrations and also were spectrophotometrically monitored as a function of time of reaction (1 h, 3 h, 24 h, 48 h and 72 h) on a spectrophotometer [29,32].

For the purification of AgNPs, the reaction mixture of AgNPs were centrifuged at 10000 rpm for 15 min: The aqueous silver nanoparticle solution was centrifuged and then the supernatant solution was decanted. The resulting pellet was redispersed in deionized water and centrifuged again. The process of centrifugation and redispersion was iterated three times for the supporting separation of AgNPs from the freely available proteins/enzymes.

2.4. Characterization of silver nanoparticles

UV–vis spectral analyzes were done by Shimadzu UV-vis spectrophotometer (UV-1800 UV, Japan). 4 mL of the aqueous solutions of AgNPs were pipetted into a 1 cm quartz cell and subsequently analysed using UV-Vis absorption spectrophotometer with a resolution of 1.0 nm between 200 and 800 nm at room temperature.

The surface functional groups of AgNPs were investigated by Fourier transform infrared spectroscopy. The spectral analyzes were done with Perkin-Elmer Spectrum Two FTIR spectrometer in a spectral range of 400–4000 cm^{-1} at room temperature. AgNPs was purified before FT-IR spectra of was recorded: 20 mL of bioreduced AgNPs solution using 1mM AgNO$_3$ after 24 h of reaction was centrifuged at 10000 rpm for 15 min. Subsequent to the centrifugation, a novel solution mixture was prepaired by dispersing the pellet in 20 mL of deionized water to remove any proteins/enzyme molecules that are freely found in the solution of the silver nanoparticles. Three replicates were performed in both the centrifugation and the dispersion. Furthermore, FTIR spectra of the *Spirogyra* sp. extract was recorded. The aqueous *Spirogyra* sp. solution was removed from water by rotary evaporation before FT-IR spectra of was recorded.

Transmission electron micrographs were performed at 200 kV by using a Talos F200S microscope (FEI, USA) in the Research Laboratory of Bayburt University. 1.5 mL of AgNPs solution after 24 h of reaction was removed from water by heating at 60ºC. Then, AgNPs was dried with N$_2$ gas and redispersed with alcohol treating by an ultrasonic probe for about 10 s. Two drops of the AgNPs solution was

poured on a carbon-coated copper grid. The grid was kept at room temperature until the solvent disappeared before the morphological images of AgNPs were acquired.

2.5. Antioxidant activity of extract and silver nanoparticles of Spirogyra sp.

2.5.1. DPPH radical scavenging activity

The DPPH antioxidant activities of extract and silver nanoparticle of the algae were measured in three parallel based on method of Brand-Williams [41], it was also determined sample reagent blanks. In the study, 750 µL of 100 µM methanolic DPPH radical solution was added onto 750 µL sample solutions. The mixture was vortexed and incubated at room temperature for 60 minutes. At the end of the period, it was determined at 517 nm absorbance with spectrophotometer.

The change of absorbance of DPPH radical in different sample concentration was measured. The graph was plotted based on absorbance corresponding to the concentrations. The results were expressed as the IC_{50} value. Lower IC_{50} values indicate higher radical scavenging potential.

2.5.2. Total phenolic content (TPC)

Total phenolic contents of the extract and the silver nanoparticle were determined according to the method of Slinkard and Singleton [42] using Folin-Ciocalteu reagent. Firstly, 50 µL of the sample (the solution of extract and synthesized silver nanoparticle) was diluted with 2.5 mL of distilled water. Then 250 µL of 0.2 N Folin-Ciocalteu reagent and 750 µL of Na_2CO_3 (7.5%) was on the mixture, respectively. It was vortexed. After the tubes were kept at room temperature for 2 h, absorbance values were determined at 765 nm.

The antioxidant standard of gallic acid (500-250-125-62.5-31.25 µg/mL) was used to draw the standard calibration graphic. The amounts of phenolic compounds in the samples were calculated in gallic acid equivalents (GAE µg/mL).

2.5.3. Total flavonoid content (TFC)

Method developed by Fukumoto and Mazza [43] was applied to determine the flavonoid contents of extracts and the nanoparticle. As in the other tests, the sample measurments were carried out in three parallels. In addition, measurements were also made for sample and reagent blanks. First of all, 250 µL equal amounts of samples were pipetted into the tubes. Then 2.1 mL of methanol was added to all tubes. Finally, 50 µL of 1M ammonium acetate (CH_3COONH_4) and 10% aluminum nitrate ($Al(NO_3)_3 \cdot 9H_2O$) were transferred to the tubes, respectively, except the sample blank and vortexed. At the end of the 40 minutes incubation period, absorbance values were read at 415 nm.

Quercetin was used as the antioxidant standard. Quercetin (0.25 mg/mL). It was prepared at six different concentrations and absorbance values-concentration graphs were drawn. According to the graphic, the total amount of flavonoid substance in the samples was determined as quercetin equivalent (QAE µg/mL).

2.6. % α-Glucosidase enzyme inhibition

The α-glucosidase inhibitory activities of extract and silver nanoparticle of the *Spirogyra* sp. were determined with modified method which developed by Zhipeng Yu et al. [44]. Firstly, 650 µL of phosphate buffer (pH: 6.8 and 0.1 M) was transferred onto 20 µL sample in test tubes. Then, 30 µL of α-glucosidase enzyme (Saccharomyces cerevisiae, lyophilized powder, ≥ 10 units/mg protein) prepared in phosphate buffer was added to mixture. After that it was incubated at 37 °C for 10 minutes, 75 µL of substrate (4-Nitrophenyl-α-D-glucopyranoside) was added. This time, the mixture was kept at 37 °C for 20 minutes, then 650 µL of 1M Na_2CO_3 was added and the reaction was stopped. As in α-glucosidase, the control solution was also prepared. Absorbance values of the mixture were measured at 405 nm in a UV-vis spectrophotometer. The % inhibition values of the samples were calculated according to the following Equation (1)

$$\% \; inhibition \; = \; \left[\left(\frac{A_{control} - A_{sample}}{A_{control}} \right) \right] \times 100 \qquad (1)$$

$A_{control}$: The absorbance value of the control solution
A_{sample}: Absorbance value of the sample extract

3. Results and Discussion

3.1. Synthesis and characterization of the AgNPs

A one-step green chemistry-based approach involving the algal (*Spirogyra* sp.) biosynthesis method was performed to synthesis silver nanoparticles (Figure 1). When the algal extract was placed in Ag^+ solution, the colorless mixture became reddish color as Ag^+ was reduced to silver metal (Ag^0) through the algal extract.

In this study, the prepared AgNPs was characterized by UV-Vis spectroscopy, FT-IR spectroscopy, and transmission electron microscopy (TEM).

After adding the algal extract to the Ag^+ solution, the formation of AgNPs was visually noticed by the color change of the reaction mixtures. At the end of the reaction, the transparent color of the silver nitrate solution changed to reddish color forming a colloidal dispersion, verifying the growth of silver particles. The formation of colloidal AgNPs was also confirmed by UV−vis spectroscopy: Figure 2 consists of the UV-Vis absorption spectra for both the algal extract solution and AgNPs solution.
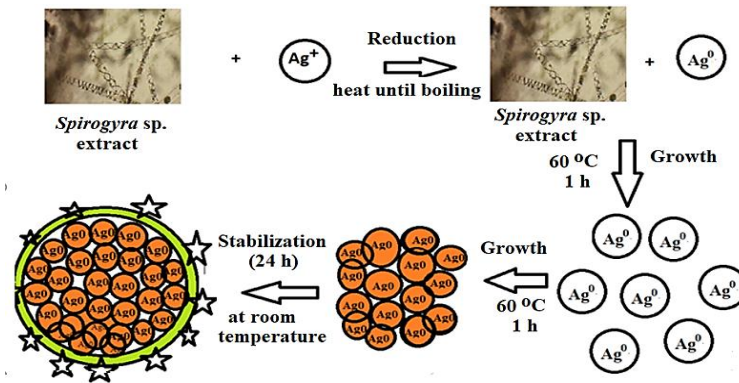
Figure 1. Schematic representation for the green biosynthesis of AgNPs from *Spirogyra* sp.

The spectra of the algal extract solution indicated the absence of an SPR peak. The location of SPR peaks are particularly attached to the size and shape of the nanoparticles, surface charge and, environmental medium conditions. The free electrons belonging to groups such as -OH and -COOH as well as -NH$_2$ on the surface of silver nanoparticles interact with the incident light in UV-Vis spectrophotometry is the most important factor for the decision of the SPR particularities of AgNPs. SPR emerged when the wavelength of incident light combined with the vibration frequency of free electrons, and intense absorption peaks were exhibited in UV-Vis spectra. Surface plasmon resonance, SPR, to be briefly expressed, is a physical phenomenon that develops due to the vibrational movements that occur on the metal surface when plane polarized light hits a metal surface and is reflected. As seen in Figure 2, AgNPs has a SPR absorption peak at about 488 nm which has been documented for various silver nanoparticles [1, 45, 46]. It is well known that Ag nanospheres have only one SPR peak. In the study, the synthesized-AgNPs consist of spherical- and oval-shaped. In addition to the surface plasmon resonance, the other peak at 378 nm may attributed to the presence of contaminating proteins in the AgNPs solution. In the typical algal (*Spirogyra* sp.) synthesis,three different concentrations of aqueous AgNO$_3$ solutions (1 mM, 2 mM and 3 mM) were used to prepare AgNPs keeping the algal extract concentration constant (5 mL, 7.5% w\v). The reduction of the Ag$^+$ at different concentrations by the constant amounts of aqueous the algal extract were also monitored as a function of time of reaction by UV–Vis spectroscopy measurements and the spectra obtained are shown in Figure 3.

So, the changes of SPR absorption peak with the concentration of AgNO$_3$ were examined as a function of time from Figure 3. In Figure 3a, it was observed that for 1mM of AgNO$_3$ a broad peak recorded at about 480 nm appeared as a shoulder in the UV-Vis spectra after 24 h of reaction and increased in intensity and shifted from 480 nm to 488 nm until 72 h of reaction.
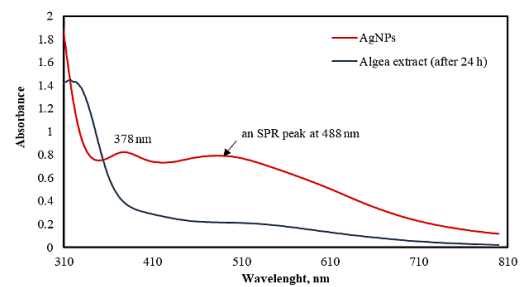
Figure 2. UV−vis spectra of the water-diluted *Spirogyra* sp. extract solution and the synthesized AgNPs solution using 1mM AgNO$_3$ at the end of 24 h of reaction
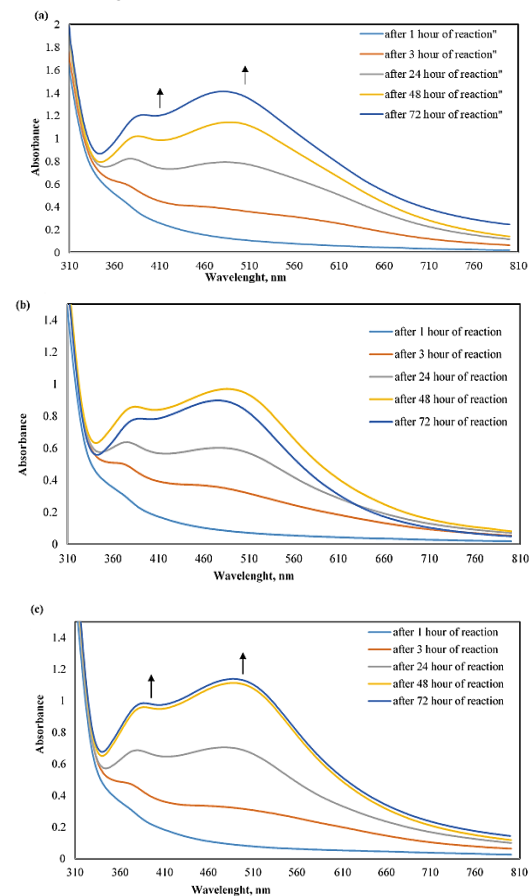
Figure 3. The reduction of the Ag$^+$ at different concentrations by the constant amounts of aqueous Spirogyra sp. extract were also monitored as a function of time of reaction by UV–vis spectroscopy measurements. The spectra obtained as a function of time in the presence of 1mM (a) 2 mM (b) and 3 mM (c) of AgNO$_3$.

In addition to the SPR absorption peak corresponding to the excitation of longitudinal plasmon vibrations, another peak at about 370 nm was also seen due to probably contaminating proteins in the presence of 1mM of $AgNO_3$ that increased in intensity with 8 nm of shift until 72 h of reaction. Similar changes in the absorbance band, such as increase in intensity and band-shifted, were also observed in the presence of 2 mM and 3 mM of $AgNO_3$ (Figure 3b,c).

In order to observe which concentration (1 mM, 2 mM and 3 mM of $AgNO_3$) would be more appropriate for the reduction of Ag^+ ion, the absorbance values of synthesized AgNPs solutions at about 488 nm were plotted against the time of reaction (in Figure 4). From the graph, it could be clearly seen that the greatest increase in absorbance of the SPR peak were obtained with $AgNO_3$ at 1 mM concentration. Choosing the lowest concentration of $AgNO_3$ will also be much more useful in terms of less silver accumulation in the environment.

Furthermore, the color change of AgNPs solution to reddish color visually noticed was completed at the end of 24 h (in Figure 5a) which was determined as ideal reaction time. At the end of 24 h of reaction time, the UV-Vis spectra showing the effect of different concantration of $AgNO_3$ concentration on the AgNPs, could be seen from Figure 5b.

The size, shape, morphology and distribution of AgNPs was determined by using the High Resolution Transmission Electron Microscopy (HRTEM) technique. TEM images of AgNPs reveals that, the nanoparticles have two different shapes as spherical or oval shaped (Figure 6). Also, the dispersed silver nanoparticles consist of spherical- and oval-shaped in variable size. The size is substantially ranged between 8.9 and 23.0 nm as shown in Figure 6a. The histogram in Figure 6a inset reveals the particle size of AgNPs. The average particle size determined from 123 dark shaded areas considered to be particles in the image in Figure 6a is 18.3 nm.

Figure 4. Time dependent-absorption for the reduction of the Spirogyra sp. extract with different values (1.0 mM, 2.0 mM and 3 mM) of $AgNO_3$ concentrations at the SPR peak of 488 nm
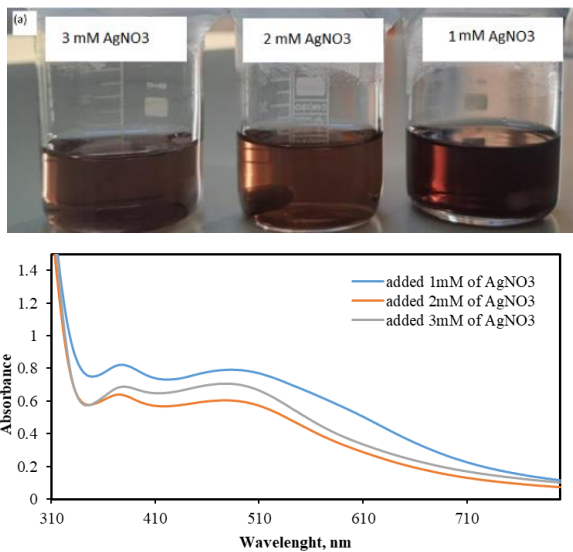
Figure 5. a) Visual appearance of the beaker containing the *Spirogyra* sp. extract and $AgNO_3$ added the *Spirogyra* sp. extract solution (1mM, 2mM and 3mM). b) UV-Vis spectra showing the effect of different conc. of $AgNO_3$ concentration on the AgNPs. The reaction time was 24 h

Figure 6. TEM image of spherically- and oval- shaped AgNPs at 500 nm (a) and 20 nm (b). Inset in (a) is the histogram related to the diameter of AgNPs in (a)
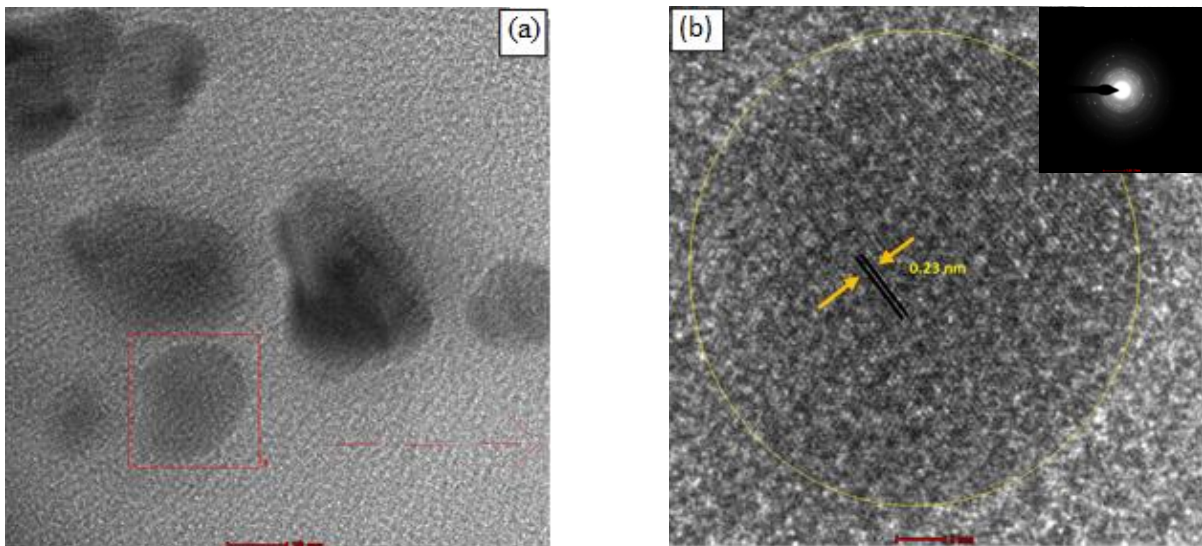
Figure 7. HRTEM images of AgNPs at 10 nm (a) and of spherically-shaped AgNPs at 2 nm which is marked in red in (a) showing fringer spacing of 0.23 nm (b). Inset in (b) is its corresponding SAED

Selected-area electron diffraction (SAED) and high resolution (HR) TEM studies were used to explain the crystal structure of the AgNPs. Figure 7a-b showed HRTEM images of AgNPs at 10 nm and 2 nm magnifications. Well-resolved lattice fringes with an interplanar spacing of 0.23 nm of spherical silver were verificated by HRTEM measurement (in Figure 7b) obtained from the particle which was red-marked in the image at 10 nm in Figure 7a. Also, SAED pattern of the particle was given in the inset of Figure 7b. The SAED pattern with bright spots on the rings clearly supported the crystalline structure of AgNPs.

In the energy dispersive X-ray analysis (EDX) analysis of AgNPs given in Figure 8 showed a peak of silver which was observed at 3 keV from the silver atoms in AgNPs. The peak proved the presence of silver nanoparticles. Because, metallic silver nanocrystals have a characteristic optical absorption peak at about 3 keV [47]. The other peaks based on carbon and copper arose because of the carbon coated copper grid of TEM. Furthermore, AgNPs were also characterized by elemental mapping results represent the distribution of elements.

According to elemental mapping results given in Figure 8 inset, the bright spot in the electron micrograph region of synthesized AgNPs proved the elemental silver atom.

FT-IR spectroscopy measurements were performed to reveale the functional groups that bound on the silver surface and involved in the biosynthesis of silver nanoparticles. The *Spirogyra* sp. extract displays a number of absorption peaks, stating its complex nature. In the FT-IR spectra of the *Spirogyra* sp. extract (Figure 9a), the intense and broad band in the range of 3500 – 3200 cm^{-1} belongs to the O–H stretching, which is usually characteristically observed in phenols and hydrogen bonded alcohols. Therefore, the peak of 3264 cm^{-1} stands for the stretching vibrations of –OH [48].

Figure 8. EDX spectrum of AgNPs. Inset the TEM micrograph of silver nanoparticles pellet solution for silver elements

Figure 9. The FT-IR spectra of the *Spirogyra* sp. extract (a) and AgNPs (b)

The band of 2935 cm^{-1} is assigned to the stretching vibration of aliphatic C–H bonds from –CH$_3$ and –CH$_2$ functional groups. The absorption peak at around 1574 cm^{-1} could be attributed to the stretching vibration of C=O, C=N, and C=C. The stretching vibration of C–N appears at 1401 cm^{-1}. The peaks in the 1000-1200 cm^{-1} region are assigned to the stretching vibration of C–O–C group. So, the sharp and broad absorption peak of 1025 cm^{-1} could be contributed to the stretching vibration bands of symmetric C–O groups such as O=C–O, C–O–C and epoxide. The FT-IR study of the algal extract demonstrates the presence of –C=O/–C=C/–C=N, –OH (hydroxyl), C–O/C–N and –N–H (amine) groups in the algal extract. It is well known that this functional groups especially carboxy, hydroxy and amide groups take part in the reduction of Ag$^+$ ion to metallic silver.

In case of the silver containing the *Spirogyra* sp. extract (AgNPs), the spectrum (Figure 8b) show medium or strong absorption peaks at 3282, 2920, 1627 and 1150/1075/1024 cm^{-1} suggesting –OH [48], aliphatic –CH stretching [49], C=O stretching frequency [50] and C–O stretching of ethers, phenols and epoxide [51]. Comparison of the spectra of *Spirogyra* sp. extract and AgNPs suggested that in silver containing the *Spirogyra* sp. extract (AgNPs) O–H, C=H stretching frequency shifted from 1574 to 1627 cm^{-1} to produce nanoparticles. In case of AgNPs, the stretching frequencies of –OH, aliphatic –CH and C=O shifted from 3284, 2935 and 1574 cm^{-1} to 3282, 2920 and 1627 cm^{-1}, respectively. Otherwise, clearly more absorption peaks were formed on broad spectral range of 1400–1025 cm^{-1} on AgNPs indicating interactions between the silver nanoparticles.

3.2. Antioxidant activity and α-Glucosidase Enzyme inhibition of the extract and AgNP of Spirogyra sp.

Determination of antioxidant activity (or capacity) of samples of various is based on different methodologies and assays. In the study were used three antioxidant activity methods with different mechanisms. The antioxidant activity values of the *Spirogyra* sp. extracts for DPPH TPC, TFC tests were determined as 21.78 (mg/mL IC$_{50}$), 80.03 (GAE µg/mL) and 0.015 (QAE µg/mL), respectively. The values in the silver nanoparticles (AgNPs) were also measured as 17.20 (mg/mL IC50), 97.61 (GAE µg/mL) 0.027 (QAE µg/mL). In addition, values of % α-glucosidase enzyme inhibition were determined as 44.70 in the algal extract and 63.50 in silver nanoparticules (Table 1).
Antioxidant activity and α-glucosidase enzyme inhibition values of silver nanoparticles are higher than algal extracts. Bedlovičová et al. [52] pointed out that antioxidant activity values of silver nanoparticles were always not higher than plant extracts. The higher antioxidant activity of silver nanoparticle than plant

extracts may be associated with content and the amount and variety of chemical compounds of the plant. In one study, silver nanoparticles were synthesized using various phenolic compounds (such as flavonoids, benzoic acids, cinnamic acids). The antioxidant capacities of structurally different phenolic compounds were evaluated. The hydroxylation of the aromatic ring appeared to play an important role in forming silver NPs. The high degree of hydroxylation in the chemical structures of phenolic compounds showed a high radical scavenging capacity and a tendency to reduce Ag$^+$ to AgNPs [53]. α-glucosidase enzyme is a key enzyme for non-insulin treatments of diabetes because of that it catalyzes the final step in the digestion process of carbohydrates [54]. Some studies indicated that plant silver nanoparticles have remerkable α-glucosidase enzyme inhibition [55, 56].

4. Conclusion

Silver nanoparticle synthesis is based on the reduction procedure performed by a chemical or biological reducing agent. Biosynthesis of AgNPs consist of bacteria, yeast, fungi, algal species and plant/plant extracts. In this study, the *Spirogyra* sp. extract was considered as an appropriate substance for the green biosynthesis of AgNPs. The algal extract acted as both a reducing and stabilizing agent. The green approach, based on silver nanoparticle synthesis using the *Spirogyra* sp. extracts, is highly remarkable in terms of being energy-saving (heated at only 60 °C for 2 h), more cost-effective (not require any commercial chemicals other than AgNO$_3$) and environmentally friendly (carry out in an aqueous medium without the use of any toxic chemicals and organic solvents). The UV-vis spectra primarily showed that AgNPs has a SPR absorption peak at about 488 nm. The concentration of AgNO$_3$ and reaction time were optimized to prepare AgNPs. So, the greatest increase in absorbance of the SPR peak of AgNPs were obtained with AgNO$_3$ at 1mM concentration. Choosing the lowest concentration of AgNO$_3$ is much more useful in terms of less silver accumulation in the environment. The colo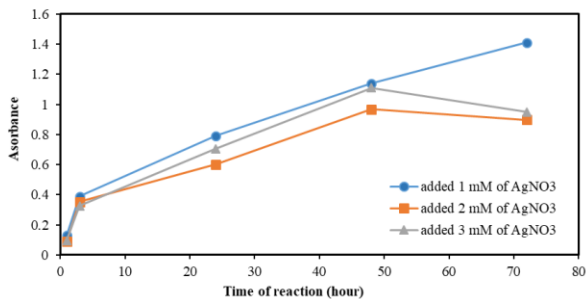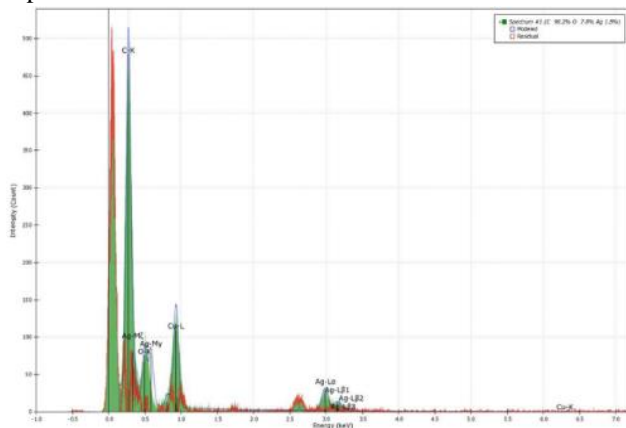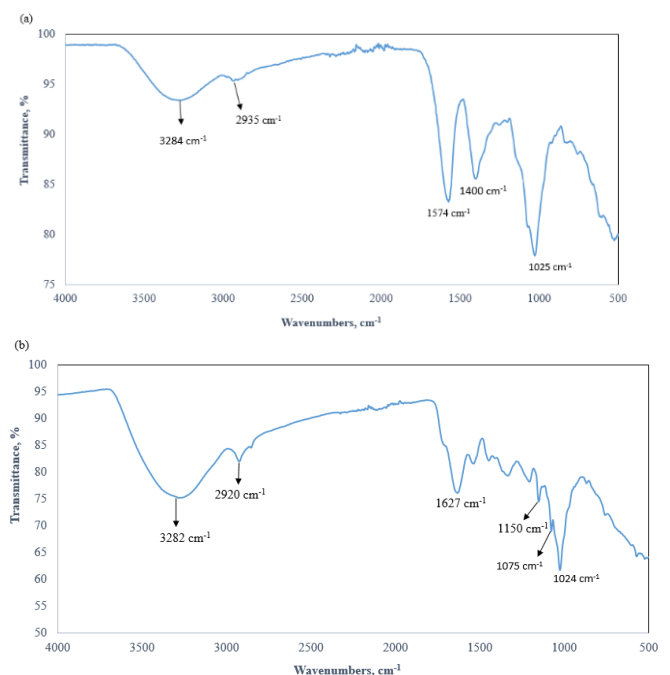r change of AgNPs solution to reddish color visually noticed was completed at the end of 24 h which was determined as ideal reaction time. FTIR spectroscopy confirmed the surface modification of the *Spirogyra* sp. extract and AgNPs by water-soluble biomolecules.

The FT-IR study of the *Spirogyra* sp. extract demonstrates the presence of –C=O/–C=C/–C=N, –OH (hydroxyl), C-O/C-N and –N-H (amine) groups in the *Spirogyra* sp. Extract [17, 23, 26]. This functional groups take part in the reduction of Ag$^+$ ion to metallic silver. TEM images of AgNPs reveals that, the nanoparticles have two different shapes as spherical or oval shaped. The analysis of TEM confirmed that the average particle size of AgNPs was 18.3 nm.

Table 1. Enzyme inhibition and antioxidant activity of the *Spirogyra* sp. extract and AgNP

Samples	Enzyme inhibition	Antioxidant activity		
	% α-Glucosidase	DPPH (mg/mLIC$_{50}$)	TPC (GAE μg/mL)	TFC (QAE μg/mL)
Spirogyra sp. extract	44.70 ± 0.12	21.78 ± 0.11	80.03 ± 0.19	0.015 ± 0.01
AgNPs	63.50 ± 0.23	17.20 ± 0.07	97.61 ± 0.27	0.027 ± 0.03

Well-resolved lattice fringes with an interplanar spacing of 0.23 nm of spherical silver were verificated by HRTEM measurement. The SAED pattern with bright spots on the rings clearly supported the crystalline structure of AgNPs. EDX analysis of AgNPs showed that the peak at 3 keV from the silver atoms proved the presence of silver nanoparticles. Furthermore, the elemental mapping results of AgNPs represented the distribution of elements. According to this results, the bright spots in the electron micrograph region of AgNPs proved the elemental silver atom.

The antioxidant activity values of the algal extracts for DPPH TPC, TFC tests were determined as 21.78 (mg/mL IC$_{50}$), 80.03 (GAE μg/mL) and 0.015 (QAE μg/mL), respectively. In addition, the values of the same tests were measured as 17.20 (mg/mL IC$_{50}$), 97.61 (GAE μg/mL) 0.027 (QAE μg/mL) for AgNPs. Furthermore, values of % α-glucosidase enzyme inhibition were determined as 44.70 in the *Spirogyra* sp. extract and 63.50 in AgNPs. Antioxidant activity and α-glucosidase enzyme inhibition values of silver nanoparticles are higher than the values of Spirogyra sp. extracts.

Declaration

The authors declared no potential conflicts of interest with respect to the research, authorship, and/or publication of this article. The authors also declared that this article is original, was prepared in accordance with international publication and research ethics, and ethical committee permission or any special permission is not required.

Author Contributions

Aysel BAŞOĞLU (AB) and Zeynep AKAR (ZA) developed the methodology. AB and ZA performed biosynthesis and characterization of silver nanoparticles (AgNPs). AB wrote the Biosynthesis of silver nanoparticles (AgNPs) and Characterization of silver nanoparticles. ZA wrote the Antioxidant activity of extract and silver nanoparticles of *Spirogyra* sp. AB and ZA supervised and improved the study.

Acknowledgment

Nomenclature

AgNPs	: Silver nanoparticles
FT-IR	: Fourier transform infrared spectroscopy
TEM	: Transmission electron microscopy
EDX	: Energy dispersive *X*-ray analysis
SAED	: Selected area electron diffraction
DPPH	: 1,1-diphenyl-2-picrylhydrazil
TPC	: Total phenolic content
TFC	: Total flavonoid content
UV-Vis	: Ultraviolet–visible
IC$_{50}$	: Half-maximal inhibitory concentration
GAE	: Gallic acid equivalent
MIC	: Minimum inhibitory concentration
MBC	: Minimum bactericidal concentration
QAE	: Quercetin antioxidant equivalent

References

1. Elias, E., E. Elemike, D. Olugbenga, D. Inyang, J. Samuel, and O. Chinedu, *2-Imino-(3,4-dimethoxybenzyl) ethanesulfonic acid Schiff base anchored silver nano-complex mediated by sugar cane juice and their antibacterial activities.* J Appl Res Technol, 2016. **14**: p. 38-46,

2. Husen, A., and K. S. Siddiq, *Phytosynthesis of nanoparticles: concept, controversy and application.* Nanoscale Res Lett, 2014. **9**(1): p. 9-229.

3. Sakar, M., S. Balakumar, P. Saravanan, and S. N. Jaisankar, *Annealing temperature mediated physical properties of bismuth ferrite (BiFeO$_3$) nanostructures synthesized by a novel wet chemical method.* Mater Res Bull, 2013. **48**: p. 2878–2885.

4. Tang B, L. Yuan, T. Shi, L. Yu, Y. Zhu, *Preparation of nano-sized magnetic particles from spent pickling liquors by ultrasonic-assisted chemical co-precipitation.* J Hazard Mater, 2009. **163**: p. 1173–1178.

5. Chen. X., T. Todorova, A. Vimont, V. Ruaux, Z. Qin, J. P. Gilson, and V. Valtchev. *In situ and post-synthesis control of physicochemical properties of FER-type crystals.* Microporous Mesoporous Mater, 2014. **200**: p. 334–342.

6. Annamalai, A., V. L. P. Christina, D. Sudha, M. Kalpana, and P. T. V. Lakshmi, *Green synthesis, characterization and antimicrobial activity of Au NPs using Euphorbia hirta L. leaf extract.* Colloids Surf. B: Biointerfaces, 2013. **108**: p: 60–65.

7. Das, S. K., and E. Marsili "*Bioinspired metal nanoparticle: synthesis, properties and application,*" in *Nanotechnology and Nanomaterials.* InTech, 2011. **11**: p. 253–278.

8. Faraday M., *Experimental relations of gold (and other metals) to light.* Philos Trans R Soc Lond B Biol Sci, 1857. **147** : p. 145–181.

9. Grier N., *Silver and Its Compounds. In: Block, S.S., Ed., Disinfection, Sterilization and Preservation.* Lee and Febiger, Philadelphia, 1968. p. 375-398.

10. Hill, W. R. and D. M. Pillsbury, *Argyria—The Pharmacology of Silver.* Williams and Williams, Baltimore 1939.

11. Galib, M. Barve, M. Mashru, C. Jagtap, B. J. Patgiri and P. K. Prajapati, *Therapeutic potentials of metals in ancient India: A review through Charaka Samhita.* J Ayurveda Integr Med, 2011. **2**(2): p. 55-63.

12. Stevens, K. N. J., O. Crespo-Biel, E. E. M. van den Bosch, A. A. Dias, M. L. W. Knetsch, Y. B. J. Aldenhoff, F. H. van der Veen, J. G. Maessen, E. E. Stobberingh, and L. H. Koole *The relationship between the antimicrobial effect of catheter coatings containing silver nanoparticles and the coagulation of contacting blood.* Biomaterials, 2009. **30**: p. 3682–3690.

13. Austin, L. A., M. A. Mackey, E. C. Dreaden, and M. A. El-Sayed. *The optical, photothermal, and facile surface chemical properties of gold and silver nanoparticles in biodiagnostics, therapy, and drug delivery.* Arch Toxicol, 2014. **88**(7): p. 1391–1417.

14. Lv, Y., H. Liu, Z. Wang, S. Liu, L. Hao, Y. Sang, D. Liu, J. Wang, and R. I. *Boughton Silver nanoparticle-decorated porous ceramic composite for water treatment.* J. Membr. Sci, 2009. **331**: p. 50–56.

15. Martinez-Abad, A., J. M. Lagaron, and M. J. Ocio, *Development and characterization of silver-based antimicrobial ethylene-vinyl alcohol copolymer (EVOH) films for food-packaging applications.* J Agric Food Chem, 2012. **60**: p. 5350-5359.

16. Zhang, F., X. Wu, Y. Chen and Lin H, *Application of silver nanoparticles to cotton fabric as an antibacterial textile finish.* Fibers Polym, 2009. **10**(4): p. 496-501.

17. Sani, E., P. D. Ninni, L. Colla, S. Barison and F. Agresti, *Optical Properties of Mixed Nanofluids Containing Carbon Nanohorns and Silver Nanoparticles for Solar Energy Applications.* J. Nanosci Nanotechnol, 2015. **15**(5): p. 3568-3573.

18. Arroyo, G. V., A. T. Madrid, A. F. Gavilanes, B. Naranjo, A. Debut, M. T. Arias and Y. Angulo, *Green synthesis of silver nanoparticles for application in cosmetic.* J Environ Sci Health Part A, 2020. **55**(11): p. 1304-1320.

19. Song, K. C., S. M. Lee, T. S. Park, and B. S. Lee, *Preparation of colloidal silver nanoparticles by chemical reduction method.* Korean J. Chem. Eng, 2009. **26**(1): p. 153-155.

20. Steinigeweg, D., and S. Schlücker, *Monodispersity and size control in the synthesis of 20–100 nm quasi-spherical silver nanoparticles by citrate and ascorbic acid reduction in glycerol–water mixtures.* Chem Commun, 2012. **48**: p. 8682-8684.

21. Anastas, P. T. and J. C. Warner, Green Chemistry; Oxford University Press: Oxford, UK, 2000.

22. Gałuszka, A., Z. Migaszewski, J. Namiesˊnik, *The 12 principles of green analytical chemistry and the significance mnemonic of green analytical practices.* Trends Anal Chem Trends, 2013. **50**: p. 78–84.

23. Gurunathan, S., K. Kalishwaralal, R. Vaidyanathan, V. Deepak, S. R. K. Pandian, J. Muniyandi, N. Hariharan, S. H. Eom, *Biosynthesis, purification and characterization of silver nanoparticles using Escherichia coli.* Colloids Surf. B Biointerfaces, 2009. **74**: p. 328–335.

24. Sivaraj, A., V. Kumar, R. Sunder, K. Parthasarathy, and G. Kasivelu, *Commercial Yeast Extracts Mediated Green Synthesis of Silver Chloride Nanoparticles and their Anti-mycobacterial.* Activity J Clust Sci, 2020. **31**: p. 287–291.

25. Sanghi, R., and P. Verma, *Biomimetic synthesis and characterisation of protein capped silver nanoparticles.* Bioresour Technol, 2009. **100**: p. 501–504.

26. Shaligram, N. S., M. Bule, R. Bhambure, R. S. Singhal, S. K. Singh, G. Szakacs and A. Pandey, *Biosynthesis of silver nanoparticles using aqueous extract from the compactin producing fungal strain.* Process Biochem, 2009. **44**: p. 939–943.

27. Pugazhendhi, A., D. Prabakar, J. M. Jacob, I. Karuppusamy, R. G. Saratale, *Synthesis and characterization of silver nanoparticles using Gelidium amansii and its antimicrobial property against various pathogenic bacteria.* Microb Pathog, 2018. **114**: p. 41–45.

28. Kathiraven, T., A. Sundaramanickam, N. Shanmugam, T. Balasubramanian, *Green synthesis of silver nanoparticles using marine algae Caulerpa racemosa and their antibacterial activity against some human pathogens.* Appl Nanosci, 2015. **5**: p. 499–504.

29. Kumar, P., S. S. Selvi, A. L. Prabha, K. P. Kumar, R. S. Ganeshkumar, and M. Govindaraju, *Synthesis of silver nanoparticles from Sargassum tenerrimum and screening phytochemicals for its anti-bacterial activity.* Nano Biomed. Eng, 2012. **4**(1): p. 12–16.

30. Rolim W. R., M. T. Pelegrino, B. de Araújo Lima, L. S. Ferraz, F. N. Costa, , J. S. Bernardes, T. Rodigues and M. Brocchic, *Green tea extract mediated biogenic synthesis of silver nanoparticles: Characterization, cytotoxicity evaluation and antibacterial activity.* Appl Surf Sci, 2019. **463**: p. 66−74.

31. Ghanbar, F., A. Mirzaie, F. Ashrafi, H. Noorbazargan, M. D. Jalali, S. Salehi, S. A. S. Shandiz, *Antioxidant, antibacterial and anticancer properties of phyto-synthesised Artemisia quttensis Podlech extract mediated AgNPs.* IET Nanobiotechnol, 2017. **11**(4): p. 485–492.

32. Saravanakumar, K., R. Chelliah, S. Shanmugam, N.B. Varukattu, D. H. Oh, K. Kathiresan, and M.-H. Wang, *Green synthesis and characterization of biologically active nanosilver from seed extract of Gardenia jasminoides Ellis.* J Photochem Photobiol B, 2018. **185**: p. 126–135.

33. Islam, S.-U., B. S. Butola, A. Gupta, and A. Roy, *Multifunctional finishing of cellulosic fabric via facile, rapid in-situ green synthesis of AgNPs using pomegranate peel extract biomolecules.* Sustain Chem Pharm, 2019. **12**: p. 100-135.

34. Li, A. N., S. Li, Y. J. Zhang, X. R. Xu, Y. M. Chen, and H. B. Li, *Resources and biological activities of natural polyphenols.* Nutrients, 2014. **6**: p. 6020-6047.

35. Majumdar, M., S. Shivalkar, A. Pal, M. L. Verma, A. K. Sahoo, and D. N. Roy, *Chapter 15 - Nanotechnology for enhanced bioactivity of bioactive compounds.* Biotechnological Production of Bioactive Compounds, Elsevier, 2020. p. 433-466.

36. Akar, B., Z. Akar and B. Sahin. *Identification of Antioxidant Activity by Different Methods of a Freshwater Alga Microspora Sp. Collected From a High Mountain Lake.* Hittite J of Sci and Eng, 2019. **6**(1): p. 25-29.

37. Elgamouz, A., H. Idriss, C. Nassab, A. Bihi, K. Bajou, K. Hasan, M. A. Haija, and S. P. Patole, *Green Synthesis,*

Characterization, Antimicrobial, Anti-Cancer, and Optimization of Colorimetric Sensing of Hydrogen Peroxide of Algae Extract Capped Silver Nanoparticles. Nanomater, 2020. **10**: p. 1861-1880.

38. Salari, Z., F. Danafar, S. Dabaghi, and S. A. Ataei, *Sustainable synthesis of silver nanoparticles using macroalgae Spirogyra varians and analysis of their antibacterial activity.* Journal of Saudi Chemical Society 2016. **20(4)**: p. 459–464.

39. Sivaraman, S. K., I. Elango, S. Kumar, and V. A. Santhanam, *A green protocol for room temperature synthesis of silver nanoparticles in seconds.* Curr Sci, 2009. **97**(10): p. 1055–1059.

40. Hartland, G. V., *Optical studies of dynamics in noble metal nanostructures.* Chem Rev, 2011. **111**: p. 3858–3887.

41. Brand-Williams, W., M. E. Cuvelier, and C. Berset, *Use of a free radical method to evaluate antioxidant activity.* Food Sci Technol_LEB, 1995. **28**: p. 25–30.

42. Slinkard, K. and V. L. Singleton, *Total phenol analysis: Automation and comparison with manual methods.* Am J Enol Vitic, 1977. **28**(1): p. 49–55.

43. Fukumoto L. R., and G. Mazza, *Assessing antioxidant and prooxidant activities of phenolic compounds.* J Agric Food Chem, 2000. **48**: p. 3597–3604.

44. Yu Z, Y. Yin, W. Zhao, J. Liu, and F. Chen, *Anti-diabetic activity peptides from albumin against a-glucosidase and a-amylase*, Food Chemistry, 2012. **135**: p. 2078–2085.

45. Henglein, A. *Physicochemical properties of small metal particles in solution: microelectrode reactions, chemisorption, composite metal particles, and the atom-to-metal transition.* J Phys Chem, 1993. **97**(21): p. 5457–5471.

46. Soliman, H., A. Elsayed, and A. Dyaa, *Antimicrobial activity of silver nanoparticles biosynthesised by Rhodotorula sp. strain ATL72.* Egypt J basic Appl Sci, 2018. **5**(3): p. 228–233.

47. Kalimuthu, K., R. S. Babu, D. Venkataraman, M. Bilal, S. Gurunathan, *Biosynthesis of silver nanocrystals by Bacillus licheniformis.* Colloids Surf. B Biointerfaces, 2008. **65**: p. 150–153.

48. Ayo, R. G., J. O. Amupitan, I. G. Ndukwe, and O. T. Audu, *Some chemical constituents of the leaves of Cassia nigricans.* Vahl. Afr J Pure Appl Chem, 2009. **3**(11): p. 208–11.

49. Kaswar, S. M. A., G. Mostafa, E. Huq, N. Nahar, Y. Ozeki, *Chemical constituents and hemolytic activity of Macrotyloma uniflorum L.* Int J Biol Chem (2009) **3**(1): p. 42–8.

50. Selvi, J. A., S. Rajendran, V. G. Sri, A. J. Amalraj, and B Narayanasamy, *Corrosion inhibition by beet root extract.* Port Electrochimica Acta, 2009. 27(1): p. 1-11.

51. Chang Chien, S. W., M. C. Wang, C. C. Huang, and K. Seshaiah, *Characterization of humic substances derived from swine manure-based compost and correlation of their characteristics with reactivities with heavy metals.* J Agric Food Chem, 2007. **55**: p. 4820–7.

52. Bedlovičová, Z., I. Strapáč, M. Baláž, and A. Salayová, *A brief overview on antioxidant activity determination of silver nanoparticles.* Mol 2020. **25**:3191-3215.

53. Docea, A. O., D. Calina, A. M. Buga, O. Zlatian, M.M.B. Paoliello, G. D. Mogosanu, C. T. Streba, E. L. Popescu, A. E. Stoica, A. C., Bîrcă, B. Ş. Vasile, A. M. Grumezescu and L. Mogoanta, *The effect of silver nanoparticles on antioxidant/pro-oxidant balance in a Murine Model.* International Journal of Molecular Sciences, 2021. **21**: p. 1233-1239.

54. Kumar, S., S. Narwal, V. Kumar, and O. Prakash, *α-glucosidase inhibitors from plants: A natural approach to treat diabetes.* Pharmacogn. Rev, 2011. **5**(9):19-29.

55. Balan, K., W. Qing, Y. Wang, X. Liu, T. Palvannan, Y. Wang and, Y. Zhang, *Antidiabetic activity of silver nanoparticles from green synthesis using Lonicera japonica leaf extract.* RSC Adv, 2016. **6**(46): p. 40162-40168.

56. Jini, D., and S. Sharmila, *Green synthesis of silver nanoparticles from Allium cepa and its in vitro antidiabetic activity.* Mater Today Proc, 2020. **22**: p. 432–438

Research Article

Production of activated carbon from the waste paper by chemical activation method

Derya Ozdemir [a,*] (iD)*, Saban Bulbul* [b] (iD) *and Mehmet Emin Ergun* [c] (iD)

aNecmettin Erbakan University,The Graduate School of Natural and Applied Science, Konya, 42090, Turkey
bNecmettin Erbakan University, Faculty of Seydişehir Ahmet Cengiz Engineering Faculty, Konya, 42370, Turkey
cAlanya Alaaddin Keykubat University, Akseki Vocational High School, Antalya,07630, Turkey

ABSTRACT

The cellulose and paper industry accounts for a large part of the circular economy. The need for activated carbons is gradually increasing, especially in the environmental and energy fields. In this study, the production of activated carbon from waste papers was carried out with the help of the chemical activation method and activation agents (phosphoric acid and zinc chloride). The parameters used in the experiments and analyzed were kept constant for all activated carbons. The density values of activated carbon were analyzed more than once in each sample with a helium-gas pycnometer device. Fourier transform infrared spectroscopy (FT-IR) was used to detect functional groups in the structure of activated carbon, and a field emission scanning electron microscope (FE-SEM) was used to study surface properties and porosity development. The distributions of activated carbons and their elemental analysis were examined by energy dispersive spectrometry (EDS) and Mapping analyses. When the results obtained from the activated carbons produced from waste paper in the study were compared with commercial activated carbon, it was observed that the waste paper had a better surface and pore structure than commercial activated carbon for the production of activated carbon, and the activation process was successfully performed.

1. Introduction

Conventional activated carbons are produced from organic and inorganic substances with high carbon content, such as wood, peat, bituminous coal, and anthracite [1].The increase in the current production of activated carbon due to the increasing demand for adsorbent materials to solve environmental problems has pushed the industry and research groups to look for alternative ways in which different methods and techniques are used. Currently, the use of many agricultural and industrial wastes (energy crops, agricultural biomass residues, forest residues, and food-based waste) as a renewable raw material source for producing activated carbons has paved the way for the production of low-cost and larger amounts of activated carbon, and many scientific studies have been conducted on this topic [2–4].

Activated carbon is a term used to refer to well-built porous structures and carbon-rich materials. Activated carbon is a versatile material with a surface area containing high and well-organized macro, meso, and micropores, includes a wide variety of chemical functional groups and can find different application areas for itself [5].Physical and chemical activation methods are used to improve the pore structure in carbon. Physical activation methods are an older method compared to the chemical activation method and it is widely used in the activated carbon production. Oxygen and hydrogen are completely removed from the material used in the production of activated carbon, and the main skeleton is formed. Then, with the use of water vapor or CO_2 gas or both as an activator agent for the activation process at a temperature of 800-1000 °C, the activation process is realized and activated carbon is produced [6]. However, the limited extent of pore development, not very large surface area, low micropores volume, the need for high temperatures for production, low adsorption rate, and relatively low activation rate are the main disadvantages of the physical activation method [7].

Many researchers around the world are performing studies on the chemical activation method to produce activated carbon. Chemical activation is often preferred because it allows the production of activated carbon with

---

higher carbon content by using lower heating temperatures and faster reaction times [8].Chemicals such as potassium hydroxide, potassium carbonate, phosphoric acid, sulfuric acid, zinc chloride, hydrochloric acid, pyrophosphoric acid, nitric acid, sodium hydroxide, potassium carbonate, sodium chloride, ammonium chloride, ferric chloride, sodium carbonate, and hydrogen peroxide are used as activating agents [4,9–19]. Alkalis such as potassium hydroxide (KOH) are usually realized with a large impregnation rate [20,21] between 400~1000 °C and are very effective in forming micropores [22]. Considering the environmental effects, energy cost, and carbon efficiency, phosphoric acid (H_3PO_4) is remarkable, and its use in large-scale activated carbon production has steadily increased in recent years [23]. Phosphoric acid (H_3PO_4) can occur at low temperatures of 400~600 °C with a low impregnation rate and consists mainly of mesoporous with a surface area of about 1000~1500 $m^2 \cdot g^{-1}$ BET[24,25]. As a catalyst, phosphoric acid (H_3PO_4) promotes bond fragmentation reactions. It facilitates cross-linking by forming a connecting layer, such as phosphate and polyphosphate esters, that can maintain the condensation and internal pore structure through the cycle and thus prevent excessive combustion on carbon activation [26].In the literature, some studies in which activated carbon was produced using different materials are as follows.

Usmani et al. reported that a product with a surface area of 942 $m^2.g^{-1}$ was obtained from lignite coal with a high sulfur content using a chemical activation method and a zinc chloride activation agent at a temperature of 650 °C and after one-hour activation [27]. In the study conducted by Liu et al., they activated hemp waste with zinc chloride and determined the surface area of the activated carbon they obtained to be 1100 $m^2.g^{-1}$ [28].

In a study conducted by Zhang and his colleagues, the effects of physical activation of activated carbon obtained from bamboo on pore structure and surface chemistry were studied, and it was concluded that the activation conditions significantly affected the surface area development, porosity, efficiency, and combustion of activated carbon [29].

In the study conducted by Fernandez et al., it was found that the surface area of activated carbon produced from the orange peel as a result of activation with phosphoric acid developed up to 1090 $m^2.gr^{-1}$. It was stated that the obtained activated carbon was successfully used in the adsorption of waste dyes in water [30]. In another study, the micro-porosity of the activated carbon produced from the sawdust of a rubber tree was improved by chemical activation with potassium hydroxide. The surface area of the produced activated carbon was found to be 1491 $m^2.gr^{-1}$ [31].

Today, sustainability is gaining importance with the developing technology. The cellulose and paper industry also forms a large part of the circular economy, and the need for activated carbon, especially in the environmental and energy fields, is increasing day by day. The purpose of this study was to use waste paper for the production of activated carbon and to evaluate the effects of experimental parameters and chemical activation agents ($ZnCl_2$ and H_3PO_4) used in the production of activated carbon.

2. Material and Method

Used writing paper waste utilized in this study. During the activation process, zinc chloride ($ZnCl_2$) and phosphoric acid (H_3PO_4) were used, while hydrochloric acid (HCl) and potassium hydroxide (KOH) were used to wash the activated carbon. All the chemicals used in this study were of analytical purity, and the production of activated carbon from the waste paper was carried out with the help of phosphoric acid and salt (zinc chloride) activation agents (Figure 1). The $ZnCl_2$, H_3PO_4, HCl, and KOH materials used in the study were obtained from Bereket Chemical Company (Bereket Chemical Medical Technical Trade and Industry Ltd. Co.).

Production of activated carbon with phosphoric acid:
3 kg of waste paper in small pieces was mixed by adding 1.5 liters of phosphoric acid (50% wt.) and 3 liters of pure water. In order for the waste paper to react with phosphoric acid, it was treated at 110°C for two hours. Then, the mixture was dried at 80°C oven for 24 hours. The dried material was subjected to carbonization for 1.5 hours at 600°C under argon gas (50 milliliters/min) for the activation process, and then cooled at room temperature. It was washed with 0.5 M KOH and then with hot deionized water until the pH value was 6-6.5. After the washed activated carbon was dried at 100°C for 6 hours, it was ground and ready for use [30]

Production of activated carbon with zinc chloride:
3 kg of waste paper in small pieces was kneaded by adding 1.5 kg of zinc chloride and 3 liters of pure water until it became a dough. In order for the raw material to react with zinc chloride, it was treated for 24 hours at room temperature. Then, the mixture was dried by keeping it in the oven at 80°C for 24 hours. After the dried material was subjected to carbonization process for 1.5 hours at 600 °C under argon gas (50 mL/min) for the activation process, it was cooled at room temperature.

2.1 Characterization

FE-SEM images of activated carbons produced by the chemical activation method were obtained by FT-IR spectroscopy. To determine the density of the activated carbons produced, a pycnometer (Micromeritics Accupyc II 1340) and a 10 cm^3 sample cup were used.
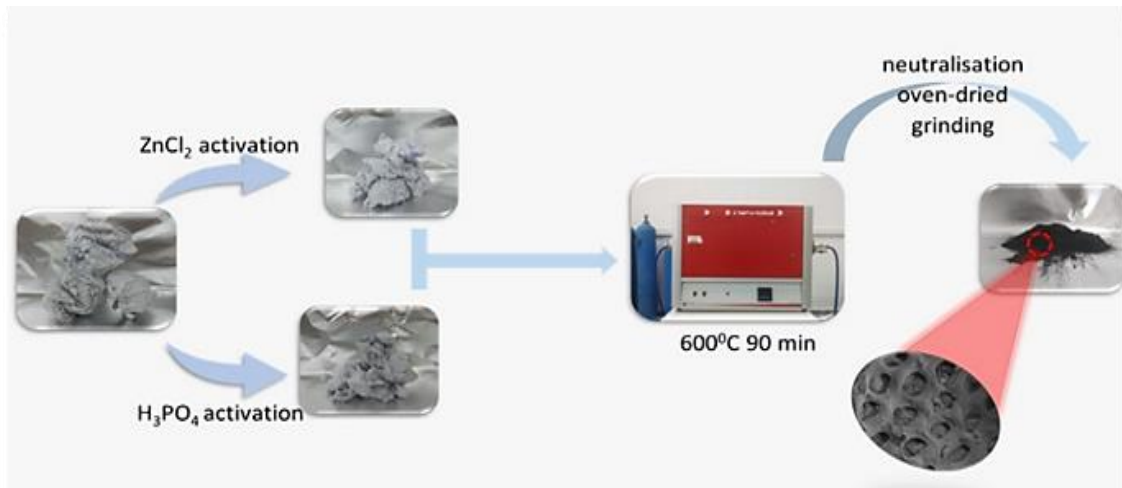
Figure 1. Production of activated carbon from waste paper

The sample was carefully prepared and loaded into the sample cup within the Micromeritics instrument. The density value was then obtained using the Accupyc II 1340 Pyc software. Helium gas was preferred because it is an ineffective gas that penetrates tiny sub-micron pores up to 0.3 nm in size [32]. A field emission scanning electron microscope (FE-SEM) (Hitachi–SU 1510) was used to examine the surface structure and pore development morphologies of activated carbons. In order to improve the quality of conductivity, an iridium (Ir) coating process with a thickness of 5 nm was applied to the surfaces of activated carbons. The operating voltage of the microscope was determined as 20 kV, and microstructure images of activated carbons were examined. For the purpose of characterizing the chemical structure of the resulting activated carbon, Fourier transform infrared spectroscopy (FT-IR) analyses were performed to determine the functional groups in the structure of activated carbon. The FT-IR spectra were determined with the FT-IR (Thermo Scientific - Nicolet iS20) device in the range of 4000-400 cm^{-1}. As a result, detailed work was carried out at each stage of the experiments to improve the micro-porosity and surface area of the activated carbon produced from waste paper during the experimental process. After the carbonized materials were washed with 0.5 M HCl solution, the activated carbon was washed with hot deionized water until the pH value was 6-6.5. Then, it was dried at 100°C for 6 hours and made ready for use by grinding [33].

3. Results and Discussion

FTIR, density, FE-SEM, EDS, and Mapping analyses of the produced activated carbon were performed and compared both with commercial activated carbon and among themselves. The parameters used in the experiments and analyzes were kept constant for all activated carbons.

3.1 FTIR Analysis

FT-IR analyses were performed to determine the functional groups in the structure of activated carbon produced as a result of the chemical activation of waste paper with $ZnCl_2$ and H_3PO_4 agents. The FT-IR spectrum of activated carbons produced by the chemical activation method is given in Figure 2.

When the FT-IR spectra in Figure 2 are examined, the presence of the OH functional group connected by peak hydrogen bonds at 3670 and 3375 cm^{-1} wavelengths is seen[34]. Peaks observed around 2970-2976 cm^{-1} indicate the aliphatic C-H functional group, while peaks formed at wavelengths of 2310-2320 cm^{-1} indicate the C≡C functional group in alkyne groups [35] .The peaks around the wavelengths of 1615-1515 cm^{-1} are associated with C=O or C=C functional groups [36]. The peak in the range of 1200-1500 cm-1 refers to the C–O groups [37] . The sharp peak formed around 1060-1040 cm^{-1} is associated with the C-O-C group [38]. Peaks smaller than 1000 cm^{-1} refer to functional groups originating from the aromatic ring [34]. On the other hand, the peaks in the range of 1127-973 cm^{-1} bands are the P=O and P=O-OH groups, which occur due to phosphoric acid [39].
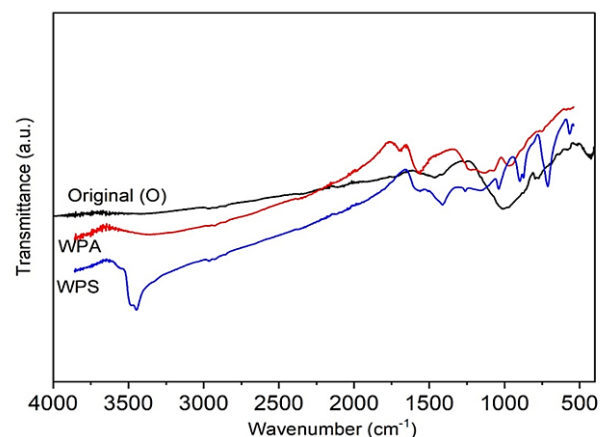
Figure 2. FT-IR spectrum of activated carbons

According to the spectrum analysis, in common with all three samples, in the wavelength range of 400-4000 cm^{-1}, the strongest adsorption band in the WPA, WPS, and O codes is in the wavelength range of 3482-3456 cm^{-1} and corresponds to the -OH functional group. It is known that in nature, hydroxyl and carboxyl groups make the surface of the activated carbon acidic [40]. Therefore, the adsorption of activated carbon and the permeability percentage are affected. In the study, it is seen that in the zinc chloride (WPS) activation performed at a wavelength of 3451 cm^{-1}, the percentage of permeability decreases significantly compared to phosphoric acid (WPA) and ready-made (O) activated carbon. Peaks in the range of 1586-1405 cm^{-1} band indicate the C–O group, while peaks in the 1082-1014 cm^{-1} wavelength range indicate the P=O and P=O-OH groups. Finally, the 630-544 cm^{-1} band refers to the C-C and C-O aromatic functional groups. It is observed that in the content of the prepared activated carbons, there is not only carbon but also other hetero atoms such as hydrogen, oxygen, nitrogen, and phosphorus.

3.2 Density Analysis

Table 1 shows the densities of activated carbon obtained from waste paper and commercial activated carbon. In the analysis results, the WPS density increases to 1.824 gr/cm^3 and the WPA density increases to 1.653 gr/cm^3. The increase in the actual density values measured by the helium gas pycnometer is related to the formation of a denser array due to the high stability of the cross-links of the molecules. It is also known that as the temperature increases and as planar clusters of aromatic rings are stacked on top of each other, heavier structures of irregular carbons are formed, and therefore the density increases [41].

3.3 FE-SEM Analysis

Scanning electron microscopy studies were conducted to examine the surface properties and porosity development of activated carbons produced using different activation agents. In order to make an assessment, FE-SEM images (taken at a size of 10k) of commercial activated carbon and activated carbon produced with different agents were used. When the FE-SEM images of commercial active (O) carbon in Figure 3a are examined, it is observed that it has a heterogeneous cavity structure and small-sized pits surrounding these cavities.

Table 1. Densities of activated carbons

Activated carbons	Density(g/cm^3)
O	2.14
WPS	1.82
WPA	1.65

When the FE-SEM images of WPA-coded activated carbon produced by chemical activation of waste paper with phosphoric acid are examined in Figure 3b, it is observed that pores that are in different sizes and like ellipse shape are lined up on the outer surface of the activated carbon which is not entirely round. When carefully examined, Figure 3b evokes a honeycomb. When compared with commercial activated carbon, it is seen that hierarchical-porous activated carbons with a high specific surface area are obtained. It is known that in studies where phosphoric acid is used as an activation agent at the stage of activated carbon production, the surface width distribution shows more heterogeneous characteristics compared to others [42]. For activated carbons, the pore structure, size, and distribution are important for characterizing the heterogeneity of materials. The heterogeneity characteristic is closely related to the balanced distributions of a rigid internal structure model and gives important clues about the used material [43]. It is possible to say that these pores are useful for any adsorption process because the large-sized pores serve as feeder pores to the lower-sized meso and micropores [44]. In many studies, it has been stated that activation temperature, pressure, and duration are important. It is emphasized that the specified parameters affect the pore volume, product efficiency, and surface volume of activated carbon, and the appropriate temperature is 600 °C [45,46].

When the FE-SEM images of WPS-coded activated carbon produced as a result of the chemical activation of zinc chloride (ZnCl$_2$) activation agent with waste paper are examined (Figure 3c), it is seen that there are irregular cavities and large and small amorphous pores on the outer surface of the activated carbon. Compared to commercial activated carbon, it is seen in Figure 3c that the pore width is deeper and has a cavity structure. Some studies in the literature have also revealed that the production of activated carbon with agricultural waste material and ZnCl2 activation agent increases the pore width [47]. ZnCl2 were used as an activation agent, the pores expanded since outward expansion and decomposition occurred on the activated carbon surface over time [48]. In another study, Gonzalez-Serrano et al. reported that they obtained a large surface area in the production of activated carbon from the chemical activation of Kraft lignin with zinc chloride, and they noted that the activated carbons produced were usually microporous [49]. Recently, activated carbons with a good pore volume and the desired surface area have been produced from many agricultural wastes and lignocellulosic materials. Experimental studies have shown that similar situations occur in terms of pore and surface area in the production of activated carbon from waste paper, and the use of zinc chloride as an activation

agent has an effect on the activation process of waste paper.

3.4 EDS Analysis

Within the scope of the study, the activated carbons obtained as a result of treatment of waste paper with H_3PO_4 and $ZnCl_2$ activation agents and commercially purchased activated carbon were compared, and in order to make characterization, elemental analysis and distributions of activated carbons were studied. Figure 4 shows the Mapping and EDS analyses.
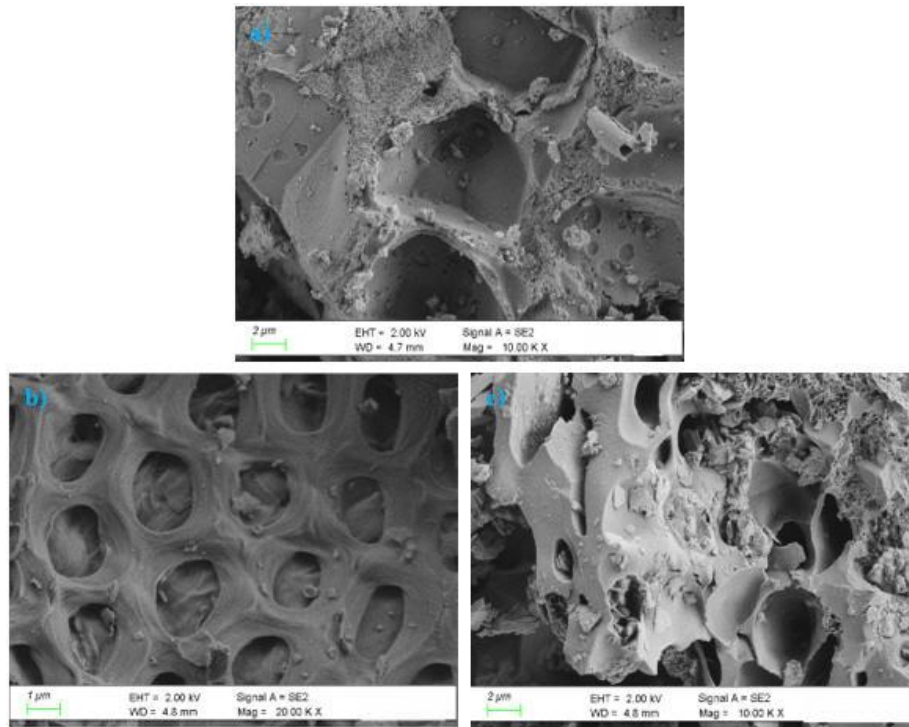
Figure 3. FE-SEM images of (a) Commercial activated carbon, (b) WPA and (c) WPS activated carbons
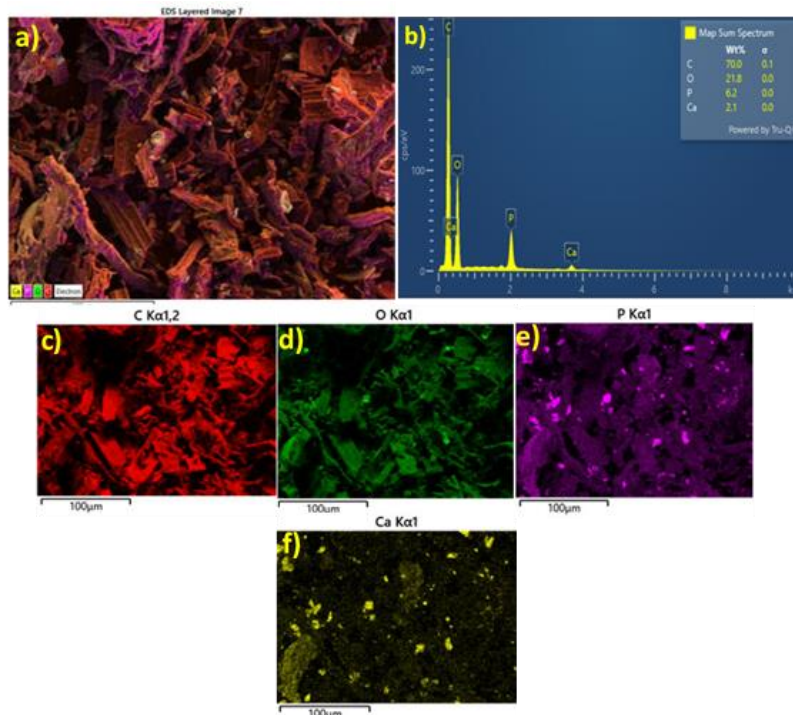
Figure 4. FE-SEM Mapping and EDS analyses of commercial activated carbon

The results of EDS elemental analysis performed on commercial activated carbon samples (Figure 4b) showed that the activated carbon produced from coconut shell included 72.5 wt% carbon concentration (C), 18.1% oxygen (O), 5.4% Silicon (Si), and 1.8% aluminum (Al). The distributions of the elements are observed in the FE-SEM Mapping images. In addition, it was found that there was 2.2% iron (Fe) element in commercial activated carbon, and this element was not homogeneously distributed as seen in FE-SEM images and Mapping elemental analyses (Figure 4g). In the study conducted by Mirshafiee et al., based on EDS analysis, it was reported that 73% C and 25% O were found in activated carbon produced from coconut shells. In addition, in the same study, it was found that elements, except for the Fe element, were distributed homogeneously in SEM-Mapping images [50]. On the other hand, it has been stated that Si and Al, found in commercial activated carbon, are also found in the stem and fruit peels of tropical tree species such as coconut [51].Figure 5 shows the EDS and Mapping analysis results of activated carbon

produced from waste paper by using phosphoric acid (H_3PO_4) activation agent.

As seen in Figure 5a and 5b, it was observed that carbon (C) (70%), oxygen (O) (21.8%), Phosphorus (P), and Calcium (Ca) elements were present respectively in the activated carbon produced by phosphoric acid activation. On the other hand, the homogeneous distribution of elements C, O, and P in the material is seen in Figure 5c, Figure 5d, and Figure 5e, respectively. In the literature, in the EDS analysis of the activated carbon produced from eucalyptus waste [52] and kraft lignin [53] by using phosphoric acid activation agents, 75% - 82 C, and 11% - 20 O, and 3-7% P element were identified. In the current study, FE-SEM images and Mapping analyses also showed a homogeneous distribution of all elements on the surface of activated carbon. In addition, the presence of Ca element in the activated carbon produced within the scope of the study (Figure 5f) was due to the use of calcium carbonate as a filler during paper production [54].
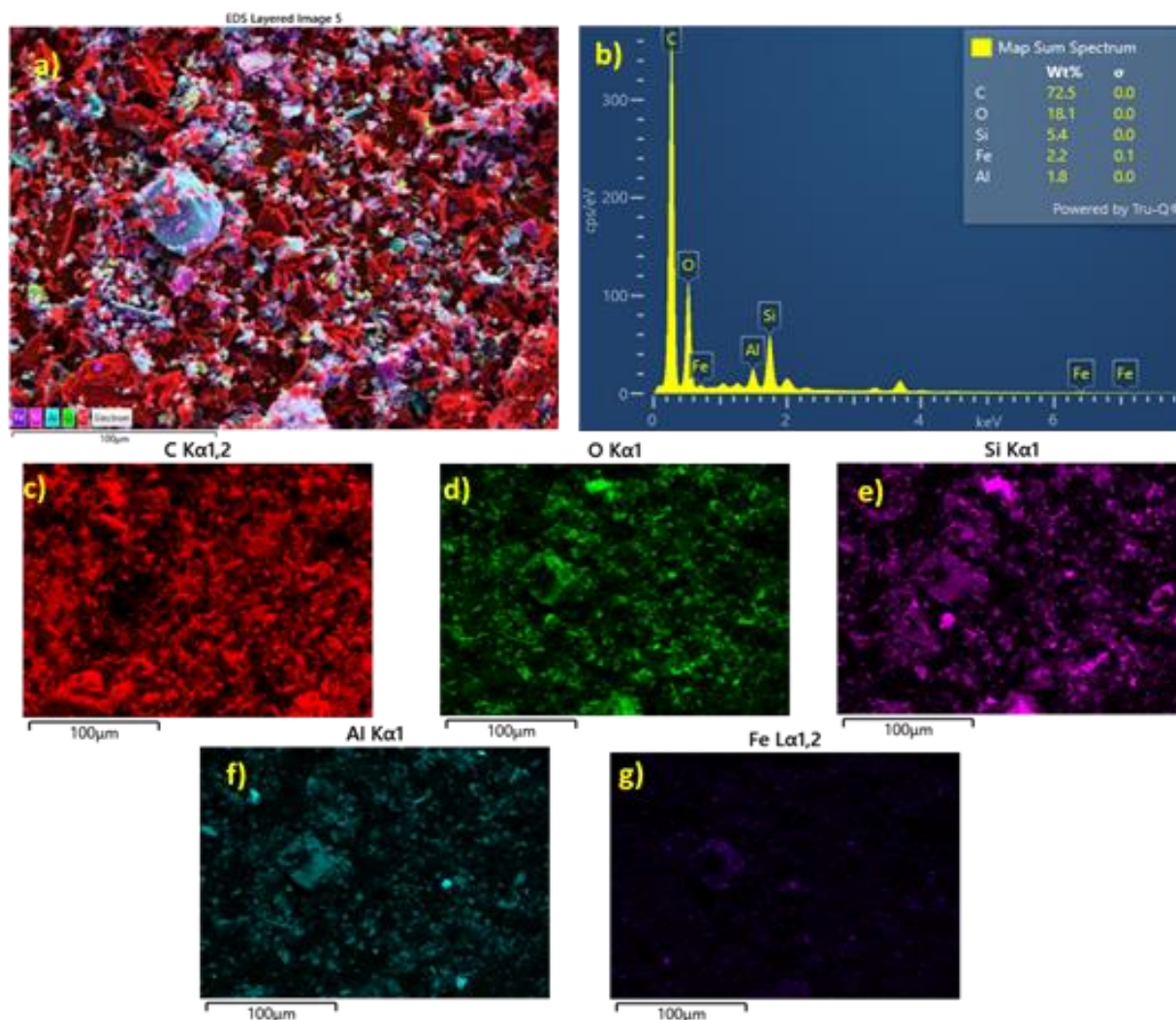
Figure 5. FE-SEM Mapping and EDS analyses of the activated carbon produced from waste paper by using phosphoric acid (H_3PO_4) activation agent

In the study conducted by Manandhar et al., EDS analysis determined that the Ca element was found in the activated carbon at a rate of 2.91% [55]. Because calcium carbonate is resistant to high temperatures [56], the presence of 2.1% Ca element in the activated carbon produced in the current study shows that it is consistent with the literature.

Figure 6 shows the EDS and Mapping analyses of activated carbon produced from waste paper using zinc chloride ($ZnCl_2$) as an activation agent.

As seen in Figures 6a and 6b, in activated carbon produced from waste paper by using zinc chloride as an activation agent, 65% carbon (C), 15.6% zinc (Zn), 12.8% oxygen (O), 5.5% chlorine (Cl), and 1.2% calcium (Ca) elements were detected. The FE-SEM images and Mapping elemental analyses revealed that all elements, except for the Ca element, were distributed homogeneously in the produced activated carbon (Figure 6g). It has been stated that 72.11% C and 22.06% O were found in office waste papers [55]. It has been claimed that the decrease in the element O, especially after the production of activated carbon, is due to the removal of the element O from the environment under high temperatures [57]. A study stated that there was O element at a rate of 6.62% in activated carbon produced from waste paper at a temperature of 850°C by using $ZnCl_2$ as an activation agent [58].

In addition, it is seen in Figures 6d and 6f that there are Zn and Cl elements in the environment due to the $ZnCl_2$ activation agent used. In the literature, it has been observed that activated carbons produced from different raw materials by using the $ZnCl_2$ activation agent have similar results [59,60]. In their study, using FE-SEM images and Mapping elemental analysis, Fardim and Holmbom showed that the element Ca was distributed heterogeneously in paper [61]. Also, another study found that the element Ca deteriorates at a temperature of 710-720 °C [62].
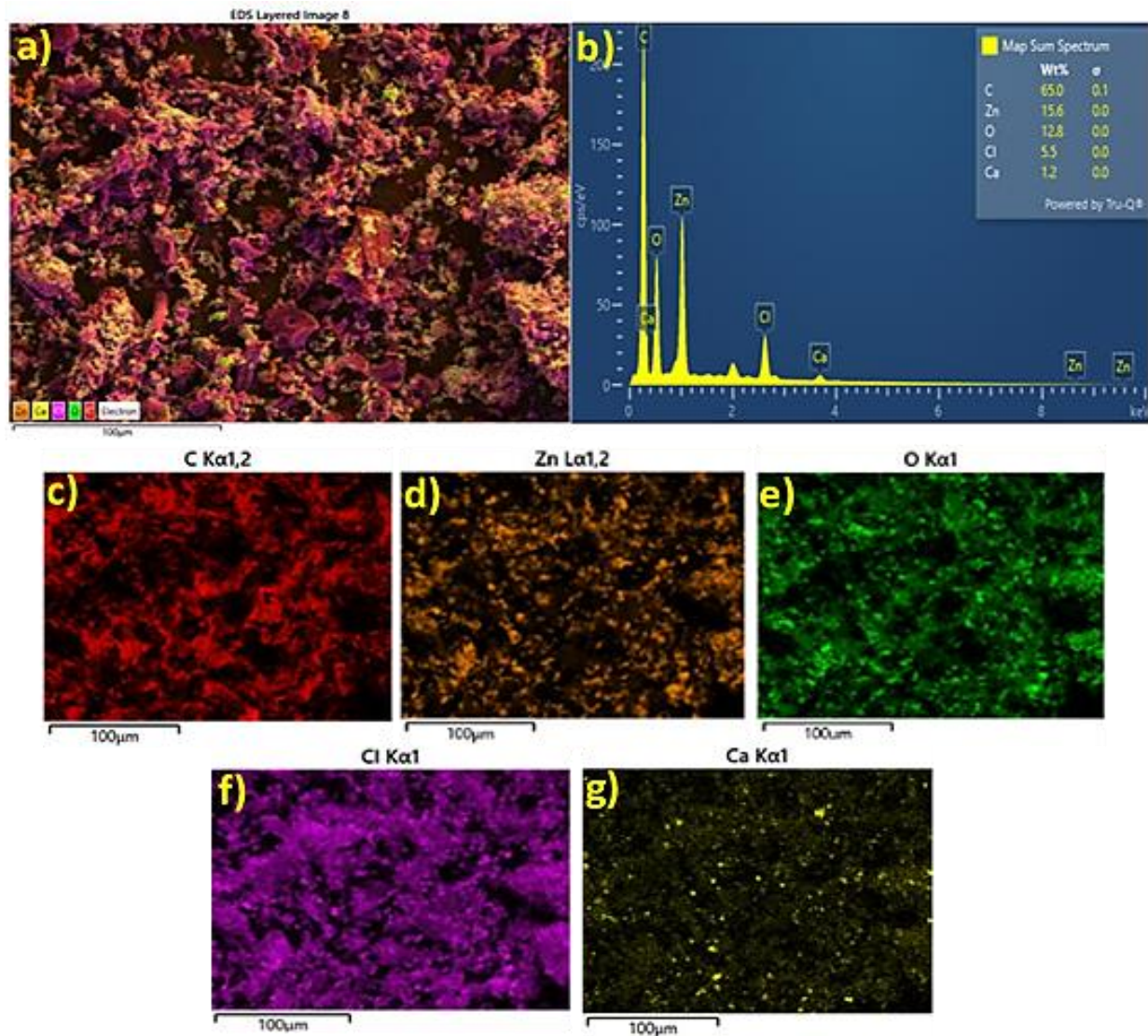

Figure 6. FE-SEM Mapping and EDS analyses of activated carbon produced from waste paper by using zinc chloride ($ZnCl_2$) as activation agent

4. Conclusion

Recycling waste paper is an important contribution to protecting the environment and increasing the diversity of raw materials used, particularly in the paper industry. However, In Turkey, the rate of recycling waste paper is low because the waste paper often contains impurities and unwanted materials, which make it more difficult and costly to recycle. Moreover, high-cost facilities are required for recycling waste paper. Therefore, it is necessary to evaluate waste paper in different areas like activated carbon production. In this study, activated carbon produced from waste paper was successfully produced with chemical activation agents ($ZnCl_2$ and H_3PO_4). The porous structures of the activated carbons produced in the FE-SEM images were determined. Activated carbons produced with phosphoric acid were found to have low density due to higher oxygen content as a result of EDS analysis. In the Mapping analyses of the activated carbons (WPA and WPS) produced within the scope of the study, Ca elements were found at rates of 2.1% and 1.2%, respectively. The use of calcium carbonate as a filler during paper production explains the presence of the Ca element. When the commercial activated carbon was compared with WPS and WPA activated carbons, it was seen that successful results were obtained in terms of pore size, distribution, and other analyzes of the produced activated carbons. Based on the results of the study, it can be concluded that the production of activated carbon from waste paper will be a good source of recycling for sustainability as well as an important material for the national economy.

Declaration

The author(s) declared no potential conflicts of interest with respect to the research, authorship, and/or publication of this article. The author(s) also declared that this article is original, was prepared in accordance with international publication and research ethics, and ethical committee permission or any special permission is not required.

Author Contributions

M.E. Ergun and D. Özdemir developed the methodology. S. Bulbul performed the analysis. D.Özdemir, S. Bulbul and M. E. Ergun wrote the manuscript and proofread the manuscript together.

References

1   Tan, X., S. Liu ,Y. Liu , Y.Gu, G. Zeng , X. Hu, et al. ,*Biochar as potential sustainable precursors for activated carbon production: Multiple applications in environmental protection and energy storage*. Bioresource Technology, 2017.**227**: p. 359–72.

2   Ruiz, B., N. Ferrera-Lorenzo, E. Fuente, *Valorisation of lignocellulosic wastes from the candied chestnut industry Sustainable activated carbons for environmental applications*. Journal of Environmental Chemical Engineering, 2017. **5**(2): p.1504–15.

3   de Souza, L.K.C., A.A.S. Gonçalves, L.S. Queiroz ,J.S Chaar, G.N. da Rocha Filho, C.E.F. da Costa,*Utilization of acai stone biomass for the sustainable production of nanoporous carbon for CO2 capture*. Sustainable Materials and Technologies, 2020. **25**: p. e00168.

4   Ukanwa K.S., K. Patchigolla, R.Sakrabani, E. Anthony, S. Mandavgane, *A Review of Chemicals to Produce Activated Carbon from Agricultural Waste Biomass*. Sustainability, 2019. **11**(22): p. 6204.

5   Bhatnagar, A., W. Hogland, M. Marques , M.Sillanpää, *An overview of the modification methods of activated carbon for its water treatment applications*. Chemical Engineering Journal, 2013. **219**: p. 499–511.

6   Ergün, M.E., S. Bulbul , *Production and characterization of activated carbon from Black Poplar (Populus Nigra) wood waste with different chemical activation methods*. International Advanced Researches and Engineering Journal, 2022 . **6**(3): p.167–75.

7   Gao, Y., Q. Yue, B. Gao, A.Li, *Insight into activated carbon from different kinds of chemical activating agents: A review*. Science of The Total Environment, 2020 .**746**: p.141094.

8   Hoang, A.T., S. Kumar, E.Lichtfouse, C.K. Cheng, Varma RS, Senthilkumar N, et al.,*Remediation of heavy metal polluted waters using activated carbon from lignocellulosic biomass:An update of recent trends*. Chemosphere, 2022. **302**: p.134825.

9   Sevilla, M., N. Díez, A.B., Fuertes, *More Sustainable Chemical Activation Strategies for the Production of Porous Carbons*. ChemSusChem,2021.**14**(1): p.94–117.

10   Hayashi, J., T. Horikawa, I. Takeda, K. Muroyama & F.A. Ani, *Preparing activated carbon from various nutshells by chemical activation with K2CO3*. Carbon, 2002.**40**: p.2381–6.

11   Yacob, A.R , H.M.Al Swaidan, *Phosphoric Acid Effect on Prepared Activated Carbon from Saudi Arabia's Date Frond Waste*. Applied Mechanics and Materials, 2012.(**110–116**): p.2124–30.

12   Ahmad, A., H.M. Al-Swaidan, A.H. Alghamdi ,*Production of Activated Carbon from Raw Date Palm Fronds by ZnCl2 Activation*. Journal of the Chemical Society of Pakistan, 2015. **37**(6): p.1081–7.

13   Jawaduddin, M., S. Memon, N. Sabzoi, M. Mujawar, S. Qureshi , *Synthesis of activated carbon via sulphuric acid and iron chloride and its potential application synthetic grey water in combination with sand bed filter*. Eurasian Journal of Analytical Chemistry,2018.**13**: p.83–94.

14   Danish, M., T. Ahmad ,*A review on utilization of wood biomass as a sustainable precursor for activated carbon production and application*. Renewable and Sustainable Energy Reviews, 2018. p.871–21.

15   Gao, Y., Q. Yue , B.Gao, Y. Sun, W.Wang, Q. Li, et al., *Comparisons of porous, surface chemistry and adsorption properties of carbon derived from Enteromorpha prolifera activated by H4P2O7 and KOH*. Chemical Engineering Journal, 2013.**232**: p.582–90.

16   Moussavi, G., A. Alahabadi , K.Yaghmaeian , M. Eskandari , *Preparation, characterization and adsorption potential of the NH4Cl-induced activated carbon for the*

removal of amoxicillin antibiotic from water. Chemical Engineering Journal, 2013. **217**: p.119–28.

17 Hussaro, K., *Preparation of Activated Carbon From Palm Oil Shell By Chemical Activation Na2CO3 And ZnCl2 As Imprenated For H2S Adsorptıon*. American Journal of Environmental Sciences,2014.**10**(4): p.336–46.

18 Dzigbor, A., A. Chimphango , *Production and optimization of NaCl-activated carbon from mango seed using response surface methodology*. Biomass Conv Bioref,2019. **9**(2): p.421–31.

19 Ncibi, M.C., R.Ranguin ,M.J Pintor,V.Jeanne-Rose, M.Sillanpää, S. Gaspard , *Preparation and characterization of chemically activated carbons derived from Mediterranean Posidonia oceanica (L.) fibres.* Journal of Analytical and Applied Pyrolysis, 2014.**109**: p.205–14.

20 González-García, P.,Activated carbon from lignocellulosics precursors: *A review of the synthesis methods, characterization techniques and applications.* Renewable and Sustainable Energy Reviews, 2018 .**82**: p.1393–414.

21 Wang, J.,S.Kaskel, *KOH activation of carbon-based materials for energy storage*. J Mater Chem,2012.**22**(45): p.23710–25.

22 Rashidi, N.A., S. Yusup , *A review on recent technological advancement in the activated carbon production from oil palm wastes*. Chemical Engineering Journal, 2017 .**314**: p.277–90.

23 Zuo, S., J.Yang, J. Liu, X. Cai, *Significance of the carbonization of volatile pyrolytic products on the properties of activated carbons from phosphoric acid activation of lignocellulosic material*. Fuel Processing Technology,2009 .**90** (7): p. 994–1001.

24 Arami-Niya, A., W.M.A. Wan Daud, F.S. Mjalli, *Production of palm shell-based activated carbon with more homogeniouse pore size distribution*. Journal of Applied Sciences, 2010.**10**(24): p.3361–6.

25 Patnukao, P., P. Pavasant , *Activated carbon from Eucalyptus camaldulensis Dehn bark using phosphoric acid activation. Bioresource Technology*, 2008 .**99**(17): p.8540–3.

26 Xu, J., L.Chen , H.Qu ,Y. Jiao ,J. Xie ,G. Xing , *Preparation and characterization of activated carbon from reedy grass leaves by chemical activation with H3PO4*. Applied Surface Science,2014.**320**: p.674–80.

27 Usmani,T.H., A.T.Wahab, S.Z. Ahmed , A.H.K. Yousufzai, *Preparation and characterization of activated carbon from a low rank coal*. Carbon, 1996 .**34**(1): p.77–82.

28 Lu, Y., S. Zhang, J.Yin, C. Bai, J. Zhang , Y.Li et al, *Mesoporous activated carbon materials with ultrahigh mesopore volume and effective specific surface area for high performance supercapacitors*. Carbon, 2017.**124**: p.64–71.

29 Zhang, Y.J., Z.J. Xing, Z.K. Duan, Li. Meng, Y. Wang, *Effects of steam activation on the pore structure and surface chemistry of activated carbon derived from bamboo waste*. Applied Surface Science, 2014.**315**: p. 279–86.

30 Fernandez, M.E.,G.V.Nunell,P.R. Bonelli ,A.L. Cukierman , *Activated carbon developed from orange peels: Batch and dynamic competitive adsorption of basic dyes*. Industrial Crops and Products, 2014 .**62**: p.437–45.

31 Thongpat, W., J.Taweekun, K.Maliwan, *Synthesis and characterization of microporous activated carbon from*

rubberwood by chemical activation with KOH. Carbon Lett, 2021.**31**(5): p.1079–88.

32 Tran,K.N., A.J Berkovich, A. Tomsett, S.K. Bhatia, *Crystalline Structure Transformation of Carbon Anodes during Gasification*.Energy Fuels, 2008.**22**(3): p.1902–10.

33 El Nemr, A., R.M. Aboughaly, A. El Sikaily, S.Ragab, M.S. Masoud,Ramadan, *Microporous nano-activated carbon type I derived from orange peel and its application for Cr(VI) removal from aquatic environment*. Biomass Conv Bioref,2022 .**12**(11): p.5125–43.

34 Mohammed, J., N.S. Nasri , M.A. Ahmad Zaini , U.D. Hamza , F.N. Ani, *Adsorption of benzene and toluene onto KOH activated coconut shell based carbon treated with NH3*. International Biodeterioration & Biodegradation, 2015. **102**: p. 245–55.

35 Al Bahri, M., L.Calvo , M.A. Gilarranz ,J.J. Rodriguez , *Activated carbon from grape seeds upon chemical activation with phosphoric acid: Application to the adsorption of diuron from water*. Chemical Engineering Journal,2012.**203**: p. 348–56.

36 Stavrinou, A., C.A. Aggelopoulos ,C.D. Tsakiroglou , *Exploring the adsorption mechanisms of cationic and anionic dyes onto agricultural waste peels of banana, cucumber and potato: Adsorption kinetics and equilibrium isotherms as a tool*. Journal of Environmental Chemical Engineering,2018 .**6**(6): p.6958–70.

37 Sebeia, N., M. Jabli ,A. Ghith , Y.El. Ghoul , F.M .Alminderej , *Populus tremula, Nerium oleander and Pergularia tomentosa seed fibers as sources of cellulose and lignin for the bio-sorption of methylene blue*. International Journal of Biological Macromolecules, 2019.**121**: p. 655–65.

38 Nasab, S.G., A.Semnani , A.Teimouri , M.J. Yazd , T.M. Isfahani, Habibollahi S. , *Decolorization of crystal violet from aqueous solutions by a novel adsorbent chitosan/nanodiopside using response surface methodology and artificial neural network-genetic algorithm*. International Journal of Biological Macromolecules,2019 .**124**: p.429–43.

39 Örkün Y. *Fındık Kabuğundan Fiziksel ve Kimyasal Aktivasyonla Aktif Karbon Üretilmesi ve Karakterizasyonu,Enerji2011,*İstanbul Teknik Üniversitesi: Turkey. p. 106.

40 Li, L., P.A. Quinlivan ,D.R.U. Knappe, *Effects of activated carbon surface chemistry and pore structure on the adsorption of organic contaminants from aqueous solution*. Carbon,2002 .**40**(12): p.2085–100.

41 Prauchner, M.J., V.M.D. Pasa , N.D.S. Molhallem ,C. Otani , S.Otani , L.C.Pardini ,*Structural evolution of Eucalyptus tar pitch-based carbons during carbonization*. Biomass and Bioenergy, 2005 .**28**(1): p. 53–61.

42 Molina-Sabio, M., F.Rodríguez-Reinoso , *Role of chemical activation in the development of carbon porosity*. Colloids and Surfaces A: Physicochemical and Engineering Aspects, 2004.**241**(1): p.15–25.

43 Wibowo, N., L. Setyadhi , D.Wibowo , J.Setiawan , S.Ismadji , *Adsorption of benzene and toluene from aqueous solutions onto activated carbon and its acid and heat treated forms: Influence of surface chemistry on adsorption*. Journal of Hazardous Materials, 2007 .**146**(1): p.237–42.

44 Zabaniotou, A., G. Stavropoulos,V. Skoulou, *Activated carbon from olive kernels in a two-stage process: Industrial improvement*. Bioresource Technology,2008 .**99**(2): p.320–6.

45 Fierro, V., V.Torné-Fernández , A. Celzard, *Kraft lignin as a precursor for microporous activated carbons prepared by impregnation with ortho-phosphoric acid: Synthesis and textural characterisation.* Microporous and Mesoporous Materials,2006 .**92**(1): p. 243–50.

46 Haimour, N.M., S .Emeish, *Utilization of date stones for production of activated carbon using phosphoric acid. Waste Management,* 2006 .**26**(6): p. 651–60.

47 Dural, M.U., L. Cavas ,S.K. Papageorgiou,F.K. Katsaros, *Methylene blue adsorption on activated carbon prepared from Posidonia oceanica (L.) dead leaves: Kinetics and equilibrium studies.* Chemical Engineering Journal, 2011.**168**(1): p.77–85.

48 Joshi, S., R.G. Shrestha, R.R. Pradhananga, K. Ariga, L.K.Shrestha , *High Surface Area Nanoporous Activated Carbons Materials from Areca catechu Nut with Excellent Iodine and Methylene Blue Adsorption*. C, 2022 .**8**(1): p.2.

49 Yang, T., A.C. Lua , *Textural and chemical properties of zinc chloride activated carbons prepared from pistachio-nut shells.*Materials Chemistry and Physics, 2006.**100**(2): p.438–44.

50 Mirshafiee, S., A. Salamatmanesh, A. Heydari, *Magnetic Coconut Shell-Derived Activated Carbon Adorned with Cu2O Nanoparticles: A Green and Efficient Porous Catalyst for N-Arylation of Hetero-Aromatics in Eutectic Medium.* ChemistrySelect,2022.**7**(29): p.e202200454.

51 Epstein, E., Silicon. *Annual Review of Plant Physiology and Plant Molecular Biology*,1999.**50**(1): p.641–64.

52 Lu, Z., H. Zhang ,A. Shahab ,K. Zhang , H.Zeng , A.U.R. Bacha et al., *Comparative study on characterization and adsorption properties of phosphoric acid activated biochar and nitrogen-containing modified biochar employing Eucalyptus as a precursor.* Journal of Cleaner Production, 2021.**303**: p.127046.

53 Brazil, T.R., M.Gonçalves, M.S.O. Junior ,M.C. Rezende ,*Sustainable process to produce activated carbon from Kraft lignin impregnated with H3PO4 using microwave pyrolysis.* Biomass and Bioenergy,2022. **156**: p.106333.

54 Jung, J.K., Y.B. Seo, *Development of hybrid calcium carbonate for high loading paper (II)-Comparison with GCC.* Journal of Korea Technical Association of The Pulp and Paper Industry, 2015.**47**(4): p.76–80.

55 Manandhar, S., B. Shrestha, F.Sciortino , K. Ariga , L.K.Shrestha,*Recycling Waste Paper for Further Implementation: XRD, FTIR, SEM, and EDS Studies. Journal of Oleo Science,*2022.**71**(4): p. 619–26.

56 Karlsson,L.,A.Lundgren,J. Jungqvist,T. Hjertberg,*Influence of melt behaviour on the flame retardant properties of ethylene copolymers modified with calcium carbonate and silicone elastomer*. Polymer Degradation and Stability, 2009. **94**(4): p.527–32.

57 Ooi,C.H.,C.L. Ang , F.Y. Yeoh , *The Properties of Activated Carbon Fiber Derived from Direct Activation from Oil Palm Empty Fruit Bunch Fiber.* Advanced Materials Research, 2013. **686**: p. 109–17.

58 Tang, X., G.Ran , J. Li , Z. Zhang ,C. Xiang, *Extremely efficient and rapidly adsorb methylene blue using porous adsorbent prepared from waste paper: Kinetics and equilibrium studies.* Journal of Hazardous Materials, 2021.**402**: p.123579.

59 Bai, X.,B. Quan , C. Kang , X.Zhang , Y.Zheng ,J. Song et al, *Activated carbon from tea residue as efficient absorbents for environmental pollutant removal from wastewater.* Biomass Conv Bioref, 2022.

60 Zhang, G., H.Yang, M. Jiang , Q. Zhang,*Preparation and characterization of activated carbon derived from deashing coal slime with ZnCl2 activation*. Colloids and Surfaces A: Physicochemical and Engineering Aspects,2022. **641**:p. 128124.

61 Fardim, P., B.Holmbom, *ToF-SIMS imaging: a valuable chemical microscopy technique for paper and paper coatings*. Applied Surface Science, 2005.**249**(1):p.393–407.

62 Princi, E., S.Vicini ,E. Marsano ,V. Trefiletti , *Influence of the artificial weathering on thermal stability of paper-based materials.* Thermochimica Acta, 2008.**468**(1): p. 27–34.

Research Article

Early stage diabetes prediction using decision tree-based ensemble learning model

Ozge Sen Kaya [a] iD, *Sinem Bozkurt Keser* [b,*] iD *and Kemal Keskin* [b] iD

[a]*Eskişehir Osmangazi University, Faculty of Engineering, Department of Computer Engineering, 26040, Eskişehir/Turkey*
[b]*Eskişehir Osmangazi University, Faculty of Engineering, Department of Electrical and Electronics Engineering, 26040, Eskişehir/Turkey*

ARTICLE INFO

ABSTRACT

Diabetes is a lifelong disease that has undesirable effects on various organs, such as long-term organ damage, functional disorder, and finally failure of the organ. Diabetes must be treated under the supervision of a doctor. Diabetes is known as a disease that can be seen in many people today and is becoming widespread due to life conditions. If a person with diabetes does not receive any treatment at an early stage, the patient's body can react with serious complications. In addition to the medical methods used in the diagnosis of diabetes, this disease can be detected by an artificial intelligence approach. This research aims to establish the most influential variable among the many variables causing diabetes and to design a model that will predict diabetes to help doctors analyze the disease with selected machine learning methods. In this study, Decision Tree, Bagging with Decision Tree, Random Forest and Extra Tree algorithms were used for the proposed model and the highest accuracy values were obtained with the Extra Trees algorithm with 99.2%.

1. Introduction

Diabetes mellitus refers to a metabolic disease reasoned by persistent hyperglycaemia. Deficiency of insulin secretion or irregularities in insulin activity or both of them is the primary basis for the hyperglycaemia [1]. Chronic diabetes mellitus (DM) constitutes undesirable effects on various organs such as long-term organ damage, function disorder, and finally failure of the organ. Specifically, eyes, nerves, heart, kidneys, and blood vessels are the most affected ones [2]. DM can be classified into three main aetiological types: type 1, type 2, and other specific types. These types differ from each other considering defects, disorders, or processes along with diabetes mellitus. The pancreas contains β-cells, which produce and release insulin in response to blood glucose levels. Type 1 diabetes, namely, insulin-dependent diabetes, arise from autoimmune extermination of the β-cells of the pancreas. The rate of disruption of β-cells is quite variable according to age, sex, genetic factors, lifestyle and diet, such that it proceeds faster in some people (primarily children), and sluggish in others (especially adults). In the latter phase of this type of diabetes, insufficient (almost negligible)

insulin is secreted. Patients need insulin therapy throughout their lifetime. Only 5-10 percent of diabetics have this form of diabetes. Type 2 diabetes involves people with insulin resistance and a lack of insulin production. Released Insulin is not enough to compensate for insulin resistance. However, the patients do not require insulin therapy to survive. This form of diabetes accounts for 90-95 percent of diabetics and has mostly been seen in obese people because obesity has a destructive effect on insulin levels. Increased neogenesis was the mechanism through which the relative volume of β-cells was higher in obese than lean nondiabetic individuals [2]. Other types of diabetes mellitus have rarely been seen when compared to type 1 and type 2 diabetes and occur under specific conditions such as genetic defects and pregnancy.

The number of diabetics worldwide has reached 422 million (approximately 8.5 percent of the world population) in 2014 and it has doubled since 1980 [3]. The research on the prevalence of diabetes mellitus for future projections shows that there will be 693 million people with diabetes by 2045 [4]. The growing rate of prevalence is really fast, especially in impoverished countries. When one considers that half of the diabetics are undiagnosed, it

becomes difficult to cope with the disease and the death rate is increased. Diagnosing diabetes in time with precision is of great importance. Therefore, it can prevent diabetes-related deaths, improve the quality of life, and reduces the economic burden caused by the disease. Machine learning is a research approach that focuses on providing computers with the ability to recognize complex patterns and extrapolate knowledge from. It has frequently been used in recent years to diagnose or help diagnose diseases. In the context of rapidly increasing diabetics, the classification of patients according to current groups will allow them to start treatment on time and will eliminate some of the problems caused by delays.

Machine learning is a powerful tool for predicting and diagnosing diabetes. It includes the analysis of big data sets, the identification of patterns, and the generation of predictions based on these patterns utilizing algorithms and statistical models. Machine learning can evaluate medical data associated with diabetes, such as blood glucose levels, blood pressure, and body mass index, to predict a person's risk of getting the disease. Compared to more traditional methods, it can offer accurate predictions. A large amount of data may be analyzed by machine learning algorithms, and these algorithms are capable of identifying small patterns. As a result, individuals may see better results from their diabetes treatment and diagnosis. Machine learning has gained importance in the health sector compared to other methods due to reasons such as easy to use and fast. Machine learning methods are used in disease diagnosis and in different studies by making use of data sets obtained in diseases. These studies have achieved some research of algorithm comparison and model establishing for DM prediction. The data validity and prediction accuracy, however, were not good enough for actual use. To increase accuracy, we must provide a novel prediction model. Therefore, we chose a dataset to test the usability and adaptation of our model. The main objectives of this study are to predict diabetes at an early stage so that patients may begin the right treatments on time, and to discover the correlations among the variables that contribute to diabetes. Finally, this research will help us to discover the best machine learning classifier to predict diabetes.

2. Related Works

Nowadays, the use of machine learning algorithms in medical diagnosis, including type 2 diabetes mellitus (T2DM), is rapidly increasing [1]. The process from expert medical diagnosis to evaluation and decision making is the key factor here [2]. Several classification algorithms are utilized to predict T2DM in the early stage. The compound of ant colony optimization (ACO) and fuzzy logic is proposed in [3] to diagnose diabetics by utilizing the public Pima Indian Diabetes Database (PIDD) which is existing at

the University of California, Irvine (UCI) machine learning repository. In the experiments, 84.24% classification accuracy is obtained with the proposed method. Karegowda et. al. [4] compare Neural Networks Back Propagation Networks (BPN), Genetic Algorithms (GA), and DT algorithms to diagnose T2DM. The proposed GA-correlation-based feature selection approach results with 84.71% accuracy in the experiments. The classification technique based on the Gaussian process (GP) has been adopted in linear, polynomial, and radial-based kernel [5]. The performance of the GP-based classification method is compared with LDA, QDA, and NB by utilizing PIDD in the experiments. 81.97% accuracy performance is obtained with the GP-based model which is larger compared to other methods. In [6], NB, SVM, Random Forest (RF), and Simple Classification and Regression Tree (CART) supervised learning algorithms are compared to recommend the best approach based on efficient performance results for the prediction of T2DM. Experimental results of each algorithm used on the PIDD demonstrate that SVM performed best in the prediction of diabetes disease having 79.13% accuracy. Three machine learning classification algorithms namely DT, SVM, and NB are used to construct a model [7]. The experiments are performed on PIDD to evaluate the performance of the algorithms. According to test results, NB outperforms other algorithms to prognosticate the likelihood of T2DM in patients with 76.30% accuracy. To construct an adaptive model with better accuracy, the k-means clustering algorithm is enhanced with Logistic Regression (LR) [8]. In the experiments, 95.42% accuracy is obtained with the proposed algorithm using 10-fold cross-validation. DT, RF, and Artificial Neural Network (ANN) are used to predict T2DM [9]. In the experiments, the dataset is including 14 attributes collected from the hospital in Luzhou, China during the physical examination. The attributes are 14 physical examination indexes such as age, pulse rate, breathe, left systolic pressure (LSP), right systolic pressure (RSP), left diastolic pressure (LDP), right diastolic pressure (RDP), height, weight, physique index, fasting glucose, waistline, low density lipoprotein (LDL), and high density lipoprotein (HDL). Principal Component Analysis (PCA) and minimum redundancy maximum relevance (mRMR) are utilized to decrease the dimension of the dataset. Five-fold cross-validation is used to evaluate the algorithms, and RF performs better with 80.84% accuracy. ANN, RF, and K-means clustering techniques are applied for the estimation of T2DM using PIDD. In experiments, the ANN algorithm outperforms the other models with an accuracy of 75.70%, and by using association rule mining, the results have shown that there is a powerful connection between BMI and glucose with diabetes [10]. Four machine learning classifiers (LR, MLP, SVM, and RF) are evaluated on a dataset including an aggregate of 5319 cases and 36,224 controls. The dataset contains a total of 116 attributes with 18 demographic, 12

medical, and 86 dental attributes of 40,519 patients. In the experiments, RF was superior to other predictive models providing overall accuracy (94.14%) [11]. Leverage F-Score Feature Selection and Fuzzy SVM are used to predict T2DM using PIDD [12]. The fuzzy SVM algorithm gives 89.02% promising accuracy for predicting patients with T2DM. Juliet and Bhavadharani have been discussed the role of Naïve Bayes (NB), Decision Tree (DT), K-Star, LR, Support Vector Machine (SVM) methods for classifying Type 2 Diabetes Mellitus by using PIDD [13]. In the experiments, Logistic Regression provides the best accuracy with 77.73%. The missing values and class imbalance problems of PIDD are handled with NB, and the Adaptive synthetic sampling method (ADASYN), respectively. Then, an RF algorithm is performed to diagnose T2DM. In the experiments, RF outperforms NB, SVM, and DT with 87.10% accuracy using 10-fold cross-validation [14]. In [15], K-Nearest Neighbor (KNN) algorithm is developed by removing noise, decreasing the dimension, and weighting distance with k-means clustering (KMC), principal component analysis

(PCA), and autoencoder (AE), respectively. In the experiments, KMC improves the accuracy of KNN from 81.6% to 86.7%, combining KMC and PCA improves the KNN accuracy to be 90.9%, combining KMC and AE enhances the KNN to gives an accuracy of 97.8%, KMC, PCA, and Weighted KNN (WKNN) increases the accuracy to be 94.5%, and finally, the combination of KMC, AE, and WKNN achieves the best accuracy of 98.3%. Since the attributes in PIDD have a high non-linearity; AE gives higher accuracies than PCA. LR, KNN, DT, RF, SVM, NB, ANN, and Gradient Boosting (GB) are compared using clinical data obtained from the Dryad Digital Repository [16]. The clinical data contains age, gender, body mass index (BMI), systolic blood pressure (SBP), diastolic blood pressure (DBP), smoking and drinking status, family history of diabetes, alanine aminotransferase (ALT), fasting plasma glucose (FPG), total cholesterol (TC), low density lipoprotein (LDL), high density lipoprotein cholesterol (HDL-C), triglyceride (TG), year of follow up. GB outperforms other algorithms with 95.50% accuracy.

Table 1. A summary of research work for diagnoses of T2DM using machine learning algorithms (NA: Not Available)

Authors	Methodology	Dataset	Tool	Best Results
Ganji and Abadeh, 2011[3]	ACO and fuzzy logic	PIDD	Weka 3	84.24% accuracy
Karegowda et. al., 2011 [4]	GA-correlation based feature selection	PIDD	Python	84.71% accuracy
Maniruzzaman et. al., 2017 [5]	GP-based classification	PIDD	NA	81.97% accuracy
Mir et. al., 2018 [6]	NB, SVM, RF, and Simple CART	PIDD	Weka 3.82	79.13% accuracy with SVM
Sisodia et. al., 2018[7]	DT, SVM, and NB	PIDD	Weka	76.30% accuracy with NB
Wu et. al., 2018 [8]	K-means clustering algorithm is enhanced with LR	PIDD	Weka	95.42% accuracy
Zou et. al., 2018 [9]	DT, RF, and ANN	Dataset is including 14 attributes collected from the hospital in Luzhou, China	Weka, Java, Matlab	80.84% accuracy with RF
Alam et. al., 2019 [10]	ANN, RF, and K-means clustering	PIDD	NA	75.70% accuracy with ANN
Hegde et. al., 2019 [11]	LR, MLP, SVM, and RF	Dataset is retrieved from Marshfield Clinic Health System's data-warehouse	Weka	94.14% accuracy with RF
Lukmanto et. al., 2019 [12]	Fuzzy SVM	PIDD	NA	89.02% accuracy
Juliet and Bhavadharani, 2019 [13]	NB, DT, K-Star, LR, SVM	PIDD	NA	77.73% accuracy with LR
Wang et. al., 2019 [14]	NB, ADASYN, RF, DMP_MI	PIDD	Python	87.10% accuracy
Khairunnisa et. al., 2020 [15]	KMC, PCA, WKNN, AE	PIDD	NA	98.3% accuracy
Tarokh and Darabi, 2020 [16]	LR,NN,DT,RF,SVM,NB,GB	The dataset is retrieved from 32 health care centers in 11 provinces in China	Python	95.50% accuracy with GB
Gupta et.al.,2020 [17]	MLP, GP, LDA, QDA, SGD, RRC, SVM, KNN, DT, NB, LR, RF, ELM, RBF	PIDD, DCA	NA	94.59% accuracy for DCA, and 79.22% for PIDD

For the diagnosis of T2DM, two real-world datasets diabetic clinical dataset (DCA) and PIDD are evaluated by using 15 different classifiers (MLP, GP, Linear Discriminant Analysis (LDA), Quadratic Discriminant Analysis (QDA), Statistical Gradient Descent (SGD), Ridge Regression Classifier (RRC), SVM, KNN, DT, NB, LR, RF, and Extreme Learning Machine (ELM) for multiquadric, Radial Basis Function (RBF), sigmoid activation function with 10-fold cross-validation [17]. The DCA dataset is collected from a medical expert in the Indian state of Assam between 2017 and 2018. The experimental results show that LR yields better than other techniques (94.59% accuracy for DCA, and 79.22% for PIDD). Table includes several machine learning algorithms that different researchers have used to make comparisons along with dataset, tool, and outcome.

Ensemble learning (EL) algorithms are applied to improve the performance of the classification algorithm and solve the problems of unstable classification. The aim of the EL is to aggregate multiple versions of base classifiers to construct the final prediction. In the field of medical diagnosis, various studies are published to enhance the performance of the prediction model by using EL algorithms. NB, KNN, and DT are utilized with EL algorithms such as bagging and boosting to predict T2DM patients using 10-fold cross-validation [18]. In the experiments, the dataset is collected from 27 Primary Care Units (PCU) in Sawanpracharak Regional Hospital between 2011 and 2013. The dataset contains a total of 48,763 instances with 20,743 diabetes and 28,020 non-diabetes, and 15 input attributes and 1 output attribute. 95.31% accuracy is obtained from bagging with a DT classifier that is superior to other algorithms. To improve the performance of the classification algorithm, voting with KNN, SVM, LR, and stacking with RF, AdaBoost (AB), LR are applied using PIDD [19]. Best accuracy results are obtained as 80.08% with stacking in the experiments. The results show that ensemble classifier models performed better than the basic classifiers alone. The ensembling of two boosting classifiers such as AB and XB gives the best combination for predicting T2DM [20]. By using PIDD, 95.00% Area Under Curve (AUC) values were obtained that are better than other algorithms in the experiments. Besides, it is proven that by applying preprocessing steps such as outlier rejection filling missing values the quality of the PIDD can be improved. LR regularised generalized linear model (Glmnet) with Least Absolute Shrinkage and Selection Operator (Lasso) regression (L1), Random Forests (RF), eXtreme Gradient Boosting (XGBoost) with tree booster using regression tree as a base classifier and Light Gradient Boosting Machine (LightGBM) with L1 loss regression are evaluated in early prediction of T2DM [21]. It is found that LightGBM results in much more stable results compared to other algorithms. In a study, an EL algorithm with base classifiers Linear Discriminant Analysis (LDA), SVM, and RF is applied on National Health and Nutrition Examination Survey (NHANES) database to predict T2DM patients. In the experiments, NHANES database including 8057 instances and 12 attributes, 74.50% best accuracy is obtained with EL algorithm with LDA. Several ensemble learning techniques have been proposed in the literature for the diagnosis of T2DM summarized in Table 2.

3. Methodology

The flow chart of the proposed approach is shown in Figure 1. The initial step in the proposed approach is to gather publicly available data sets on diabetic symptoms. In the second stage, the data preprocessing is performed. Furthermore, in the third stage, data is split into training dataset (80%) and test dataset (20%). The training dataset is utilized to train the models (Decision Tree (DT), Bagging with Decision Tree, Random Forest (RF), and Extra Trees) and testing dataset is used to test the models in terms of various performance metrics (accuracy, precision, recall, and F1 score,). After comparing the models in terms of accuracy, the efficient model with the highest accuracy for the diagnose of the diabetes is determined. Finally, the outcomes of the patients are predicted according to this model.

3.1 Dataset

The dataset used in this study is utilized to predict early diabetes mellitus from the open-source machine learning repository UCI. The dataset was obtained by questionnaire from 520 patients at Sylhet Diabetes Hospital in Sylhet, Bangladesh, and were confirmed by doctors. Dataset consists of 17 features such as Age, Sex, Polyuria, Polydipsia, Sudden Weight Loss, Weakness, Polyphagia, Genital Thrush, Visual Blurring, Itching, Irritability, Delayed Healing, Partial Paresis, Muscle Stiffness, Alopecia, Obesity, and Class. These features are shown in detail in Table 3.

In this dataset, the first parameter is the age parameter as seen in the Table 3. The diabetes prevalence worldwide has increased from %4.7 to %8.5 of the population [22]. According to the IDF Diabetes Atlas estimates, 1 in 11 adults has diabetes in 2015. These adults are 16 years of age and above 16 years of age. The second parameter is sex. Studies show that middle-aged men have a higher prevalence of diabetes than women of similar age, and conversely, the prevalence is higher in older women than men. Other parameters are important parameters in the diagnosis of diabetes: polyuria, excessive urination; polydipsia, excessive thirst; sudden weight loss, weakness, polyphagia which is associated with hunger, genital thrush, visual blurring, itching, irritability, delayed healing, partial paresis or muscular stiffness, alopecia which is point baldness due to hair loss, obesity which is excessive or abnormal fat mass which results to health risks.

Table 2. A summary of research work for diagnoses of T2DM using ensemble learning algorithms (NA: Not Available)

| Authors	Methodology	Dataset	Tool	Best Results
Nai-arun et. al.,2014 [18]	NB, KNN, DT, Bagging and boosting	Dataset is collected from 27 Primary Care Units (PCU) in Sawanpracharak Regional Hospital during 2011-2013	NA	%95.31 accuracy with bagging and base classifier DT
Patil et. al., 2019 [19]	KNN, SVM, LR, RF, AB, LR	PIDD	Python	80.08% accuracy
Hasan et. al., 2020 [20]	KNN, DT, RF, AB, NB, XB	PIDD	Python	95.00 % AUC
Kopitar et. al., 2020 [21]	LR,RF,XGBoost, LightGBM	The dataset is collected from the NHANES database including 8057 instances and 12 attributes	NA	74.50% accuracy with EL algorithm with LDA
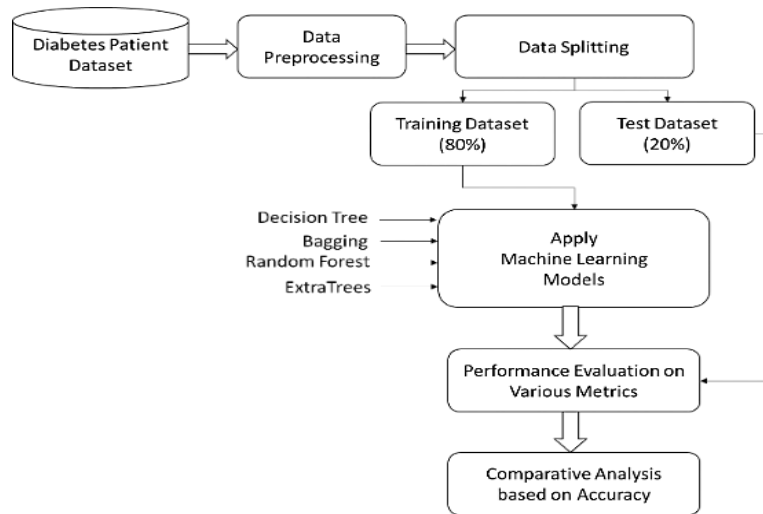
Figure 1. The proposed model

3.2 Data Preprocessing

Preprocessing was done to analyze the features in the dataset and to make the classification more efficient. Although there are no null values in the dataset, there are categorical values. The categorical values were converted to numerical values. There are 38.46% (1) and 61.54% negative (0) classes in the dataset. The scatter plots of each feature over the classes are given in Figure 2.

These scatter plots represent the distribution of diabetes disease according to the parameters. The data in the dataset according to the parameters were visualized with these plots. When the dataset examined, it is seen that there is an unbalanced distribution problem. Due to the unbalanced distribution problem in the dataset, The SMOTE approach was used. The SMOTE method is regarded as the most popular and frequently the most effective sampling technique [23]. Numerous imbalanced dataset issues have been addressed using the technique created in 2002. This technique differs from other approaches in that it creates artificial instances based on the k nearest neighbors of the instances under examination, as opposed to replicating the minority class data.

Table 3. Feature Details

| Features Name	Features Type	Data Type	Possible Value
Age	Predictive	Integer	16-90
Sex	Predictive	Object	Male, Female
Polyuria	Predictive	Object	Yes, No
Sudden Weight Loss	Predictive	Object	Yes, No
Weakness	Predictive	Object	Yes, No
Polyphagia	Predictive	Object	Yes, No
Genital Thrush	Predictive	Object	Yes, No
Visual Blurring	Predictive	Object	Yes, No
Itching	Predictive	Object	Yes, No
Irritability	Predictive	Object	Yes, No
Delayed Healing	Predictive	Object	Yes, No
Partial Paresis	Predictive	Object	Yes, No
Muscle Stiffness	Predictive	Object	Yes, No
Alopecia	Predictive	Object	Yes, No
Obesity	Predictive	Object	Yes, No
Class	Responsive	Object	Positive, Negative
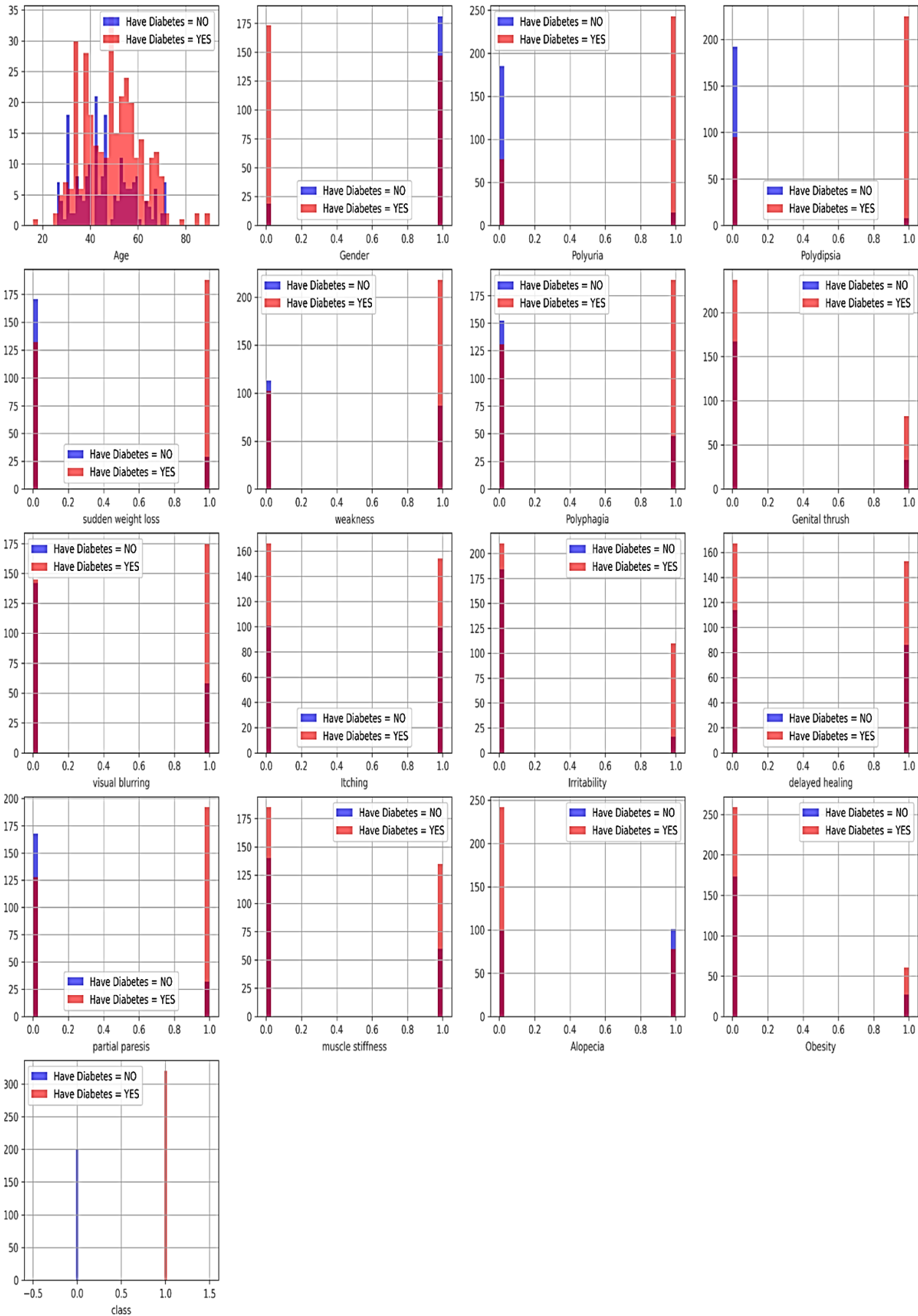
Figure 2. The scatter plots of each feature

Following is a brief summary of how the algorithm operates:

1. The k-closest neighbors of each observation pertaining to the minority class are searched,
2. The difference between the observation of the minority class and the observation with the k nearest neighbors (K-Nearest Neighbors) is taken,
3. The difference determined in Step 2 is multiplied by a random integer (α) is selected at random from (0,1),
4. Using the Equation (1), a new synthetic observation is produced:

$$x_{yeni} = xi + (xj - xi) * \alpha \qquad (1)$$

5. Repeat steps 1-4 to obtain the desired number of synthetic observations.

3.3 Machine Learning Algorithms

3.3.1 Decision Tree

The first algorithm used in prediction of the diabetes mellitus is the decision tree algorithm [24]. The basic idea in the decision tree algorithm, which is a powerful classification algorithm among machine learning algorithms, is based on repeatedly dividing the input data into groups with the help of a classification algorithm. As a result of this division, nodes are formed and these nodes are labeled. The division continues in depth until all nodes of the group have the same class label. The advantage of this algorithm is that it is used very frequently and it is an algorithm that can be easily interpreted and created easily. Decision trees, which are one of the supervised learning methods, consist of roots, nodes, branches and leaves like a tree. There are some criteria used in feature selection, that is, in determining which node will be selected. These criteria are; information gain, gain ratio and gini index.

3.3.2 Bagging with Decision Tree

The bagging method is one of the ensemble learning methods derived by the award-winning statistician Breiman in 1996. In bagging, the dataset is distributed across several bootstrap copies. Each replica is plotted with replacement, regardless of the original dataset; on average, each copy contains 63.2% of the original data. The process is accomplished by repeatedly running the weak learner on various bootstraps. At each iteration, the classifier learned from the weak learner is combined into the strong composite classifier to achieve higher accuracy than any single

Real Class Label	Predicted Class Label	
	TP	TN
	FP	FN

component classifier can do alone [25]. In this study, a

bagging algorithm is utilized to transform weak learners into strong learners.

3.3.3 Random Forest

Random Forest, another most commonly used machine learning technique, is a combination of the Bagging method developed by Breiman in 1996 and the Random Subspace method developed by Kim Ho [26]. This technique combines multiple classifiers to improve performance. In different subsets of the given dataset, the Random Forest classifier consists of decision trees. Each decision tree output is averaged to improve the prediction accuracy in the given dataset. Random Forest takes predictions from multiple trees, calculates the maximum number of predictions, and predicts the final output. In the Random Forest algorithm, random data points are first selected from the training data set. A subset of the decision tree associated with this selected point is developed. The first two steps are applied again by determining the number of the decision tree to be created. Finally, at the given data points, each decision tree is estimated and new data points are assigned to the category that wins the majority vote.

3.3.4 Extra Trees

The Extra Tree algorithm, which consists of a collection of decision trees, is referred to collections of other decision tree algorithm collections as bootstrapping (bagging) and random forest [27]. The training dataset is used to create a large number of unpruned decision trees as part of the Extra Trees technique. When utilizing regression or classification, estimates are performed by averaging the decision tree estimation or by employing majority vote. The Extra Trees approach fits each decision tree on the whole training dataset, in contrast to bagging and random forest, which only use a bootstrap sample of the training dataset to construct each decision tree. With regard to calculation time, the Extra Trees approach is faster.

3.4 Performance Evaluation

In machine learning, the confusion matrix is used to show the relationship between real class labels and predicted class labels. It is a visualization tool used to show the accuracy values obtained as a result of the classification process. It is used to represent true positive (TP), correct negative (TN), false positive (FP), false negative (FN).
• True Positive (TP): It indicates that the patient has diabetes.
• True Negative (TN): It indicates that the patient does not have diabetes.
• False Positive (FP): It indicates that a person who does not have diabetes has been misdiagnosed with diabetes.
• False Negative (FN): It indicates that a person with diabetes is misdiagnosed as not having diabetes.

Table 4. **C**omparison of algorithms using 10-CV

	ACC	PREC	RC	FS
DT	%97.35	%97.79	%96.87	%97.33
Bagging with Decision Tree	%97.50	%98.41	%96.56	%97.48
RF	%98.59	%98.75	%98.44	%98.59
Extra Trees	**%98.91**	**%98.75**	**%99.06**	**%98.91**

* ACC: Accuracy, PREC: Precision, RC: Recall, FS: F1-Score

Table 5. Confusion matrix results of classification algorithms

DT

Real-Class Label		Predicted Class Label	
		0	**1**
	0	61	1
	1	1	65

Bagging with Decision Tree

Real-Class bel		Predicted Class Label	
		0	**1**
	0	61	1
	1	2	64

RF

Real-Class abel		Predicted Class Label	
		0	**1**
	0	62	0
	1	2	64

Extra Trees

Real-Class Label		Predicted Class Label	
		0	**1**
	0	62	0
	1	1	65

Table 6. Overall performance comparison of algorithms

	ACC (Training)	ACC (Test)	PREC (Test)	RC (Test)	FS (Test)
DT	%100.00	%98.44	%98.00	%98.00	%98.00
Bagging with Decision Tree	%99.61	%97.66	%97.00	%98.00	%98.00
RF	%100.00	%98.44	%97.00	%100.00	%98.00
Extra Trees	**%100.00**	**%99.22**	**%98.00**	**%100.00**	**%99.00**

* ACC: Accuracy, PREC: Precision, RC: Recall, FS: F1-Score

Table 7. Evaluation of related studies

References	The Best Algorithm	The Best Result	The Difference with Our Work
Zou et. al., 2018	Random Forest	%80.84	+18.36%
Nai-arun et. al.,2014	Bagging and base classifier DT	%95.31	+3.89%
Hegde et. al., 2019	Random Forest	%94.14	+5.06%
Başer et.al, 2021[28]	Random Forest	%84,78	+14.42%

Using these values in the confusion matrix given in the table, the following metrics used to determine the performance of the classification algorithm are calculated.

Measures	Definitions	Formula
Accuracy	Refers to the ratio of the number of correctly classified samples to the total number of samples	$\dfrac{TP + TN}{\text{Total no of samples}}$
Precision (P)	Classifiers correctness/accuracy is measured by Precision	$\dfrac{TP}{TP + FP}$
Recall (R)	Refers to the power of the classification algorithm to correctly predict positive samples.	$\dfrac{TP}{TP + FN}$

F1-Score	It is the geometric mean of the sensitivity and recall criteria and allows the values of both criteria to be considered together.	$\dfrac{2 * (P * R)}{P + R}$

4. Test Results

In this section, we discuss the experimental test and evaluate the machine learning algorithms to predict diabetes mellitus. These tests aim to estimate whether the patient has diabetes mellitus or not. In addition, the sckit-learn library, which is a popular library containing functions of algorithms developed in the field of machine learning and data mining developed with Python programming language, has been utilized. The tests were performed on Windows 10 operating system, using Python version 3.8.10. All tests experiments

were performed on a computer with 12GB of RAM (Intel ® Core™ i7-4700HQ CPU @ 2.40Ghz 2.40GHz).

The problem in this study was considered as a classification problem and Decision Tree (DT), Bagging with DT, Random Forest (RF), and Extra Trees algorithms were used in the classification stage. Firstly, 10-CV was utilized in order to demonstrate the performance of the algorithms. The results of 10-CV are given in Table 4.

According to the proposed system, the dataset was split into 80% train and 20% test as given in Figure 1. Then, the confusion matrix obtained as a result of the tests performed with machine learning algorithms is shown in Table 5. In confusion matrices given Table 5, 0 represents cases without diabetes mellitus and 1 represents cases with diabetes mellitus. It is seen that the Extra Trees algorithm is more successful than other algorithms that predict diabetes mellitus when Table 5 is examined. The performance measures calculated using the confusion matrix are given in Table 6.

When the results given in Table 6 are examined, it is seen that the Extra Trees algorithm performs the best prediction with an accuracy of 99.22%. The DF algorithm has an accuracy of 98.44%, the Bagging algorithm has an accuracy of 97.66% and the RF algorithm has an accuracy of %98.44. We observed that decision tree-based classifiers give good results for this dataset. Because the features in the dataset are in the logic of a decision mechanism.

For data with unbalanced class distribution, it would be more accurate to use the f1-score performance metric, where precision and recall metrics are considered together, instead of accuracy. Accordingly, considering the values in Table 5, it is seen that better f1-score values are obtained by applying the Extra Trees algorithm. When the algorithm is examined in terms of processing times, it is seen that there is not much difference between them. In Table 7, we compare our work with the literature in order to demonstrate the efficiency of the proposed approach.

5. Conclusions

Diabetes is one of the diseases that can have undesirable effects on various organs and last throughout life. Diabetes, which is a disease that should be treated under the supervision of a doctor, can lead to serious complications in the body if not treated. In addition to the medical methods used in the diagnosis of diabetes, this disease can be detected by artificial intelligence approached. With these approaches, experts are assisted in the diagnosis of the disease. This paper aims to predict the diabetes. First of all, a data preprocessing was done on the dataset obtained from UCI. SMOTE algorithm was used during this preprocessing. Then, different machine learning algorithms were used to predict diabetes. In this paper, using Decision Tree, Bagging and Decision Tree, Random Forest and Extra Trees algorithms, the most

successful accuracy rate was obtained from the Extra Trees algorithm with 99.22%. In future studies, it is aimed to detect diabetes by using deep learning on the dataset and machine learning methods not used in this study. In future studies, it is aimed to realize an artificial intelligence-based decision support system that will significantly help experts with big data technologies, deep learning and transfer learning approaches in the diagnosis of diabetes.

Declaration

The author(s) declared no potential conflicts of interest with respect to the research, authorship, and/or publication of this article. The author(s) also declared that this article is original, was prepared in accordance with international publication and research ethics, and ethical committee permission or any special permission is not required.

Author Contributions

O. Sen Kaya performed the literature research, analysis of the methodology, preparation of algorithm figures, examination of the test results, writing the article. S. Bozkurt Keser performed the literature research, design and implementation of the research, analysis of the results, organizing and writing the article. K. Keskin contributed to organizing, writing, and proofreading the article.

References

1. Kavakiotis, I., Tsave, O., Salifoglou, A., Maglaveras, N., Vlahavas, I., and Chouvarda, I., Machine learning, and data mining methods in diabetes research. Computational and structural biotechnology journal, 2017. **15**: p. 104-116.
2. Choubey, D.K., Paul, S., and Bhattacharjee, J., Soft computing approaches for diabetes disease diagnosis: a survey. International Journal of Applied Engineering Research, 2014. **9**(21): p. 11715-11726.
3. Ganji, M.F. and Abadeh, M.S., A fuzzy classification system based on Ant Colony Optimization for diabetes disease diagnosis. Expert Systems with Applications, 2011. **38**(12): p. 14650-14659.
4. Karegowda, A.G., Manjunath, A., and Jayaram, M., Application of genetic algorithm optimized neural network connection weights for medical diagnosis of Pima Indians diabetes. International Journal on Soft Computing, 2011. **2**(2): p. 15-23.
5. Maniruzzaman, M., Kumar, N., Abedin, M. M., Islam, M. S., Suri, H. S., El-Baz, A. S., and Suri, J. S., Comparative approaches for classification of diabetes mellitus data: Machine learning paradigm. Computer methods and programs in biomedicine, 2017. **152**: p. 23-34.
6. Mir, A. and Dhage, S.N., Diabetes disease prediction using machine learning on big data of healthcare. in 2018 fourth international conference on computing communication control and automation (ICCUBEA). 2018. IEEE.
7. Sisodia, D. and Sisodia, D. S., Prediction of diabetes using classification algorithms. Procedia computer science, 2018. **132**: p. 1578-1585.

8. Wu, H., Yang, S., Huang, Z., He, J., and Wang, X., Type 2 diabetes mellitus prediction model based on data mining. Informatics in Medicine Unlocked, 2018. **10**: p. 100-107.

9. Zou, Q., Qu, K., Luo, Y., Yin, D., Ju, Y., and Tang, H., Predicting diabetes mellitus with machine learning techniques. Frontiers in genetics, 2018. **9**: p. 515.

10. Alam, T. M., Iqbal, M. A., Ali, Y., Wahab, A., Ijaz, S., Baig, T. I., and Abbas, Z., A model for early prediction of diabetes. Informatics in Medicine Unlocked, 2019. **16**: p. 100204.

11. Hegde, H., Shimpi, N., Panny, A., Glurich, I., Christie, P., and Acharya, A., Development of non-invasive diabetes risk prediction models as decision support tools designed for application in the dental clinical environment. Informatics in medicine unlocked, 2019. **17**: p. 100254.

12. Lukmanto, R. B., Nugroho, A., and Akbar, H., Early detection of diabetes mellitus using feature selection and fuzzy support vector machine. Procedia Computer Science, 2019. **157**: p. 46-54.

13. Juliet, M.P.L. and T. Bhavadharani, An improved prediction model for type 2 diabetes mellitus disease using clustering and classification algorithms. International Research Journal of Engineering and Technology (IRJET), **6**(2): p. 1179-1186.

14. Wang, Q., Cao, W., Guo, J., Ren, J., Cheng, Y., and Davis, D. N., DMP_MI: An effective diabetes mellitus classification algorithm on imbalanced data With missing values. IEEE Access, 2019. **7**: p. 102232-102238.

15. Khairunnisa, S., Suyanto, S., and Yunanto, P. E. Removing Noise, Reducing dimension, and Weighting Distance to Enhance k-Nearest Neighbors for Diabetes Classification. in 2020 3rd International Seminar on Research of Information Technology and Intelligent Systems (ISRITI). 2020. IEEE.

16. Tarokh, M.J., Type 2 Diabetes Prediction Using Machine Learning Algorithms. Jorjani Biomedicine Journal, 2020. **8**(3): p. 4-18.

17. Gupta, D., Choudhury, A., Gupta, U., Singh, P., and Prasad, M., Computational approach to clinical diagnosis of diabetes disease: a comparative study. Multimedia Tools and Applications, 2021: p. 1-26.

18. Nai-Arun, N., and Sittidech, P., Ensemble learning model for diabetes classification. in Advanced Materials Research. 2014. Trans Tech Publ.

19. Patil, M. K., Sawarkar, S. D., and Narwane, M. S. Narwane, Designing a Model to Detect Diabetes using Machine Learning. Int. J. Eng. Res. Technol, **8**(11), p: 333-340

20. Hasan, M. K., Alam, M. A., Das, D., Hossain, E., and Hasan, M., Diabetes prediction using ensembling of different machine learning classifiers. IEEE Access, 2020. **8**: p. 76516-76531.

21. Kopitar, L., Kocbek, P., Cilar, L., Sheikh, A., and Stiglic, G., Early detection of type 2 diabetes mellitus using machine learning-based prediction models. Scientific reports, 2020. **10**(1): p. 1-12.

22. Gamara, R. P. C., Bandala, A. A., Loresco, P. J. M., and Vicerra, R. R. P., Early stage diabetes likelihood prediction using artificial neural networks. in 2020 IEEE 12th International Conference on Humanoid, Nanotechnology, Information Technology, Communication and Control, Environment, and Management (HNICEM). 2020, IEEE.

23. Hu, F., Li, H., A novel boundary oversampling algorithm based on neighborhood rough set model: NRSBoundary-SMOTE. Mathematical Problems in Engineering, 2013.

24. Quinlan, J. R., Induction of decision trees, Machine Learning, **1**, p: 81-106, 1986.

25. Perveen, S., Shahbaz, M., Guergachi, A., and Keshavjee, K., Performance analysis of data mining classification techniques to predict diabetes. ScienceDirect, 2016. **82**: 115-121.

26. Breiman, L., 2001. Random forests. Machine Learning, **45**(1): p. 5-32, 2001.

27. Geurts, P., Ernst, D., and Wehenkel, L., Extremely Randomized Trees, Machine Learning, **63**(1), p. 3-42, 2006.

28. Başer, B. Ö., Yangın, M., and Sarıdaş, E. S., Makine öğrenmesi teknikleriyle diyabet hastalığının sınıflandırılması. Journal of Natural & Applied Sciences, **25**(1), 2021.